X-ray emission from faint galaxies and quasars

Almaini, Omar

X-ray Emission from Faint Galaxies and Quasars

by

Omar Almaini

Department Of Physics,

University of Durham .

Submitted for the degree of

Doctor of Philosophy

March 1996

X-ray Emission from Faint Galaxies and Quasars

Omar Almaini

Abstract

In this thesis a study of faint X-ray sources is undertaken to understand the nature and origin of the Cosmic X-ray Background (XRB). A study of the X-ray variability characteristics of the QSO population is also presented.

The optical identification of faint *ROSAT* sources is described. A large fraction of these sources are identified as QSOs. A number of the remaining sources appear to be associated with faint galaxies with a range of morphological types. The discovery of a rare, high redshift obscured QSO is also described and discussed.

A method is developed to study the X-ray variability of faint QSOs. Low amplitude variability ($\sim 25\% \, rms$) on timescales of hours to days appears to be characteristic. Contrary to the trends apparent in local AGN, the QSO population show no evidence for a decrease in variability amplitude with luminosity. There is also no trend in variability with redshift, which may favour a short lived model for QSO evolution. A bright, highly variable Seyfert galaxy is analysed in detail.

To constrain the galaxy contribution to the XRB a cross-correlation analysis is presented. Cross-correlating faint galaxy catalogues with unidentified X-ray sources suggests that faint $b_j < 23$ galaxies account for $\sim 21 \pm 6\%$ of all X-ray sources to a flux limit $S(0.5-2.0\,\mathrm{keV}) \sim 4 \times 10^{-15} \mathrm{erg\,s^{-1}cm^{-2}}$. Galaxies are then cross-correlated with the remaining *unresolved* XRB. A highly significant signal is obtained on 3 deep *ROSAT* fields. Using a formalism to model the galaxy population and its clustering, an estimate of the local X-ray volume emissivity is obtained. The results suggest that $b_j < 23$ galaxies contribute $\sim 20\%$ of the unresolved XRB. Comparing the cross-correlation of faint and bright galaxies with theoretical models reveals strong evolution in the X-ray luminosity of galaxies with the form $L_x \propto (1+z)^{3\pm1}$. Extrapolation to high redshift suggests that faint galaxies contribute $50-100\%$ of the unresolved XRB.

Finally, a study of the X-ray spectra of faint *ROSAT* sources is presented. The mean source spectra harden significantly at lower flux. Separating the QSOs from the unidentified sources and galaxies, we find no trend in the $0.5-2\,\mathrm{keV}$ spectra of QSOs. The remaining population produces the spectral hardening. Taking a subset of the most probable X-ray luminous galaxies, these show significantly harder spectra than QSOs with a mean photon index of $\Gamma \sim 1.5 \pm 0.1$. X-ray luminous galaxies could therefore account for the missing component of the XRB.

Declaration

The work described in this thesis was undertaken by the author as a PPARC research student at the University of Durham under the supervision of Dr. T.Shanks. No part of this thesis has been submitted for a degree at the University of Durham or at any other University.

All of the work described in this thesis was carried out solely by the author with the exception of Chapter 2 which was carried out in collaboration with Dr. Gordon Stewart and Dr. Brian Boyle as explicitly described in the text. The X-ray source catalogue on which much of this thesis is based was obtained as part of the Deep *ROSAT* Survey collaboration with Dr. Tom Shanks, Dr. Brian Boyle, Dr. Gordon Stewart, Dr. Richard Griffiths, Dr. Ioannis Georgantopoulos and Dr. Nathan Roche.

Some of the results presented here have been published elsewhere as follows:

Almaini,O., Boyle,B.J., Georgantopoulos,I., Griffiths,R.E., Shanks,T., and Stewart,G.C., 1995, MNRAS , 277, L31,
A deep ROSAT survey IX: Discovery of a High Redshift Type 2 QSO

Almaini,O., Shanks,T., Boyle,B.J., Griffiths,R.E., Roche,N., Stewart,G.C. and Georgantopoulos,I. 1996, MNRAS Accepted,
A Deep ROSAT survey XII - The X-ray spectra of faint ROSAT Sources

Almaini, O., Shanks, T., Boyle, B.J., Stewart, G.C. and Griffiths, R.E., (1995). Posters from the 17th Texas Symposium on Relativistic Astrophysics, MPE special report.
ROSAT X-ray Variability in a Complete Flux-Limited Sample of QSOs

Shanks, T., Almaini, O., Boyle, B.J., Della-Ceca, R., Done, C., Georgantopoulos, I., Griffiths, R.E., Rawlings, S.J., Roche, N., & Stewart, G.C., (1996). In Rontgensstrahlung from the Universe, in press.
The Faint Galaxy Contribution to the X-ray Background

Roche,N., Shanks,T., Almaini,O., Boyle,B.J., Georgantopoulos,I., Stewart,G.C. and Griffiths,R.E., 1995, Mon. Not. R. astr. Soc., 276, 706,
A deep ROSAT survey VIII: X-ray detection of the evolved galaxy cluster 0055-279

ACKNOWLEDGEMENTS

I thank the Department of Physics at the University of Durham for the provision of facilities that allowed this research to take place and acknowledge the receipt of a PPARC research studentship. I also thank the Institute of Astronomy in Cambridge for kindly providing the facilities I needed to finish my research and write this thesis.

It is a pleasure to thank the friendly, approachable members of the astronomy group in Durham for creating an atmosphere so conducive to front line research. I am indebted to Tom Shanks for his patient, conscientious supervision. His enthusiasm and genuine fascination with the universe is infectious. I must also thank the other members of the Deep *ROSAT* Survey collaboration, namely Brian Boyle, Gordon Stewart, Richard Griffiths, Ioannis Georgantopoulos and Nathan Roche. It was a privilege work with such fine astronomers. A big thank you to Lilian Graham who read every word of this dissertation. Her suggestions improved the text enormously. I am also indebted to Chris Done for her help and enthusiasm. Meeting Chris, with her vast knowledge of X-ray astronomy, made me realise how much I had still to learn. I am also grateful to Andy Fabian, Chris Reynolds and Neil Brandt for useful discussions and their sound advice. On the computing front, warm thanks to Alan Lotts and Peter Draper for keeping the computing system alive against all odds. Douglas Burke and Andrew Ratcliffe deserve OBE's for putting up with my endless stream of computing problems and even patiently debugging my Fortran programs. I must also thank George Hau for those cool Perl scripts.

I am enormously grateful to the members of Durham University Archery Club, especially Mark Deakin, Mark Preston and Martin Bradley. We made a great team. A special thank you to Mike Carr at the Maiden Castle Sports Centre for allowing me to train at all ungodly hours.

Warm thanks to Douglas Burke, Roger Haynes, Scott Croom, Claire Halliday, Jane Chapman, Luis Teodoro, James Steel, Glenn Baggley, Paul Young, Gillian Wilson, Nuanwan Sanguansak, Raphael Guzman, Steve Zepf and others too numerous to mention who have tolerated my childishness for so long. In particular, I cannot thank Andrew Ratcliffe enough for the help and friendship he has shown over the years, especially for standing by me through the rough times. Thanks also to Adrian Askew, Robert Wright, Ioannis Pachos and Fotini Vassiliou for dragging me away from work, buying me drinks and keeping me sane. A special mention for Haley and 'the boys' - they know who they are. I am grateful to my new office mates, George Hau, Zdenka Kunkic, Julian Elliot, Girish Beeharry, Tiziana Di Matteo, Gordon Ogilvie plus all my new friends at the IoA for putting up with me in recent months.

I owe so much to my family for their love and encouragement over the years. I would never have come this far without their rock solid support and for this I consider myself a very lucky person. Thank you Mum, Dad, Khalid, Nadia for always being there.

Finally, I thank Lilian for her love and everything else..

Omar Almaini

March 28th 1996

Contents

Chapter 1

Introduction

In this chapter our current understanding of the X-ray background (XRB) is reviewed. Quasars are known to contribute a significant fraction of this radiation but cannot explain the whole X-ray sky, suggesting the need for a new energetic source population. Unusually X-ray luminous galaxies may provide a solution, although the nature of the X-ray emitting mechanism is unclear. Finally, the X-ray variability characteristics of active galactic nuclei (AGN) are described and discussed.

1.1 The X-ray background

1.1.1 Discovery

In June 1962 a rocket was launched to study X-rays reflected from the moon. No such reflection was seen, but the first non-solar X-ray source was discovered in the constellation Scorpius. This cosmic source (SCO X-1) was at first viewed with some disbelief. Assuming that the X-rays were emitted by a faint star within the X-ray error box would imply an X-ray luminosity a billion times higher than the sun. As more X-ray sources were detected it soon became clear that such energetic phenomena did indeed exist. With the launch of successive generations of instruments culminating in dedicated X-ray satellites it has emerged that most of these galactic X-ray sources are binary star systems in which material accretes onto a highly collapsed compact object (eg. neutron star or black hole). As we will discuss, a much larger fraction of the X-ray sources have an extragalactic origin.

The second important finding of this first rocket flight was the discovery that the sky is bathed in a uniform, seemingly diffuse glow of X-rays which became known as the X-ray background (XRB) (Giacconi et el 1962). The uniformity of this background radiation immediately suggested that a large fraction was extragalactic in origin. However, despite over 30 years of study, the origin and nature of this radiation remains a major unsolved problem. With the advent of sensitive imaging satellites such as *Einstein* and *ROSAT* most of the XRB can be now be resolved into discrete sources (at least at low energies) but no one class of source can explain more than 50% of the total flux. We will now summarise the basic properties of the XRB and discuss the various possibilities for its origin.

1.1.2 The spectrum of the XRB

As an operational definition, we will define the XRB over the range of energies from 0.1 keV (120Å) to 100keV.

Below 0.5 keV the XRB is dominated by galactic emission. At these energies the interstellar medium absorbs a significant fraction of any extragalactic contribution. The emission we do see is mostly from a local hot bubble of gas with a temperature of $\sim 10^6$ K. Using the Large Magellanic Cloud to shadow the extragalactic component, McCammon & Sanders (1990) suggest an upper limit of $\sim$ 10% on the extragalactic contribution at 0.25 keV.

The *HEAO − 1A2* experiment permitted the most accurate measurement of the XRB spectrum from 3 − 45 keV. In this band the spectrum is a remarkably good fit to a thermal Bremsstrahlung model with a temperature of $\sim$ 40 keV (Marshall et al 1983). Since most of the energy density of the XRB is concentrated in this band, this led many researchers to consider thermal models to explain the XRB (see section 1.1.3), invoking a hot intergalactic gas to simultaneously explain the isotropy. Over the 3 - 10keV band, where the most sensitive imaging satellites have concentrated, the XRB is equally well fit by a power law model with photon index of $\Gamma = 1.4$ (equivalent to an energy index of $\alpha = 0.4$). Recent results of the *ASCA* satellite has shown that this spectral index extends down to 1keV. These results are of particular importance in restricting the contribution from QSOs (see section 1.1.4).

At the highest energies, above 60keV, the spectrum falls off rapidly. This sharp drop has been used to infer a cut-off in the spectrum of AGN (or any significant contributor to the XRB) in order to prevent an overproduction in the Gamma-ray background above a few MeV (Schwartz & Tucker 1988).

1.1.3 A diffuse thermal origin?

Above $\sim$ 0.5 keV the XRB is dominated by extragalactic X-ray sources. The first such indication came from the observed uniformity of the X-ray sky, now known to be isotropic to within a few percent on large scales (Warwick et al 1989). Further evidence was provided with the discovery of a dipole anisotropy coinciding with the motion of our galaxy through the microwave background frame, the so called Compton-Getting effect (Shafer 1983, Shafer & Fabian 1983).

The diffuse, smooth appearance of the XRB led to suggestions that it may be caused by thermal emission from a hot, intergalactic medium (Hoyle 1963). Although this would seem a very natural explanation, given the almost perfect thermal Bremsstrahlung shape of the spectrum, a diffuse origin for the XRB can now be ruled out by two independent arguments. The development of higher resolution X-ray satellites has shown that a considerable fraction of the soft XRB (below 3 keV) can be resolved into individual sources. Most of these were identified as AGN with fairly steep X-ray spectra, typically with photon power law indices of $\Gamma \simeq 2$. Subtracting these sources from the total XRB leaves a residual spectrum which cannot be thermal in origin. Thus the near perfect thermal Bremsstrahlung shape of the XRB would seem no more than a cosmic red herring. A significant contribution from a hot intergalactic medium can also be ruled using the smoothness of the microwave background spectrum, as observed by the *COBE* satellite. Microwave background photons would inverse Compton scatter in the hot plasma and produce a distortion in the observed microwave spectrum (Wright 1979). The near perfect black body spectrum observed by *COBE* can therefore place an upper limit of $\sim$ 3% on any XRB contribution from intergalactic hot gas (Mather 1990).

1.1.4 The contribution from QSOs

The most significant progress has been made in the soft X-ray band below 3keV since the launch of high resolution imaging satellites such as *Einstein* and, more recently, with *ROSAT*.

The discovery of many AGN by the *Einstein* satellite (Giacconi et al 1979) initially suggested that they could explain the whole XRB at 2keV (Marshall et al 1983, Zamorani et al 1981). Although the flux from these QSOs could only directly account for $\sim$ 20% of the total background, by using the optical to X-ray luminosity ratios the optical QSO luminosity function was scaled to estimate the X-ray luminosity function . Extrapolation to high redshift implied that QSOs could produce the entire XRB. We now know that this result was an overestimate by at least a factor of two, caused by limited knowledge of the form and evolution of the optical luminosity function. Nevertheless,

QSOs became established as the best candidates to explain the XRB.

The launch of the *ROSAT* satellite has allowed us to detect X-ray sources at least an order of magnitude fainter than before. Using the deepest *ROSAT* exposures (Hasinger et al 1993) up to 70% of the $0.5 - 2\,\mathrm{keV}$ XRB can now been resolved into discrete sources with a density of $\sim 400\ \mathrm{deg}^{-2}$. Using optical multifibre spectroscopy Shanks et al (1991) attempted to identify the optical counterparts to many such sources. Since QSOs were considered very likely X-ray emitters, these fields were centred on the ultra-violet excess (UVX) QSO fields of Boyle et al (1990). This enabled many QSO to be immediately identified with X-ray sources. Further spectroscopic observations revealed that QSOs account for over 50% of the resolved X-ray sources and directly account for $\sim 30\%$ of the XRB at 1keV. A further four fields were obtained, allowing 128 QSOs to be identified in total. For the first time this allowed an accurate determination of the QSO X-ray luminosity function and its evolution (Boyle et al 1993, 1994). Extrapolating this relationship to faint fluxes and high redshifts suggested a contribution of $\sim 35 - 50\%$ of the XRB at 1keV. Accounting for the whole XRB with QSOs can only be achieved with a significant steepening of the faint end of the luminosity function, suggesting either that a new class of X-ray source is required or the existence of a large population of previously unidentified, low luminosity AGN.

Studies of the source number count distribution provide further evidence for the emergence of a new population. Measuring the integral number count as a function of flux, we expect a power law slope of $\gamma = 2.5$ in a Euclidean universe. Using the deepest *ROSAT* exposures, and thus the faintest X-ray sources yet detected, Hasinger et al (1993) found that the number count distribution flattens from a Euclidean relationship below a flux of $S = 10^{-14}\mathrm{erg\ s^{-1}cm^{-2}}$ to a slope of $\Gamma = 1.9$. Georgantopoulos et al (1996) have confirmed this result on five shallower *ROSAT* fields. Though not as deep as the Hasinger survey, these have the advantage of optical identification. In particular, the behaviour of the AGN population could be assessed separately from the remaining sources. They found that the number count relationship for AGN undergoes an abrupt break below $\sim 10^{-14}\mathrm{erg\ s^{-1}cm^{-2}}$, turning over to a slope of $\gamma = 1.1 \pm 0.5$, flatter than the distribution as a whole. Thus the AGN contribution appears to drop at the faintest limits. Extrapolating this behaviour suggests that AGN contribute no more than $\sim 50\%$ of the total XRB. The emergence of a new X-ray source population is a likely explanation.

There is also some evidence that QSOs may cluster too strongly to account for more that $\sim 50\%$ of the XRB at 1keV (Georgantopoulos et al 1996). The upper limits on the anisotropy suggest that QSOs would produce more 'clumpiness' on small scales and thus overestimate the angular auto-correlation function.

1.1.5 The spectral paradox of the XRB

There has always been a serious problem in explaining the entire XRB with QSOs. While the X-ray spectrum of the XRB is a good fit to a power law slope of $\Gamma = 1.4$ in the $0.1 - 10$ keV band (Gendreau et al 1995) the spectra of QSOs show much steeper spectra with $\Gamma \simeq 2$ (Turner & Pounds 1989). This gave rise to the 'Spectral Paradox', namely that as more sources were resolved and identified with steep spectrum AGN, the more difficult it became to explain the XRB with such sources. Two basic mechanisms have been invoked to overcome this problem and thus explain the entire XRB with ordinary QSOs:

(i) The discovery of a hump in the X-ray spectra of *Ginga* AGN (Pounds et al 1990) was interpreted as reprocessed X-ray emission reflected from a 'cold' slab of material (eg. the accretion disk). This feature hardens the X-ray spectra of AGN in the $10 - 20$ keV band. Furthermore, GRANAT and OSSE observations of a sample of Seyfert 1 galaxies revealed a sharp steepening in their spectra near ~ 100 keV, as required for any candidate to explain the X-ray background (Schwartz & Tucker 1988). These observations prompted various models which attempted to explain the XRB using a superposition of AGN spectra over a wide range of redshifts (eg. Zdziarski et al 1993). In principle such models could explain the entire XRB with AGN. However, as noted by Vikhlinin et al (1995), these models neglect the contribution of steep spectrum sources already resolved by *ROSAT* and *Einstein* and as such do not give an acceptable fit to the residual background radiation. It also emerged that this model overpredicts the X-ray source number counts at soft X-ray energies (Setti 1992, Comastri 1992).

(ii) There have been suggestions that the intrinsic spectra of AGN may harden at high redshift due either to an intrinsic change in their properties (Morisawa & Takahara 1990) or intervening absorption from damped Lyman alpha systems (Vikhlinin et al 1995). These are testable hypotheses. Although the X-ray spectra of distant QSOs are not well studied, preliminary indications from X-ray surveys reveal no trend in the mean spectra of QSOs as a function of redshift (Stewart et al 1994, Almaini et al 1995).

Thus, on the grounds of their X-ray spectra, number count distribution, luminosity function and clustering properties it would appear that ordinary QSOs do not comprise the entire XRB. A different form of AGN may provide a solution however, as we will shortly discuss.

1.1.6 X-ray luminous galaxies

Normal galaxies of all types are known to be significant sources of X-ray emission. *Einstein* observations revealed that most spiral galaxies show an X-ray luminosity linearly related to their blue band luminosity. A bright galaxy of absolute magnitude $M_B = -21$ has a typical X-ray luminosity of $L_X(0.5 - 3\,\mathrm{keV}) \sim 10^{40}\mathrm{ergs}^{-1}$ (Fabbiano, Kim & Trinchieri 1992). The relatively high X-ray temperatures ($kT \sim 3 - 6\,\mathrm{keV}$) are consistent with low-mass X-ray binaries as the main source of X-ray flux (Kim, Fabbiano & Trinchieri 1992). These binaries appear to form a constant fraction of the stellar mass, thus explaining the linear optical to X-ray luminosity relation. However, scaling this ratio by the optical volume emissivity of all galaxies can produce only $\sim 3\%$ of the total XRB.

The X-ray luminosity of elliptical galaxies is generally higher than expected from the linear relation applicable to spirals (Fabbiano 1989). This is caused by additional X-ray emission from diffuse hot gas. The temperature of this gas is generally fairly low ($\sim 1\,\mathrm{keV}$), which produces a very soft X-ray spectrum (Awaki et al 1994). This soft spectrum, coupled with the low space density of elliptical galaxies, can also rule them out as significant contributors to the XRB.

Thus ordinary galaxies do not seem likely candidates to explain the missing X-ray source population. However, at the high luminosity end of the 'normal' galaxy distribution there is a class of unusually X-ray luminous galaxies. In particular, a number of X-ray bright starburst galaxies (eg. M82) have been known for many years (Watson, Stanger & Griffiths 1982). The potential contribution of 'narrow emission line' galaxies to the XRB was eventually quantified after many were observed with both the *Einstein* and IRAS satellites (Griffiths & Padovani 1990; Green, Anderson & Ward 1992). By relating the X-ray and far infra-red luminosities an estimate of the X-ray luminosity function was obtained. Extrapolation to high redshift suggested that IRAS galaxies could in principle contribute $10 - 30\%$ of the XRB, depending on their evolution with redshift. Boller et al (1992) correlated the *ROSAT* all-sky survey with objects identified in the IRAS database and suggested the existence of a number of apparently normal spirals with exceptionally high X-ray luminosities ($\sim 10^{43}\mathrm{erg\ s}^{-1}$). Moran, Halpern and Helfand (1994) have since discovered that many of these were in misclassified Seyfert galaxies. However, as pointed out by Ward et al (1993), a number of galaxies remain with optical spectra that cannot be classified as AGN but which are nevertheless $10-100$ times more X-ray luminous that normal galaxies.

Further evidence was obtained with the optical identification of X-ray sources on deep *ROSAT* exposures. It emerged that a large fraction appear to be associated with faint galaxies (Griffiths et al 1995, Georgantopoulos et al 1996). Similar results have been obtained by Boyle et al (1995a) and McHardy et al (1995). Given the high sky density

of faint galaxies, some of these will be chance associations. Roche et al (1995) adopted a statistical approach to overcome such confusion and deduced that $B < 21$ galaxies account for $\sim 5\%$ of the X-ray sources to a flux limit of $S \sim 4 \times 10^{-15}\mathrm{ergs}^{-1}\mathrm{cm}^{-2}$. Extrapolation to fainter magnitudes would therefore suggest a much more significant fraction. Griffiths et al (1996) and Boyle et al (1995) obtained an approximate luminosity function with a small number of narrow emission-line galaxies and suggest strong X-ray luminosity evolution of the form $L_x \propto (1+z)^3$, implying a contribution to the XRB of $\sim 10 - 30\%$ at 1keV.

Cross-correlation with an entire X-ray image offers a potentially much deeper probe of the XRB. A number of authors have attempted the two-point cross-correlation between the hard (2-10 keV) XRB and various optical and infra-red galaxy catalogues (Lahav et al 1993, Miyaji et al 1994, Carrera et al 1995). These galaxy catalogues were generally fairly shallow ($z < 0.1$) but by correcting for clustering effects and extrapolating the measured local volume emissivity to z$\sim$5 it was shown that 10-30% of the XRB could be due to sources associated with galaxies. However because of the unknown error in such an extrapolation and the uncertain evolutionary properties of galaxies it is clearly desirable to probe more distant objects directly. The clearest evidence that fainter galaxies could be important contributors to the XRB came from the study of Roche et al (1995). Using the improved sensitivity and angular resolution of the *ROSAT* satellite they were able to probe fainter limits and much smaller angular scales ($\sim 15''$). Cross correlation with X-ray sources suggested a $\sim 5\%$ contribution from galaxies with $B < 21$. A much more significant result was obtained by removing the X-ray sources and cross-correlating with 3 deep (21-49ks) images of the *unresolved* XRB. The results implied that galaxies to a limit of $B = 23$ directly contribute $\simeq 17\%$ of the 1keV XRB. A simple extrapolation to $B < 28$ showed that galaxies could account for $\sim 30\%$ of the XRB or possibly much more with additional evolution at high redshift.

Thus faint galaxies may in principle explain the remainder of the XRB. The total fraction depends on their uncertain evolution with redshift.

1.1.7 Explaining X-ray luminous galaxies

As described above, there is mounting evidence for an unusually X-ray luminous population of galaxies, $10 - 100$ times brighter than normal galaxies, which may contribute significantly to the XRB. The X-ray emitting mechanism is far from clear however. As discussed in Ward et al (1993), the two most popular explanations are starburst activity and/or obscured AGN. A third explanation has recently emerged (Di Matteo & Fabian 1996) in which massive black hole remnants in the cores of galaxies undergo advection dominated accretion. We will describe these alternatives in turn:

Starforming galaxies:

Galaxies undergoing bursts of starforming activity have long been known to show higher X-ray to optical ratios than normal galaxies (Fabbiano et al 1984). David, Jones & Forman (1992) investigated the correlations between the X-ray, optical and far infra-red properties of a sample of 81 star-forming galaxies. They found a much larger dispersion in L_X/L_B than observed in more quiescent spiral galaxies. They also found that the 'excess' X-ray luminosity was proportional to the far infra-red luminosity at $60\mu m$. This strongly suggested a model in which the X-ray emission has two components. The first component is emission from long lived low-mass X-ray binaries, as in more passive spiral galaxies. The second X-ray component is associated with the immediate star-formation rate (short lived massive X-ray binaries, supernovae, gas outflows etc.) and boosts the X-ray luminosity significantly during starbursting phenomena. Massive X-ray binaries are expected to give hard X-ray spectra very close to that of the residual XRB (Treyer et al 1992). This awaits observational confirmation for extragalactic systems. Outflows of gas in starburst galaxies have been certainly been observed with very high temperature gas (Heckman, Lehnert & Armus 1993). Thus starforming activity is expected to play some role in explaining the XRB, although its relative importance in relation to other alternative explanations is undetermined.

Obscured AGN:

Another popular explanation attempts to explain the XRB in terms of unified schemes for AGN (Antonucci 1993). Broadly speaking, the primary spectroscopic classification for low redshift AGN are into Seyfert 1 galaxies, with broad permitted lines and a strong continuum, and Seyfert 2 galaxies which show only narrow emission lines and relatively weak continua. Broader emission lines are caused by clouds closer to the central ionising source orbiting at higher orbital velocities. In type 2 AGN the broad line region is believed to be obscured from view by the presence of a thick molecular torus and thus a Seyfert 2 would show the properties of a Seyfert 1 if viewed from another angle. In support of this picture, polarization studies reveal that some Seyfert 2 do indeed harbour Seyfert 1 nuclei by observing broad lines in flux scattered into our line of sight (Antonucci & Miller 1985, Miller & Goodrich 1990). In Seyfert 2 with a relatively low column density, it should also be possible to see through the obscuring material in the infra-red band since the attenuation falls at longer wavelengths. In many cases, broad emission lines have indeed been seen in infra-red hydrogen recombination lines such as Paα and Brγ (Blanco, Ward & Wright 1990, Hines et al 1991). Further evidence is provided by X-ray observations which reveal distinctive absorption features associated with a large column of obscuring material along the line of sight (Mulchaey et al 1992, Awaki et al 1991).

Recent modelling has shown that the entire 5-100keV XRB and $\sim$ 70% of the

XRB can be explained in terms of these unified schemes in which there are a range of obscured and unobscured AGN (Madau et al 1994, Comastri et al 1995). A key feature of these models is the existence of a substantial unidentified population of obscured AGN with a distribution of column densities in the range $N_H = 10^{21} - 10^{25}\mathrm{cm}^{-2}$ over a wide range of redshifts. The predicted ratios of Seyfert 1 to Seyfert 2 nuclei is approximately 1:3, in good agreement with a complete optically selected sample of Seyfert galaxies (Huchra & Burg 1992). There are two untested assumptions in such models. The first is that unobscured and obscured AGN should show the same evolutionary properties. The second is the assumption that high luminosity QSOs should show the same distribution of column densities as low luminosity Seyferts.

Ion supported tori:

A model has been proposed recently by Di Matteo & Fabian (1996) in which the XRB can be explained by galaxies containing supermassive black hole remnants from earlier quasar epochs. For accretion at low Eddington efficiency, this can lead to advection dominated accretion with an optically thin, hot ion torus in which the ions are much hotter than the electrons. The electron temperature then saturates at ~ 100 keV and since the gas is optically thin it emits a thermal Bremsstrahlung spectrum. The X-ray spectra from such sources integrated over a range of redshift can then accurately reproduce the XRB. This model can also be directly tested since it predicts a second emission peak at radio wavelengths due to emission from hot ions. The distinctive rise in the high frequency radio spectrum is in principle distinguishable from other known sources of radio flux.

1.1.8 Summary

The origin of the X-ray background remains a major unsolved problem. We now know that only a negligible fraction of this radiation can be due to a diffuse hot gas (such as an intergalactic medium). QSOs can account for $\sim 30-50\%$ of the XRB at soft energies. Explaining the entire XRB with QSOs, particularly at harder energies, seems increasingly unlikely given their X-ray spectra, number count distribution and clustering properties.

There are indications that a population of unusually X-ray luminous galaxies may account for a significant fraction of the XRB. The precise contribution is still uncertain and depends on the poorly constrained X-ray luminosity evolution. It is also vital to measure the X-ray spectra of these galaxies. Only if their spectra are significantly harder than QSOs can they provide the solution to the origin of the XRB.

The nature of the X-ray emitting mechanism in such galaxies is also unclear.

Starburst activity, obscured AGN or advection dominated accretion are possible solutions. We will discuss possible future observations that may distinguish between these competing theories in Chapter 6.

1.2 QSO X-ray variability

In the standard model for quasars and AGN the energy is generated by accretion onto a supermassive black hole (Rees 1984). The spectacular results obtained recently with the *ASCA* satellite provide strong evidence for this model with the discovery of very broad ($> 50,000$km s^{-1}) iron K lines in the X-ray spectra of nearby active galaxies (Mushotzky et al 1995, Iwasawa et al 1996). The most likely explanation is Doppler broadening due to the emitting material orbiting a very massive compact object. Such profiles cannot be explained by the competing starburst model for AGN (Terlevich et al 1993).

The X-ray flux from AGN also exhibits variability on shorter timescales than any other waveband, indicating that this emission occurs in the innermost region of the central engine (McHardy 1990, Grandi et al 1992). Detailed studies of X-ray variability can therefore act as important probes of the AGN phenomenon. Short timescale variations have already shown that AGN generate their vast energy output within a very confined space (Terrell 1967). A substantial change in flux cannot occur more rapidly than the light crossing time of the source, allowing an upper bound on the X-ray emitting size scale.

The *Ariel* $-$ *V* sky survey revealed that large amplitude variability ($\delta I/I \sim 1$) was common in Seyfert 1 galaxies on timescales of days (Marshall et al 1981) and in some cases even on scales of hours (Tennant & Mushotzky 1983, Marshall et al 1983). Assuming that the majority of these sources are not relativistically beamed, this immediately suggests an emitting region smaller than light days in diameter. Using observations taken with the *EXOSAT* satellite, Grandi et al (1992) found evidence for variability on timescales less than one day in $\sim 40\%$ of AGN. This variability is most frequently of fairly low amplitude ($\delta I/I < 1$) although a number of notable exceptions have been found. In NGC4051 and MCG-6-30-15 for example large amplitude variations (a factor of two and greater) are consistently found on timescales less than one hour (Kuneida et al 1990, Yaqoob 1992, Reynolds et al 1996). So far only models invoking accretion onto supermassive, compact objects can produce large amplitude variability on such short timescales.

Significant advances were made with the 'long look' observations taken with the *EXOSAT* observatory. The high orbit of this satellite and its much improved sensitivity

allowed continuous 200,000s observations of a small number of local AGN with high signal to noise. Visually the light curves appear very random in nature. Fourier and spectral analysis revealed no preferred timescales or periodicities over the frequency range $f = 10^{-3}$ to 10^{-5} Hz. Instead these sources showed power smoothly distributed over a wide range of frequencies, generally with power spectra of the form $P(f) \propto f^{-1.5}$ (McHardy & Czerny 1987, Lawrence & Papadakis 1993). Such light curves are described as *red noise*, ie. scale free but with more power at low frequencies. The power spectra are eventually expected to flatten from a power law form at the lowest frequencies below $\sim 10^{-5}$ Hz (McHardy et al 1990, Abraham and McHardy 1989). Similarly, at high frequencies we expect a cutoff corresponding to the smallest scales in the emitting region (eg. the inner region of the accretion disk) but so far no such steepening has been observed.

The challenge for physical models is now to explain this very characteristic form of X-ray variability. To date no consensus has arisen on how this can be reproduced in a relatively parameter free manner. Short timescale variability cannot arise from global changes in the accretion rate since the viscous timescale in the accretion disk is too long. One explanation is the shot noise model in which a large number of uncorrelated events (eg. shocks or reconnecting magnetic field lines) appear at random intervals and decay exponentially. Such models yield f^{-2} power spectra, steeper than those generally observed, but can be made to fit observations by tweaking the particular range of decay timescales (Papadakis and Lawrence 1993). A better fit to the data has been obtained by Abramowicz (1991) by modelling a distribution of hot spots on a rotating accretion disk. Modulation of the X-ray flux occurs due to Doppler beaming or possibly periodic occultation. However, the number of free parameters in this model (describing spot size, lifetime and radial distribution) suggest that a more specific physical mechanism is required to truly explain the observed X-ray variability.

Problems arise in temporal spectral analysis if the variability is governed by a small number of variables rather than being truly stochastic. Power spectrum techniques will then no longer be valid. This situation would arise, for example, if an X-ray emitting cloud of electrons varied in a coherent manner, as opposed to the shot noise or hot spot models of random, uncorrelated events. However, work by Krolik & Done (1993) has shown that the light curves of 5 Exosat AGN are incoherent to a high level of significance, ie there is no relation between the phase and frequency of the Fourier components. This would appear to rule out models with simple coherent oscillators, but the processes underlying the variability in QSOs are still poorly understood.

Interesting results have been obtained by comparing the variability in different QSOs, suggesting that more luminous sources vary with lower amplitude. Barr and Mushotzky (1986) studied the shortest timescale required for a source to double in flux and observed an increase in doubling timescale with luminosity. Green et al (1993) stud-

ied the power spectra of *EXOSAT* AGN and found that the power at a given frequency decreases with luminosity with the form $Amp. \propto L_x^{-1/3}$. Similar results were obtained independently by Lawrence & Papadakis (1993) who deduced that the amplitude falls with luminosity as $L_x^{-0.5}$. Such trends might be explained if more luminous sources are physically larger in size.

Very little work has been carried out on the variability characteristics of more luminous QSOs however, particularly at high redshift. Since QSO activity is known to have peaked at a redshift of $z \simeq 2$ (Boyle et al 1993) it is now vital to establish whether the trends observed in local AGN apply to the QSO population as a whole.

Chapter 2

Identifying X-ray Sources

In this chapter I describe the optical identification of X-ray sources on two new deep *ROSAT* fields. The discovery of a rare narrow-line QSO is also discussed.

2.1 Introduction

The X-ray background (XRB) was the first cosmic background radiation to be discovered. The first clear detection was made during a rocket flight intended to study solar X-rays reflected from the moon. Instead, the first non-solar X-ray source (Sco-X1) was identified along with an isotropic, seemingly diffuse glow of X-ray emission (Giacconi et al 1962) identified as the XRB. Despite over 30 years of study, the origin and nature of this radiation remains a major unsolved problem. The most significant progress has been made in the soft X-ray band below 3keV since the launch of high resolution imaging satellites such as *Einstein* and more recently with *ROSAT*. The launch of the *ROSAT* X-ray satellite has allowed us to detect X-ray sources at least an order of magnitude fainter than ever before. Using the deepest *ROSAT* exposures (Hasinger et al 1993) up to 70% of the $0.5-2\,\mathrm{keV}$ XRB can now been resolved into discrete sources.

We have undertaken a major observational programme to identify X-ray sources at the faintest flux limits in an attempt to understand the nature and origin of the cosmic XRB. The first field (QSF3) was centred on the ultra-violet excess (UVX) survey field of Boyle et al (1990). Spectroscopic follow up observations revealed that QSOs account for over 50% of the X-ray sources and could directly explain $\sim 30\%$ of the total XRB flux (Shanks et al 1991). A further four fields were acquired, allowing 128 QSOs to be identified in total. This allowed an accurate determination of the QSO X-ray luminosity function and its evolution (Boyle et al 1994). Extrapolating the QSO luminosity function and/or source number counts to faint fluxes showed that QSOs could account for up to

$\sim$ 50% of the XRB at 1keV. However it is difficult to account for the remainder unless the QSO luminosity function steepens considerably at faint levels. A further problem in explaining the XRB with ordinary QSOs is their X-ray spectra (see Chapter 5) which are significantly steeper than the spectrum of the residual XRB.

In recent years it has emerged that optically faint, X-ray luminous galaxies may be a significant new source population (Roche et al 1995, Georgantopoulos et al 1996, McHardy et al 1995). Many faint X-ray sources appear to be associated with faint galaxies, but due to the high surface density of galaxies at faint magnitudes and the limited resolution of the *ROSAT* PSPC the true galaxy contribution can only be determined statistically. By cross-correlation techniques Roche et al (1995) showed that faint galaxies could contribute $\sim$ 30% of the XRB and perhaps the entire XRB with strong evolution, The two deeper fields described here will allow us to confirm these results and investigate the galaxy population further (see Chapter 4). They will also significantly extend the X-ray source catalogue at faint flux limits below 1×10^{-14}erg $s^{-1}cm^{-2}$.

In this chapter the process of X-ray source detection and follow-up spectroscopy is described. The resulting X-ray source catalogue will be added to the original catalogue of Shanks et al (1996) for analysis in this thesis. Finally, the discovery of an obscured X-ray QSO is presented.

2.2 The X-ray source detection

To extend the Deep *ROSAT* Survey to fainter flux levels two further *ROSAT* PSPC exposures were obtained. These were centred on two of the well studied ultra-violet excess (UVX) survey fields of Boyle et al (1990). Additional X-ray data was already available from the *ROSAT* data archive, taken from the survey of Bohringer et al (in preparation). These serendipitous pointings were offset 5.6 and 6.9 arcminutes from our field centres and provided an additional $\sim$ 20ks of X-ray data. Table 2.1 gives details of the final exposure times, field centres and the line of sight column densities of galactic hydrogen. Being some distance from the galactic plane, the absorption by neutral hydrogen is relatively low which aids faint source detection.

The *ROSAT* PSPC is sensitive over the energy range 0.1 – 2.4 keV. Due to considerable contamination from galactic emission and geocoronal X-rays below 0.5 keV (Snowden and Freyberg 1993), the source detection efficiency was optimised by restricting the analysis to the 0.5 – 2.4keV energy band. Data from periods of high particle background were also removed from the analysis, excluding approximately 10% of the data when the Master Veto Rate exceeded 170 counts s^{-1} (Plucinsky et al 1993). Treat-

Field	RA	DEC	N_H	Exposure time
BJS855	$10^h46^m24^s$	$-00°21'00''$	2.9 ± 0.4	57147s
BJS864	$13^h43^m43^s$	$-00°15'00''$	2.6 ± 0.3	52466s

Table 2.1: Summary of deep *ROSAT* fields, with coordinates in J2000 and galactic column density in 10^{20} atom cm^{-2}.

ing the additional archive data in the same way, final mosaics of the image data were produced. The BJS864 field is shown in Figure 2.1 binned in 15″ pixels. As can be seen from this image, the point spread function of the *ROSAT* PSPC degrades rapidly beyond a 20 arcminute radius, leading to a sharp fall in sensitivity (Hasinger et al 1992). As a direct consequence the positional errors are also poor beyond this radius which hampers the identification of unique optical counterparts. A further problem is the obscuration from the support structure of the PSPC in the outer regions which can lead to inaccurate flux estimates. To avoid these problems only the sources detected within 18 arcminutes of the primary field centre were used in the analysis. Within this radius the expected vignetting is $< 12\%$ in the $0.5 - 2$ keV band.

The standard Point Source Search (PSS) detection algorithm was used to detect X-ray sources on these images. This procedure not only detects peaks above a given significance threshold, the standard 'flux in a box' technique, but also fits a model PSF to the observed distribution to determine whether or not a source is real. This was carried out with Dr Gordon Stewart and produced 4σ source lists containing ~ 60 sources within the central 20 arcminute region of each field.

2.3 Obtaining X-ray fluxes

To obtain flux estimates for X-ray sources on these fields the original exposures and serendipitous pointings were treated separately before combining. A critical aspect in this procedure is the determination of the sky background. For each dataset this was measured by removing the identified sources and analysing the remaining background. The source subtracted images showed no evidence for any significant background gradients (which can occur from contamination due to solar scattered X-rays or irregularities in the galactic background). The background subtraction was then performed using the residual image measured in concentric radii of 2 arcminute width. The background strip appropriate to the radius of each source was used. This allows for the variation in the PSPC response and PSF with off-axis angle. For each source the $0.5 - 2$ keV photon counts were obtained from circular regions large enough to capture 90% of the source photons. The required radii were calculated assuming the spectra have a mean photon

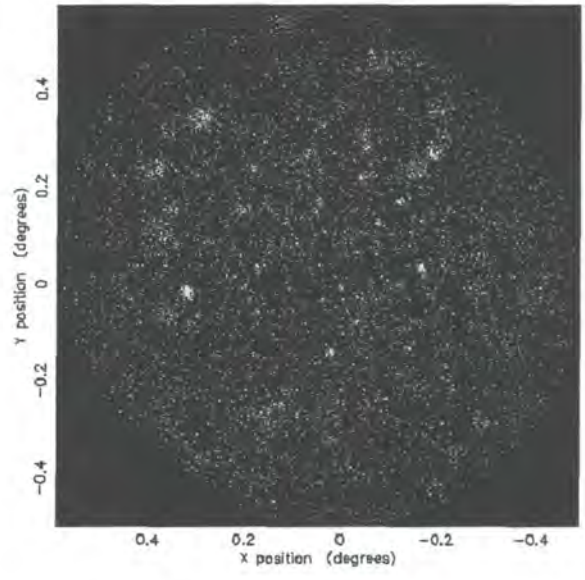

Figure 2.1: Deep (52ks) *ROSAT* PSPC image of the BJS864 field obtained from a mosaic of two exposures offset by 6 arcminutes

index of $\Gamma = 2.0$ (see Chapter 5) and varied from $30''$ on axis to $\sim 60''$ for a source at 18 arcminutes off-axis. Note that the background image was obtained by subtracting sources using significantly larger (98%) exclusion radii.

Before converting photon counts into X-ray flux several instrument correction factors were taken into account. The non-energy dependent factors due to dead-time and the obscuration by wires amount to a multiplicative factor of ~ 1.3 for each source. A vignetting correction was applied using the theoretical vignetting as a function of radius (Briel et al 1994). Photon counts were then combined from the two offset exposures. To convert detected count rates into flux the on-axis effective area of the PSPC was used assuming a mean power law spectrum of $\Gamma = 2.0$ (see Chapter 5). This leads to a conversion factor of 1.2×10^{-11}erg s^{-1}cm^{-2} to convert count rates into $0.5 - 2.0$ keV flux.

2.4 Obtaining optical counterparts

Optical counterparts to the X-ray sources were obtained from COSMOS automated scans of photographic plates taken with the Anglo-Australian Telescope. This optical data was previously used for the galaxy clustering and number count analyses of

Stevenson et al (1985) and Jones et al (1991). Sources detected by COSMOS to a magnitude limit of $b_j \sim 23$ were separated into stellar and galaxy candidates. Further U, R, I band photometry was added by matching with scans from other colour plates. Further details of the plate reduction and zero point magnitude calibration are given in Jones et al (1991). Astrometric solutions to convert plate co-ordinates into right ascension and declination were already in existence from the UVX QSO survey of Boyle, Jones and Shanks (1991) with rms errors < 1 arcsecond. In order to cross-correlate these positions with X-ray sources a second transformation was required to convert into X-ray (x,y) co-ordinates and vice-versa. This was performed using ~ 10 UVX QSOs and stars with definite counterparts on each *ROSAT* image. These gave 6 coefficient astrometric transforms with rms positional errors of 7.1 and 8.4 arcseconds for the BJS855 and BJS864 fields respectively. Such positional errors are expected given the angular resolution of the *ROSAT* PSPC (Briel et al 1994).

Optical counterparts to these X-ray sources were obtained by cross-correlating with the optical catalogue. The nearest object with an optical magnitude $b_j < 23$ was taken as a trial optical counterpart to each source. In $\sim 90\%$ of cases a candidate was identified within a 15 arcseconds radius but the search area was extended to a maximum radius of 30 arcseconds if required. In a minority of cases ($\sim 3\%$) two possible optical counterparts could be identified. In such cases, where possible, both candidates were observed. When observing constraints prevented this the most likely X-ray source was chosen on the basis of the optical magnitude, colour and star-galaxy separation. As an example, a UVX stellar candidate at $b_j = 22.5$ is likely to be a QSO (Boyle, Jones and Shanks 1991) and as such more likely to be the X-ray source than, say, a galaxy candidate at the same magnitude.

Almost half of the 4σ X-ray sources were found to have a faint galaxy within a 15 arcsecond radius, either as a primary or secondary counterpart. However given the high surface density of faint blue galaxies ($\sim 10^4 \mathrm{deg}^{-2}$ at $B < 23$, Metcalfe et al 1991) we expect many of these to be chance associations. Essentially, if we look deep enough we can find a galaxy counterpart to any X-ray source. The true galaxy contribution to the X-ray source counts can only be determined statistically and will be discussed in Chapter 4.

2.5 Obtaining optical spectra

Optical spectra were obtained during 4 dark nights at the 3.9m Anglo-Australian Telescope. Using the *AUTOFIB* multi-fibre system developed by Parry et al (1986) up to 60 spectra could be obtained simultaneously. By a fortunate coincidence the field of view of the AUTOFIB system coincides almost exactly with the 40 arcminute central

diameter of the *ROSAT* PSPC, making it an ideal instrument for this work. Typically 20 fibres were allocated to observe the sky background. This allowed ~ 40 objects to be observed in each AUTOFIB configuration. Four separate sets of fibre bundles were used to guide the telescope, using fiducial stars of magnitude $V \sim 14$. Two configurations were set up for each field, divided approximately into "bright" and "faint" objects, which allowed most of the 4σ counterparts to be observed. Light was fed along the fibres of the AUTOFIB instrument into the RGO Spectrograph which gave spectra with an effective wavelength coverage of $3500 - 7500$Å with a resolution of 12Å width, with 4Å sampling on the CCD.

During the observing a Cu/He arc lamp was regularly observed for the purposes of wavelength calibration. Twilight sky flat-field exposures were also taken at the beginning and end of each night. On two of the four nights $3 - 4$ hours were lost due to drifting cloud. Photometric conditions were not essential however since the objective was to classify objects from their spectral features. Fluxing a spectrum obtained with the AUTOFIB system is almost impossible due to differential atmospheric refraction and the varying spectral responses of the fibres.

Unfortunately, substantial additional light loss was encountered due to pointing problems with the AUTOFIB system, despite $< 0.6''$ rms errors in the positions of guide stars. This led to fibres being placed randomly up to ~ 2 arcseconds from the position of the object in the focal plane, causing considerable light loss from some objects. This problem is as yet unresolved but may be due to the unusually cold conditions encountered during the observing run causing fibre heads to "stick" during placement (Boyle, private communication). Nevertheless, positive identifications were obtained for 72 of the 113 optical counterparts.

2.6 Reduction Of Optical Spectra

The optical fibre data was reduced using the IRAF data reduction package. The reduction procedure was implemented as follows:

- All data frames were bias subtracted using an overscan region present on each exposure. This was carried out with the **ccdproc** task. Bad pixel rejection was also implemented to eliminate cosmic ray events.
- The arc frames were visually blinked against each other to check for shifting in the arc lines before and after the object field was observed. In the vast majority of cases no shift was seen (at the < 1 pixel level). However, if a shift was detected the frames containing night sky lines at the correct wavelengths were used (see below

for wavelength calibrations).

- Spectra were extracted from the object frames using the **dofibers** task in the IRAF package. This is a multi-task procedure which automatically detects fibre apertures on the CCD image. Spectra are then extracted and flat field corrections applied. The arc frames were calibrated in a semi-automated way using a range of Cu/He emission lines from an arc lamp. After a trial fitting to the brightest lines a low order polynomial fit was applied to $\sim$ 8 emission lines in the region 3500-7500Å. Object spectra are then wavelength calibrated using this fit. These fits were further checked using the positions of sky lines in the object frames. The sky spectra were then combined and subtracted from the object spectra. All of the above procedures were carefully monitored at every stage and any errors made by the automated process were corrected. The results of this procedure are a set of wavelength calibrated, sky subtracted object spectra for each 2000 second exposure.

- The spectra obtained above were then combined using the **scombine** task with an average sigma clipping procedure, rejecting pixels from frames $\pm 4\sigma$ from the mean. Finally for clarity any remaining sky lines are removed manually. The final spectra from both *ROSAT* fields are shown in Appendix A.

2.7 Catalogue of identifications

The final reduced spectra were identified with the help of Dr Brian Boyle using the **splot** task in the IRAF package. In agreement with studies of the previous fields, the sources appear to be a mixture of AGN, late type stars and galaxies with a range of morphological types.

13 X-ray sources were identified as stars, all of late type (F,G,K,M). These account for $\sim$ 10% of X-ray sources.

QSOs were primarily identified on the basis of broad emission lines $> 2000 \mathrm{kms}^{-1}$ in Lyα, CIV, CIII and MgII. In total 21 new QSOs were discovered in addition to the 18 UVX QSOs already identified as sources on these fields. QSOs account for 35% of the 4σ X-ray sources and 50% of the identified sources, in agreement with the analyses of the first five fields (Boyle et al 1994).

Of the optical counterparts classified as galaxies, 21 were confirmed by spectroscopy. These are included in the catalogue although some are likely to be spurious associations with X-ray sources. The true galaxy contribution can only be determined statistically. In Chapter 4 we demonstrate that $B < 23$ galaxies account for $21 \pm 6\%$

of the 4σ X-ray sources by direct cross-correlation. Establishing exactly which sources are associated with galaxies is difficult however due to the high surface density of faint galaxies at these magnitudes ($\sim 10^4\,\mathrm{deg}^{-2}$, Metcalfe et al 1991). Nevertheless, at brighter optical magnitudes the confusion problem becomes less pronounced. Therefore a subsample of the "most probable" X-ray luminous galaxies are selected. These are the objects with optical magnitudes $B < 21.5$, having optical counterparts positively identified as galaxies by spectroscopy and all lying within 20 arcseconds of an X-ray source. By cross-correlation techniques (see Chapter 4, Section 4.2.4) it is shown that $\sim 20\%$ of such galaxies identified on these fields are likely to be spurious identifications. As described in Griffiths et al (1995) the strength of the CaII H & K break in the optical spectra near 4000Å indicate a range of morphological types. Approximately half show strong OII emission lines (equivalent width $>$ 10Å) which suggest active starforming activity. Thus starburst phenomena may be important in explaining some of the X-ray emission, but clearly cannot explain all of these galaxies. Without the spectral coverage to obtain redshifted Hα/[NII] (or Hβ/[OIII]) it is also difficult to distinguish starburst galaxies from Seyfert 2. In a similar survey at brighter magnitudes (Boyle et al 1995a), high resolution spectroscopy reveals a mixture of these types in roughly equal proportion, although the distinction is ambiguous in many cases. The X-ray luminous galaxies will be discussed further in Chapters 4, 5 and 6.

The final catalogue of 4σ X-ray sources is given in Appendix B. Analysis of the source number distribution will be presented elsewhere (Georgantopoulos et al, in preparation). The results are consistent with the study of the first five fields (Georgantopoulos et al 1996) and show a flattening in the source number counts away from a Euclidean relationship at faint fluxes below $1 \times 10^{-14}\,\mathrm{erg\ s^{-1}cm^{-2}}$. In particular the QSO counts turn over more rapidly than the remaining sources, suggesting the emergence of another source population. The inclusion of these QSOs into luminosity function studies will also be presented elsewhere (Boyle et al, in preparation).

In Chapter 3 this catalogue will be combined with the 128 QSOs identified from the first 5 *ROSAT* fields (Shanks et al 1996, in preparation) to investigate the X-ray variability characteristics of this QSO population. In Chapter 4 a detailed study of the faint galaxy contribution to the X-ray background will be carried out. This will be followed in Chapter 5 by a study of the X-ray spectra of the entire source population to investigate the problem of the "spectral paradox" of the XRB.

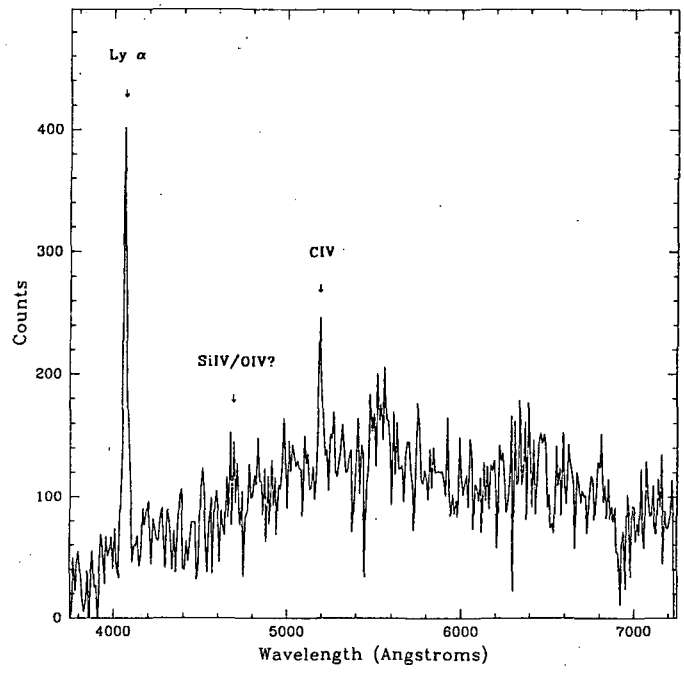

Figure 2.2: Low resolution (12Å) optical spectrum for RXJ13434+0001. The prominent emission lines are marked.

2.8 The discovery of a high redshift obscured QSO

In addition to the broad line QSOs an unusual object was identified on the BJS864 field. AAT plates identify this source, named RXJ13434+0001, as a star-like object at $b_j = 22$, only 3″ from the X-ray source position.

The optical spectrum is shown in Figure 2.2. Identification of the lines as Lyα and $C_{IV}\lambda1549$ give a redshift of $z = 2.347 \pm 0.006$, implying an absolute magnitude of $M_B = -23.7$ ($H_0 = 50\,\mathrm{km\,s^{-1}Mpc^{-1}}$, $q_0 = 0.5$). Taking into account the instrumental resolution, the full width at half maxima for the Lyα and CIVλ1549 emission lines are $900\,\mathrm{km\,s^{-1}}$ and $< 700\,\mathrm{km\,s^{-1}}$ respectively. Local objects with strong, narrow emission lines are generally classified as Seyfert 2 or starburst galaxies. However, the existence of highly ionized C_{IV} suggests the presence of a strong non-thermal ionizing source, inconsistent with being a starburst galaxy. Given its high optical and X-ray luminosities, we therefore classify $RXJ13434+0001$ as a rare example a narrow-line QSO (Stocke et al 1982, Elizalde & Steiner 1994) and possibly the first detected by X-ray selection.

For comparison, all of the 167 QSOs identified in this survey and the 400+

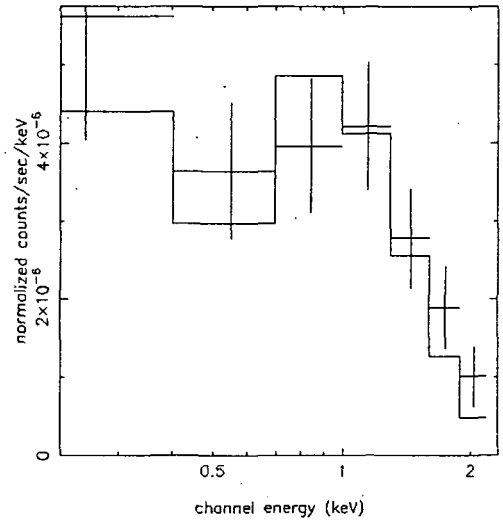

Figure 2.3: The observed $0.1-2\,\mathrm{keV}$ X-ray spectrum with the best fitting power law model ($\Gamma = 1.56$) modified by galactic absorption.

QSOs from the Durham survey (Boyle et al 1987) show broad emission lines with FWHM $> 2,500$ km s^{-1}. Obscuration of the inner broad line region is clearly one explanation for $RXJ13434+0001$, making it an example of the long sought after luminous equivalents to Seyfert 2 galaxies. X-ray observations do not provide conclusive evidence for this however.

$RXJ13434+0001$ is the 5th brightest source on the BJS864 field with a $0.1-2$ keV X-ray flux of 4.5×10^{-14}erg s^{-1}cm^{-2}. The best fitting power law model gives a $0.4-6.7\,\mathrm{keV}$ rest frame luminosity of $1.9 \times 10^{45}\,\mathrm{erg\,s^{-1}}$, comparable to most QSOs at this redshift. Spectral fitting was attempted by dividing the ~ 200 photons into seven spectral bins. Fixing photoelectric absorption at the galactic value of $N_H = 2.6 \times 10^{20}$ atom cm^{-2} we obtain a best fitting power law model ($\chi^2_{red} = 1.07$) with a photon index of $\Gamma = 1.56 \pm 0.17$. The raw channel spectrum and best fitting model are shown in Figure 2.3. This spectrum is somewhat flatter than the mean spectrum for QSOs, $\Gamma = 2.2 \pm 0.1$ (see Chapter 5). Repeating the background subtraction with other source free regions near this source give the same result and confirm that this is not a systematic effect.

Thus, despite having a harder spectrum than most QSOs, $RXJ13434+0001$ shows no obvious evidence for significant photoelectric absorption at soft energies. Most local Seyfert 2 galaxies show strong photoelectric absorption columns of $N_H = 10^{22}-10^{24}$

atom cm^{-2} (Mulchaey et al 1992) with a distinctive sharp spectral cut off at soft energies. For $RXJ13434+0001$ the best fitting cold absorber model gives zero for the intrinsic (ie. rest frame) absorption, but a column of $N_H = 6 \times 10^{21}$atom cm^{-2} is permitted within the 99% confidence contours (see Figure 2.4). We conclude that a moderate absorbing column could be present. Fixing the intrinsic power law at a QSO-like index of $\Gamma = 2.2$ gives a restframe neutral hydrogen column of $N_H = 2.5 \pm 1.1 \times 10^{21}$ atom cm^{-2}. The dust associated with such a column would be enough to obscure the broad line region in the ultra-violet band (assuming standard gas to dust ratios) producing ~ 6 magnitudes of absorption at Lyα.

The X-ray to optical flux ratios also suggest some absorption compared to normal broad line QSOs. An obscured model absorbs the spectrum in both bands, but for standard gas to dust ratios the relative attenuation is ~ 10 times higher in the UV than at 2keV. Fitting the standard power law between the monochromatic optical and X-ray luminosities at 2500Å and 2keV respectively we obtain a spectral index $\alpha_{ox} = 1.14 \pm 0.05$ compared to $\alpha_{ox} = 1.5 \pm 0.1$ for normal broad line QSOs, suggesting some UV extinction but only ~ 2.5 magnitudes. Thus the UV continuum is somewhat brighter than we might expect from an absorbed model. This is also evident from Figure 2.2. There appears to be sufficient absorption to obliterate broad emission lines, but not the UV continuum. This could be explained if RXJ13434+0001 had some contribution from a bright host galaxy.

We consider it unlikely that RXJ13434+0001 belongs to the rare class of narrow-line Seyfert 1 galaxies (Brandt et al 1994). These objects are generally characterised by very steep X-ray spectra with $\Gamma > 3$. Our object has a significantly flatter spectrum with $\Gamma = 1.56$. Indeed, the steep spectrum of these sources is actually invoked as an explanation for the narrow lines since a steep X-ray spectrum might interfere with the formation and confinement of broad line clouds (Brandt et al 1994). This clearly cannot be the case for our object.

When this QSO was first discovered there were two alternative explanations to the moderate obscuration scenario (see Almaini et al 1995). If $RXJ13434+0001$ has a very low absorbing column then the broad-line region cannot be obscured. This raised the intriguing possibility that we may have discovered a "naked" Type 2 nucleus. Alternatively, the obscuring column could be very large ($> 10^{24}$atom cm^{-2}) and the observed X-rays due entirely to scattered flux (Fabian et al 1994). However in March and May 1995 further observations of $RXJ13434+0001$ were made at the UK Infra-Red Telescope in Hawaii. An IRCAM3 image revealed a bright point-like object with a magnitude $K = 17^m$. This gives $B - K = 5$ compared to $B - K \simeq 2.5$ for most normal QSOs, suggesting ~ 2.5 magnitudes of nuclear UV extinction. During another observing run (the main aim of which was to obtain infra-red spectra of faint blue galaxies) a short (2000s) exposure was taken by Dr T. Shanks with the UKIRT CGS4

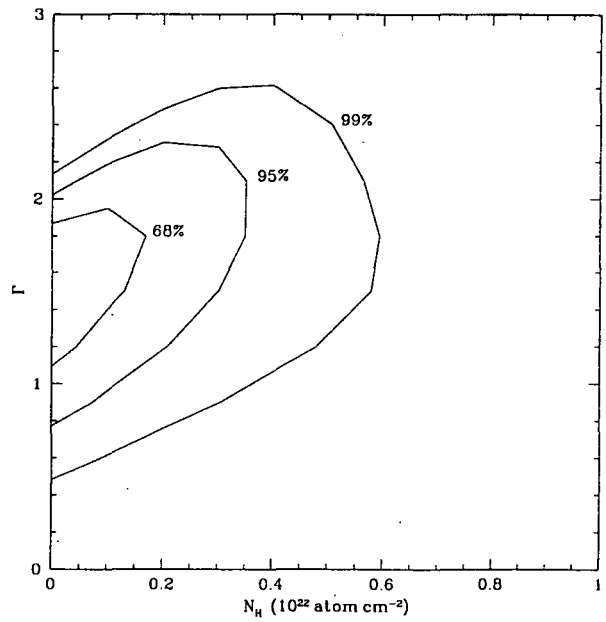

Figure 2.4: Confidence contours in the rest frame column density (N_H) *v.* photon index (Γ) plane for the X-ray spectral fits to RXJ13434+0001. The contours represent the 68%, 95% and 99% confidence regions with two interesting parameters.

infra-red spectrograph between 1.4-2.3 microns with a 2.4 arcsecond slit. This spectrum has a resolution of $\sim$ 25Å and is shown in Figure 2.5. The broad emission line at 2.2 microns coincides exactly with the expected position of the Balmer line H_α, confirming the redshift $z = 2.35$. The FWHM of this line corresponds to $\sim$ 260Å, ie. $\sim$ 3500km s^{-1}, entirely consistent with normal broad line QSOs. Thus the UKIRT observations favour the first explanation for this object, namely that $RXJ13434+0001$ is a QSO obscured by a moderate amount of gas and dust sufficient to obliterate broad Lyα and C_{IV} in the ultra-violet band but not broad $H\alpha$.

Deeper infra-red observations are required to determine the *amount* of dust obscuration. The short exposure already obtained was insufficient to detect H_β at 1.63 microns. Detection of this line would allow the degree of reddening to be assessed from the ratio of the strengths of H_α/H_β. Photoionisation models predict an intrinsic line ratio $H_\alpha/H_\beta \simeq 3$ (Netzer 1990). The same ratio is observed in unobscured QSOs and Seyfert galaxies (Francis et al 1992). This value would be changed significantly by dust reddening. The X-ray spectrum of this QSO suggests a plausible neutral hydrogen column density of $N_H = 2.5 \times 10^{21}$atom cm^{-2} which, assuming standard gas to dust ratios, would change the line ratio to $H_\alpha/H_\beta \sim 7$. Deeper infra-red observations are required to test this hypothesis and obtain an accurate estimate of the reddening.

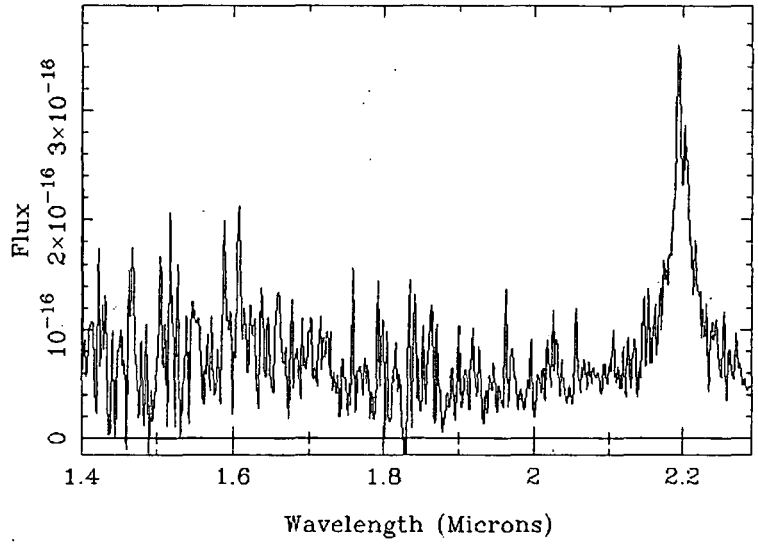

Figure 2.5: Near infra-red spectrum of RXJ13434+0001. The broad emission line at 2.2 μm corresponds to Hα and confirms that dust is obscuring the broad line in the ultra-violet band.

It is difficult to make claims on the basis of one new object, but nevertheless we note that the discovery of a population of high redshift obscured QSOs would have important implications for the origin of the X-ray background. A major problem in explaining the X-ray background with QSOs are their X-ray spectra (see Chapter 5). *ASCA* observations (Gendreau et al 1995) have shown that the extra-galactic XRB from $1-10$ keV has a flat power-law slope of $\Gamma = 1.4$ while type 1 QSOs have a much steeper slope, $\Gamma \simeq 2.2$. This suggests that a new faint population with a flatter X-ray spectrum is required to account for the remainder of the XRB . Recent modelling (Comastri et al 1995, Madau et al 1994) has shown that the entire $5-100$keV X-ray background and $\sim$ 70% of the *ROSAT* band may be explained in the context of unified schemes in which there are a range of obscured and unobscured AGN. An important prediction of this model is the existence of a large population of previously undetected luminous obscured QSOs, many of which should be detectable at faint fluxes even in the *ROSAT* band. One explanation for the new population of narrow-line X-ray galaxies emerging from *ROSAT* surveys (eg. Ward et al 1993, Roche et al 1995, Boyle et al 1995) is that some of these galaxies contain hidden AGN. The QSO RXJ13434+0001 may therefore represent a particularly bright high redshift counterpart to these objects. If an obscured QSO population does exist at high redshift they could make a significant contribution to the X-ray background but still remain too faint for any optical counterparts to be observed on photographic plates. From an X-ray absorbing column typical of Seyfert 2 galaxies we would expect at least 6 magnitudes of extinction in the rest frame UV, corresponding

to the observed optical waveband. It is therefore not surprising that such objects have not been detected before. It may only be the presence of a bright host galaxy which permitted the detection of this particular object. This would explain the relatively high UV continuum, despite the obscuration of the broad line region. The optical counterparts to other obscured AGN in less luminous hosts would therefore remain undetected.

2.9 Conclusions

In this chapter the detection and optical spectroscopic identification of *ROSAT* sources from 2 deep fields has been described. Positive identifications were obtained for 72 of the 113 X-ray sources detected to an approximate flux limit of $S_{(0.5-2\mathrm{keV})} = 4 \times 10^{-15}\mathrm{erg\ s^{-1}cm^{-2}}$. Approximately 10% of these sources are associated with late type stars. At least 39 were firmly identified as QSOs, accounting for $\sim 50\%$ of the identified sources and in good agreement with the identifications from the first 5 *ROSAT* fields (Boyle et al 1994). Many of the remaining sources appear to be associated with faint galaxies on photographic plates to a limit of $b_j = 23$. The galaxy contribution to the X-ray background will investigated further in Chapter 4.

A high redshift ($z = 2.35$) obscured X-ray QSO was also discovered on the BJS864 field. This object shows narrow Lyα and C_{IV} ultra-violet emission lines with FWHM $< 1000\mathrm{kms^{-1}}$ suggesting that this may by a luminous, high redshift counterpart to Seyfert 2 galaxies. However, unlike most local Seyfert 2's, $RXJ13434+0001$ does not show evidence for significant photoelectric absorption. Nevertheless, the X-ray spectrum from $0.1 - 2\,\mathrm{keV}$ has a power law index of $\Gamma = 1.56 \pm 0.17$ which is somewhat flatter than normal broad line AGN (see Chapter 5). A normal QSO X-ray spectrum obscured by an obscuring column of $N_H \sim 2.5 \times 10^{21}\mathrm{atom\ cm^{-2}}$ can explain the X-ray data. The detection of broad H_α by Shanks et al (1996) confirms that a moderate level of obscuration is obscuring the UV emission lines. X-ray to optical flux ratios and the $B - K$ colour imply a very low level of reddening and suggest the need for an additional source of UV continuum emission. This is also evident from the low resolution UV spectrum. The contribution from a bright host galaxy is one possibility. Obscured QSOs may be a rare phenomena (see also Stocke et al 1982, Elizalde & Steiner 1994) but the discovery of this object raises the possibility that there may be other obscured high redshift AGN which, if found in significant numbers, would have important implications for our understanding of active galaxies and the origin of the X-ray background. It is possible that the detection of this object was permitted only by the relatively low level of obscuration. Alternatively, it may be the presence of a bright host galaxy which revealed this AGN. Obtaining the $H\alpha/H\beta$ line ratio will allow us to model the underlying spectrum more accurately to distinguish between these scenarios.

A large population of such objects could, in principle, explain the spectral hardening seen at faint X-ray fluxes (see Chapter 5) and thus account for the remainder of the XRB (Comastri et al 1994). The newly emerging population of narrow emission-line galaxies could be low redshift examples from such a population and many could be harbouring hidden AGN (see Chapters 4 & 5). However, more work is required to determine whether such obscured objects exist in sufficient numbers.

Chapter 3

QSO X-ray variability

In this chapter a study of QSO X-ray variability is presented in an attempt to quantify the variability characteristics of the QSO population as a whole. Trends in variability with luminosity, redshift or spectral shape may provide important clues in understanding QSOs and their evolution. Finally a bright, highly variable AGN is analysed in detail.

3.1 Introduction

QSO are known to emit vast quantities of X-ray radiation. The X-ray flux exhibits variability on shorter timescales than any other waveband, indicating that this emission occurs in the innermost region of the central engine (McHardy 1990, Grandi et al 1992). Detailed studies of X-ray variability can therefore act as important probes of the AGN phenomenon. Since a substantial change in flux cannot occur more rapidly that the light crossing time of the source, a large change in flux can allow an upper limit on the size of the central source (Terrell 1967)

Using observations taken with the *EXOSAT* satellite Grandi et al (1992) found evidence for variability on timescales less than one day in $\sim 40\%$ of AGN. This variability is most frequently of fairly low amplitude ($\delta I/I < 1$) although a number of notable exceptions have been found. In NGC4051 and MCG-6-30-15 for example large amplitude variations (a factor of two and greater) are consistently found on timescales less than one hour (Kuneida et al 1990, Yaqoob 1992, Reynolds et al 1996). So far only models invoking accretion onto supermassive, compact objects can produce such large amplitude variability on short timescales.

Significant advances were made with the 'long look' observations taken with the

EXOSAT observatory. The high orbit of this satellite and its much improved sensitivity allowed continuous 200,000s observations of a small number of local AGN with high signal to noise. Visually the light curves appear very random in nature. Fourier and spectral analysis revealed no preferred timescales or periodicities over the frequency range $f = 10^{-3}$ to 10^{-5} Hz. Instead these sources showed power smoothly distributed over a wide range of frequencies, generally with power spectra of the form $P(f) \propto f^{-1.5}$ (McHardy & Czerny 1987, Lawrence & Papadakis 1993). Such light curves are described as *red noise*, ie. scale free but with more power at low frequencies. The power spectra are eventually expected to flatten from a power law at the lowest frequencies below $\sim 10^{-5}$ Hz (McHardy et al 1990, Abraham and McHardy 1989). Similarly, at high frequencies we expect a cutoff corresponding to the smallest scales in the emitting region (eg. the inner region of the accretion disk) but so far no such steepening has been observed. Some of the physical models invoked to explain such variability are described in Chapter 1.

Particularly interesting results were obtained by comparing the variability in different AGN, suggesting that more luminous sources vary with lower amplitude. Barr and Mushotzky (1986) studied the shortest timescale required for a source to double in flux and observed an increase in doubling timescale with luminosity. Green et al (1993) studied the power spectra of *EXOSAT* AGN and found that the power at a given frequency decreases with luminosity with the form $P \propto L_x^{-1/3}$. Similar results were obtained independently by Lawrence & Papadakis (1993) who deduced that the amplitude falls with luminosity as $L_x^{-0.5}$. Such trends might be explained if more luminous sources are physically larger in size.

These results have all been obtained from studies of local, bright AGN. This is natural since the light curves are of high signal to noise and can be analysed in detail. They do not, however, represent a "typical" sample of the AGN population. In particular, QSO activity is known to have peaked at much higher redshift ($z \simeq 2$) and has evolved very strongly to the present day in the sense that a typical QSO is now ~ 30 time less luminous (Boyle et al 1994). In this work we present an analysis of 167 QSOs detected from our Deep *ROSAT* Survey (see Chapter 2) which represent a near complete, flux limited sample of QSOs spanning a very wide range in luminosities with redshifts $0.1 < z < 3.3$. Most of the X-ray sources presented here are detections at the faintest possible X-ray flux and hence the light curves are generally of low signal to noise. Detailed power spectrum analysis is therefore impossible. Nevertheless we will develop methods to detect and quantify the amplitude of variability, or at least place upper limits on the variability which might be present. In this way it may be possible to study the X-ray variability characteristics of a typical X-ray selected QSO population. We will also search for trends in variability with luminosity, redshift and spectral index which may be important in understanding the AGN phenomenon and its evolution.

3.2 Obtaining light curves

3.2.1 Data Reduction

In the course of optically identifying X-ray sources from 7 deep *ROSAT* fields we have discovered 167 QSOs to a flux limit of $\sim 4 \times 10^{-15}$ergs^{-1}cm^{-2} (0.5-2.0 keV). A description of the X-ray source detection and optical identification for the deepest exposures is given in Chapter 2. Details of the QSO redshift distribution and the X-ray luminosity function and its evolution are given in Boyle et al (1994). The process of obtaining light curves for variability studies is now described.

The *ROSAT* PSPC has a 2 degree field of view but is most sensitive within the central 40 arcminute diameter ring. The sources analysed here were all detected within this optimal region. The arrival of each photon is time tagged with an accuracy of a few milliseconds, which in principle should allow accurate time series analysis. Unfortunately the support structure of the PSPC causes complications. Within the central ring there are thick wires (of $\sim$12 arcseconds width) with a 4 arcminute spacing and further thin wires (of $\sim$ 3 arcseconds width) spaced at approximately 50 arcseconds . To allow for this structure the satellite switches to a 'wobble' mode when using the PSPC which moves the instrument back and forth to smooth out the shadowing of sources behind the wires ($\pm$3 arcminutes in 400 seconds). On average this process obscures 21% of the photons from a given source and effectively restricts time series analysis to timescales greater than the oscillation period. A further restriction is the 96 minute orbit of the satellite which imposes further periodic gaps on the light curves. In general a source is visible for 1000 – 2000 seconds per orbit. This restriction, combined with the effect of instrument wobble, makes it very difficult to conduct meaningful time series analysis on time scales smaller than the orbital period. However, given the faint nature of the X-ray sources studied here (typically 10^{-3} counts/second), sampling on bins of orbital length or greater is generally required to obtain sufficient photon counts per bin and allow meaningful $\sqrt{N}$ errors.

Basic data reduction was carried out using the *Asterix* X-ray data processing package. For each source, depending on the off-axis radius, a source box radius was chosen to enclose 90% of the X-ray photons. Assuming a mean QSO spectral index of $\Gamma = 2.2$ (see Chapter 5), the radius of this circle varies from 24.6″ on axis to 56.6″ at a maximum radius of 18 arcminutes. Data from periods of high particle background are excluded from the analysis. This removes $\sim$ 10% of the data when the Master Veto Rate rises above 170 counts s^{-1} (Plucinsky et al 1993). As with the spectral analysis of Chapter 5, considerable care was taken in choosing areas for background subtraction. By good fortune, none of the fields showed evidence for significant background gradients (generally caused by irregularities in the galactic background or contamination from solar scattered

Correction	Position Dep.?	Energy Dep.?	Time Dep.?
Dead time	No	No	Yes
Wires	No	No	No
Vignetting	Yes	Yes	No
PSF	Yes	Yes	No

Table 3.1: Dependence of instrument corrections

X-rays). Typically six circular areas of 4-6 arcminute radius are then chosen across the field from source free regions to perform the background subtraction. The background box closest to each source was used, with minor vignetting corrections ($< 10\%$) to correct for the differing off axis radii of source and background boxes. Normalising for the difference in area between the source and background boxes, we obtain the source photon counts in each time bin:

$$N_{source} = N_{total} - (r_S/r_B)^2 \times F_\nu \times N_{back} \tag{3.1}$$

where F_ν is the vignetting correction and r_S, r_B are the radii of the circular source and background boxes respectively.

The next step is to apply instrument corrections to the background subtracted file to allow for effects such as mirror vignetting, off-axis detector response, photon scattering and dead time. The various corrections and their dependencies are shown in Table 3.1. For time series analysis, the *Asterix* package simply multiplies the counts in each time bin by a factor for each correction. The largest of these is the correction for wires, which obscure 21% of photons per wobble. Thus we obtain the corrected photon counts:

$$N_{corr} = F\left[N_{total} - (r_S/r_B)^2 \times F_\nu \times N_{back}\right] \tag{3.2}$$

where $F = f_{dt} \times f_{wires} \times f_{vig} \times f_{psf} \simeq 1.3$ is the total instrument correction factor for each bin. From this, assuming Poisson statistics, the resulting variance for each time bin will be given by:

$$\sigma^2{}_N = F^2\left[N_{tot} + (r_S/r_B)^4 \times F_\nu^2 \times N_{bck}\right] \tag{3.3}$$

Problems may conceivably arise if the background regions themselves show differing variability across the field. Although care is taken to use background regions

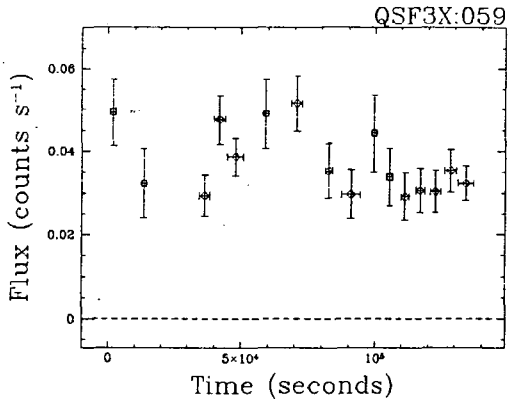

Figure 3.1: The light curve of the QSO QSF3X059.

close to each source, differential variability may nevertheless introduce extra variance into the light curves above the Poisson noise and bias the results. Some of the background boxes do indeed show evidence for variability at a low level ($\delta I/I < 10\%$), probably due to contamination from solar scattered X-rays. However, comparing the light curves from different background regions reveals the same variability across the detector. Such effects will therefore be removed in background subtraction.

3.2.2 Binning light curves

Light curves were first binned in orbital observation periods for the reasons described above. This gave $16-26$ observation slots, depending on the individual field exposure. An example of such a light curve is shown in Figure 3.1 for the QSO QSF3X:059 which has a 27ks exposure. The periodic gaps are due to the orbit of the satellite with larger gaps occurring during phases of high instrument background, such as when the satellite passes through the South Atlantic Anomaly. Many of the fainter sources give very few counts per bin and hence meaningless Poisson errors. Such sources are rebinned. Using the mean intensity of the source, if the smallest bin is expected to give fewer than 20 photons it is merged with its nearest neighbour. This process is repeated until $\bar{I}\Delta t > 20$ photons per bin.

Before the rebinning process, each light curve was visually inspected for any unusual flaring activity on short timescales which would otherwise be averaged out. No significant flares were apparent however and all light curves were rebinned as described above. From a total of 167 QSO, this process leaves 104 with a minimum of 2 time bins. The faintest 63 QSOs, with fewer than ~ 40 photons, are excluded from this preliminary analysis.

3.3 Detecting Variability

A χ^2 test was performed on each light curve to test for variability against the null hypothesis that the flux remains constant:

$$\chi^2 = \sum_n \frac{[I_n - \langle I_n \rangle]^2}{\langle \sigma_n^2 \rangle} \tag{3.4}$$

The results show that 22 of the 104 QSOs show evidence for variability with a significance $> 90\%$. Of these, 12 are significant at $> 95\%$ of which 4 are significant at $> 99\%$. The 12 QSOs with variability at $> 95\%$ significance are shown in Figure 3.2.

It is important to emphasise that the non-detection of variability in the remaining QSOs does not imply that no variability is occurring. We can only state that any intrinsic variations which may be present are overwhelmed by photon noise. In an observation of higher signal to noise some variability may have been detected. It is therefore vital to establish what amplitude of variability *could* have been detected in each QSO, given the noise and the sampling. Only then can we make quantitative statements about the "typical" variability in the population.

Simulations were therefore carried out to determine the minimum detectable variability for each QSO. Theoretical light curves with a certain intrinsic amplitude of fluctuations are produced and binned with the same sampling structure as the real QSO.

A time process $x(t)$ may be represented by its Fourier integral:

$$x(t) = \int_{-\infty}^{+\infty} X(f) e^{2\pi i f t} df \tag{3.5}$$

The power spectrum of $x(t)$ is defined as the modulus squared of the inverse Fourier transform (neglecting factors of 2π):

$$P(f) = \left| \int_{-\infty}^{+\infty} x(t) e^{-2\pi i f t} dt \right|^2 = |X(f)|^2 \tag{3.6}$$

In the simulations, rather than assuming random variability (ie. white noise) for the QSOs, I have assumed that all QSOs show the form of power spectrum observed in local Seyfert galaxies, ie. $P(f) \propto f^{-1.5}$ (Lawrence & Papadakis 1993). A general theoretical light curve can then be constructed to satisfy this spectral form:

Figure 3.2: Light curves of the 12 QSOs showing evidence for variability with > 95% significance.

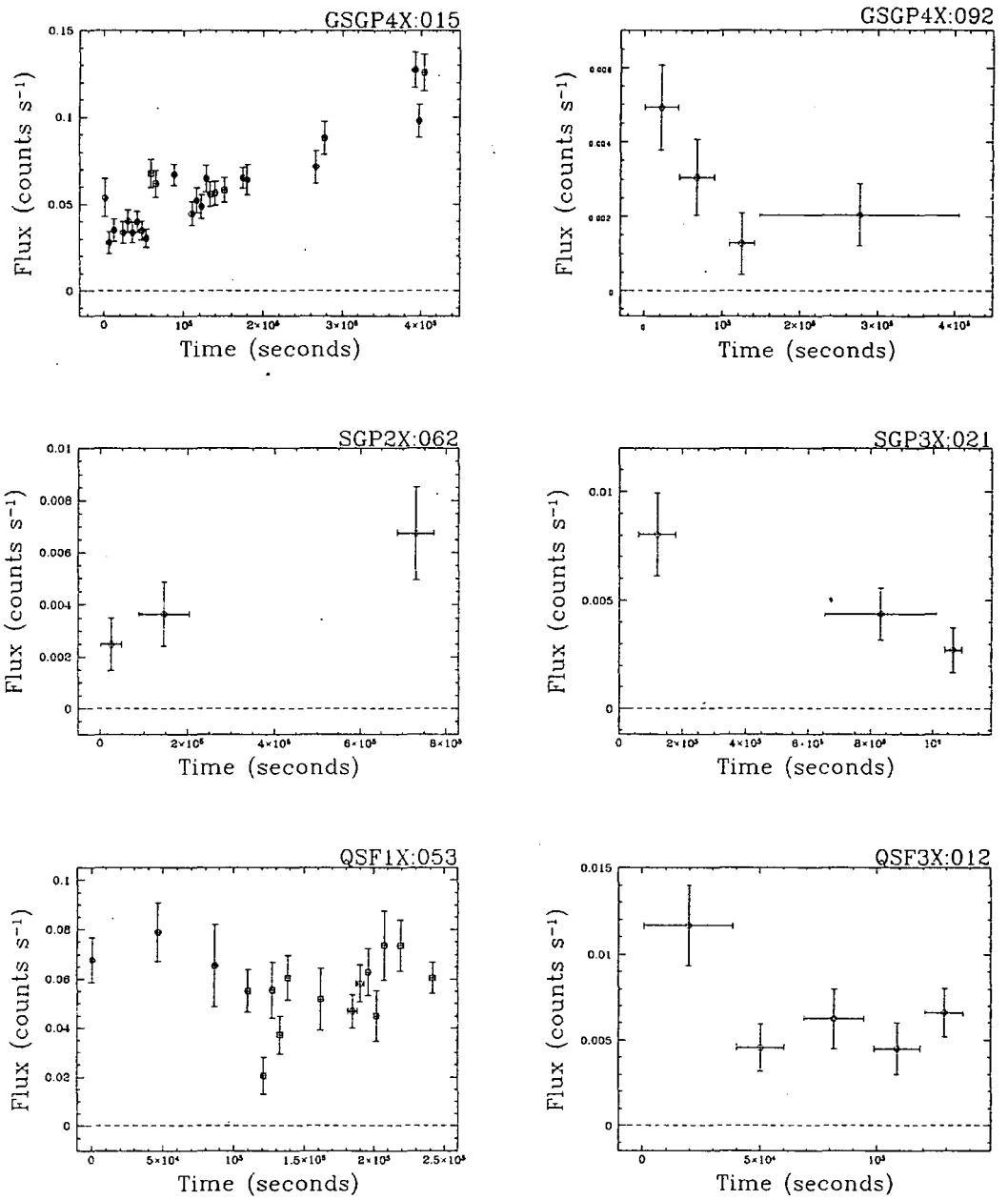

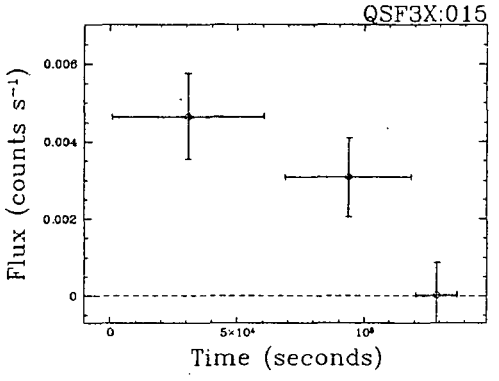
QSF3X:015
Flux (counts s^{-1})
Time (seconds)

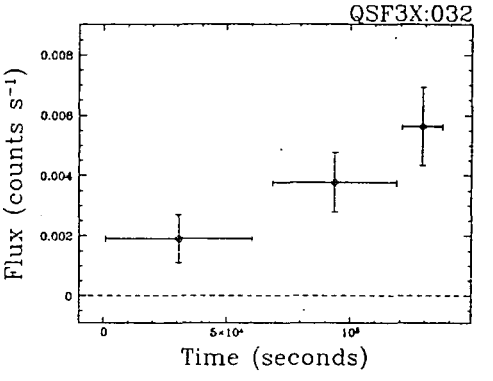
QSF3X:032
Flux (counts s^{-1})
Time (seconds)

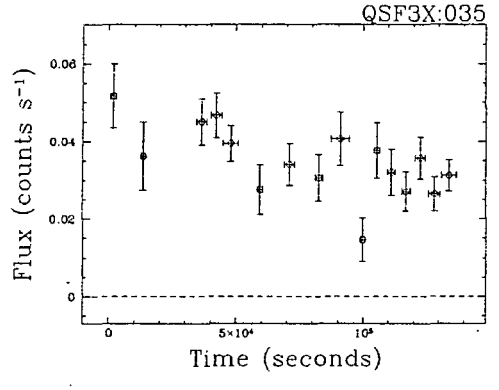
QSF3X:035
Flux (counts s^{-1})
Time (seconds)

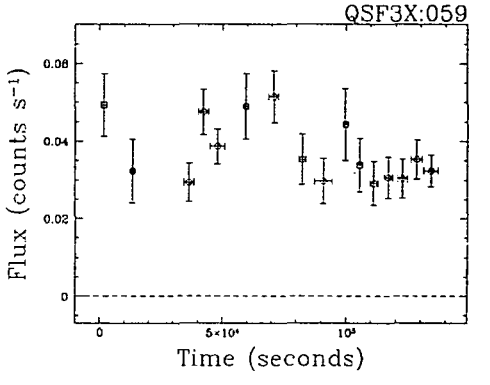
QSF3X:059
Flux (counts s^{-1})
Time (seconds)

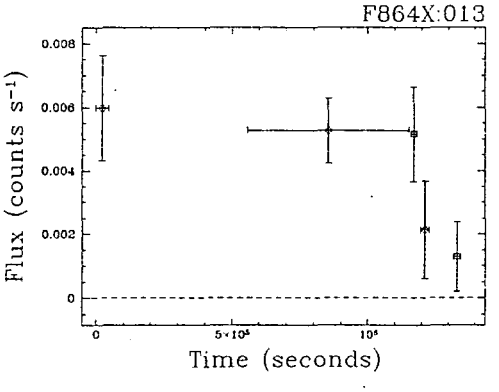
F864X:013
Flux (counts s^{-1})
Time (seconds)

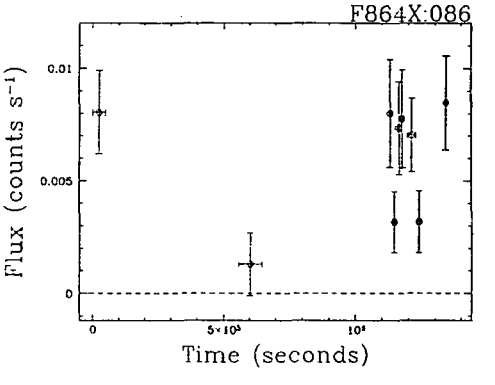
F864X:086
Flux (counts s^{-1})
Time (seconds)

$$x(t) = \int_{-\infty}^{+\infty} |P(f)|^{1/2} e^{i[2\pi ft - \phi(f)]} df \tag{3.7}$$

where the real function $\phi(f)$ represents the phase information lost by the power spectrum method. However, in a stochastic random process governed by a large number of variables we expect no relation between the phase and frequency of Fourier components, and indeed this has been shown for a number of *EXOSAT* AGN (Krolik & Done 1993). The light curves were therefore simulated using a random phase $\phi(f)$. Sampling x(t) over discrete time intervals t_k, the Fourier integral collapses into the discrete Fourier transform and we obtain:

$$x(t_k) \propto \sum_{f_{min}}^{f_{max}} |P(f)|^{1/2} \cos[2\pi f t_k - \phi(f)] \tag{3.8}$$

The lowest contributing frequencies are chosen at 10^{-6} Hz to agree with measurements of McHardy et al (1990). The high frequency cut off (the Nyquist frequency) was chosen at an arbitrarily high value of 2×10^{-3} Hz, ie. $\frac{1}{500s}$, at the current limit of power spectrum observations (Green et al 1993). The resulting light curve is then corrected to allow for the redshift of the galaxy (viz. all times multiplied by $1 + z$) and a random section chosen and rebinned on the same sampling structure as the real QSO. To obtain the required amplitude of variability, the light curves are scaled and a flat d.c. component added to give a total variance of the required amplitude. Variances giving root mean squared amplitudes in $\delta I/I$ at levels from 10% to 150% were used.

Poisson noise was then added to these light curves, using the error bars from the real data. For each QSO, 1000 simulated light curves were produced for each level of variability amplitude and χ^2 tests preformed to establish whether the variations are detectable. If variability is detected at the 90% confidence level in 90% of the simulations, then variability of that amplitude is considered "detectable". The results of these simulations are summarised in Table 3.2, showing the number of QSOs with sufficient S/N to detect variability at each amplitude.

We may now interpret the significance of the variable QSOs. Only 22 of the 104 QSOs showed variability with $> 90\%$ significance, which implies that ~ 10 of these might be spurious. However, at higher signal to noise the fraction of variable objects increases. Taking only the 15 QSOs with sufficient S/N to detect variability of $\sim 40\%$ rms, we find that 10 are detected as variable. Of the 7 QSOs in which 30% variations were detectable, 6 were found to be significantly variable. Thus the results imply that with sufficient S/N most QSOs might show evidence for low level variability. We will now attempt to measure the amplitude of variations.

	S/N →							
Detectable variability (rms)	150%	100%	75%	50%	40%	30%	20%	10%
Number of QSOs	104	80	59	29	15	7	1	-
(Number of variables)	(22)	(22)	(19)	(13)	(10)	(6)	(1)	-

Table 3.2: Showing how the fraction of variable QSOs increases with higher signal to noise. The number of QSOs with sufficient S/N to detect *intrinsic* rms fluctuations of a given amplitude are shown. The subset of these QSOs which actually show evidence for variability are also shown.

3.4 The amplitude of variability

We will now attempt to directly measure the amplitude of intrinsic variations in each QSO. Although most are too faint to enable a significant detection of variability we can nevertheless place upper limits on the amplitude of fluctuations which could be present. In this way it may be possible to combine QSOs with variability just below the level of significant detection and hence obtain meaningful results overall.

Unlike the well studied light curves of *EXOSAT* AGN, the QSOs studied here are too faint to obtain variability amplitudes by detailed power spectrum analysis. A simpler method is to estimate the intrinsic variance in the light curve. Since this quantity is proportional to the amplitude of the power spectrum (Chatfield 1976) it will also allow comparisons with previous work. In order to compare objects of different flux in a meaningful way, all light curves are first divided by their mean flux. Hence we are measuring the amplitude of *fractional* variability.

The variance in the light curve has two components: first there may be fluctuations due to intrinsic variations in the QSO and secondly there will be a component due to noise (ie. Poisson errors from the source and background). These components are related simply via:

$$\sigma^2_{total} = \sigma^2_{intrinsic} + \sigma^2_{noise} \tag{3.9}$$

Therefore to estimate the intrinsic variations we must subtract expected variance due to noise, which is simply the square of the error on the mean flux. Hence we obtain:

$$\sigma^2_{intrinsic} = \sum_{n=1}^{N} \frac{(I_n - \bar{I})^2}{N-1} - \sigma^2(\bar{I}) \tag{3.10}$$

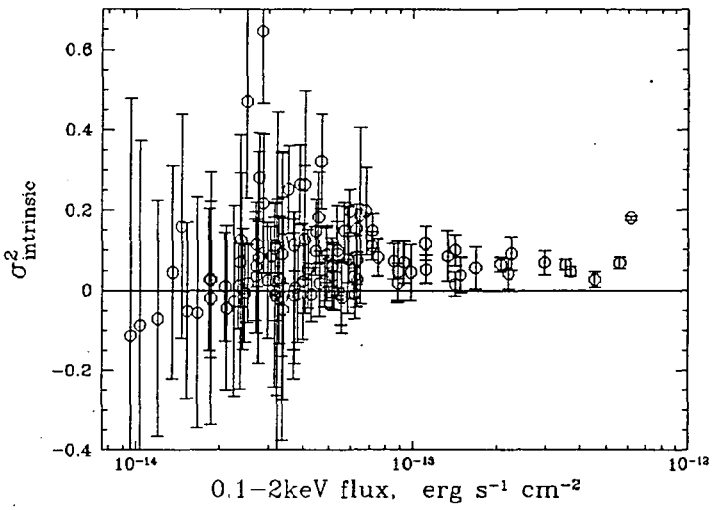

Figure 3.3: Showing the intrinsic, noise subtracted variance in the light curves of 104 QSOs as a function of 0.1-2 keVflux

An estimate of the error on this quantity was obtained by simulation. Light curves were first constructed on the same binning structure as the real QSO. Errors were then introduced at each point by shifting the flux by a random amount according to a Gaussian distribution with standard deviation equal to the error on the real data. Measuring the variance in the resulting light curve and repeating 1000 times allows an estimate for the error in the intrinsic variance.

Finally, since the 7 *ROSAT* fields have different exposure windows spread over periods of 3–13 days the light curves were trimmed to be of approximately the same total length. This allows us to compare the variability of QSOs from different fields in a meaningful way since we are sampling the same timescales. A section of length $\sim 2\times10^5$ seconds was selected from each field, chosen to give the maximum on source exposure.

The results are displayed in Figure 3.3 where $\sigma^2_{intrinsic}$ is displayed as a function of flux for every QSO. In agreement with the analysis of detectable variability, many of the brighter QSOs with flux greater than 1×10^{-13}erg s^{-1}cm^{-2} show evidence for intrinsic variations significantly above zero. At fainter X-ray flux however the errors do not allow individual variable QSOs to be determined with confidence. Nevertheless, the fainter distribution show a mean amplitude of $\sigma^2 = 0.074 \pm .01$, equivalent to an average of 27% rms fluctuations. This is consistent with the mean of the brighter objects, suggesting that variations of this amplitude are 'typical' of the QSO population. Only one source displays an amplitude significantly higher than this mean value. This QSO, the brightest in the sample, will be examined in more detail in Section 3.7.

3.5 The evolution of QSO variability

Studies of bright, nearby active galaxies have suggested a possible relationship between the amplitude of variability and the luminosity of the source. Green et al (1993) studied high signal to noise observations of *EXOSAT* AGN and deduced that the amplitude of the power spectrum decreases with luminosity with the form $A \propto L_x^{-1/3}$. Similar results were obtained in an independent analysis by Lawrence & Papadakis (1993) who found $A \propto L_x^{-0.5}$. Green et al presented an explanation based on more luminous sources being physically larger in size. They suggest that the X-ray emission can be modelled as a number (N) of fragmented X-ray emitting regions which independently brighten and fade. Thus the probability of a large, coherent flare involving the whole disk would decrease for a larger source. One may therefore crudely relate the luminosity L to the number of fragments N and expect the amplitude of fractional variability to scale $A \propto \sqrt{N}/N$, leading to $A \propto L_x^{-0.5}$. If the emitting regions are not entirely independent then we expect larger changes than simple $\sqrt{N}$ variations and therefore a more gradual scaling with luminosity, eg. $A \propto L_x^{-\alpha}$ with $\alpha < 0.5$.

These observations were all conducted at low redshift. It is therefore important to establish whether such trends occur in the QSO population as a whole. In particular, QSOs were typically much brighter at high redshift. Using a subset of the sources studied here, Boyle et al (1993) found a prominent break in the QSO X-ray luminosity function. Tracing the redshift dependence of this feature showed that luminosity evolution of the form

$$L^* \propto (1+z)^{3.2 \pm 0.1} \qquad 0.3 < z < 2.2 \tag{3.11}$$

best describes the evolution of the QSO population. A similar form had already been established for the optical evolution of QSOs (Boyle et al 1987). Thus if the trend in variability amplitude is applicable to the QSO population as a whole we might expect smaller amplitude variability at high redshift. Assuming $A \propto L_x^{-0.5}$ we would predict $A \propto (1+z)^{-1.5}$ and thus the variability amplitude should be a factor of ~ 6 times lower at redshift $z = 2.2$ for a typical L^* QSO.

In Figure 3.4(a) the intrinsic variance in the 104 QSOs is plotted as a function of luminosity. The 21 brightest sources with flux greater than 1×10^{-13}erg s^{-1}cm^{-2} (0.1-2 keV) are emphasized in bold since these have the smallest errors. Despite the large scatter, there is no evidence for any trend in amplitude with luminosity, contrary to the results apparent in local AGN. This is also illustrated in Figure 3.4(b) where the mean values of σ^2 are shown in logarithmic bins. Over almost two orders of magnitude in luminosity there is no evidence for a change in the mean variability amplitude.

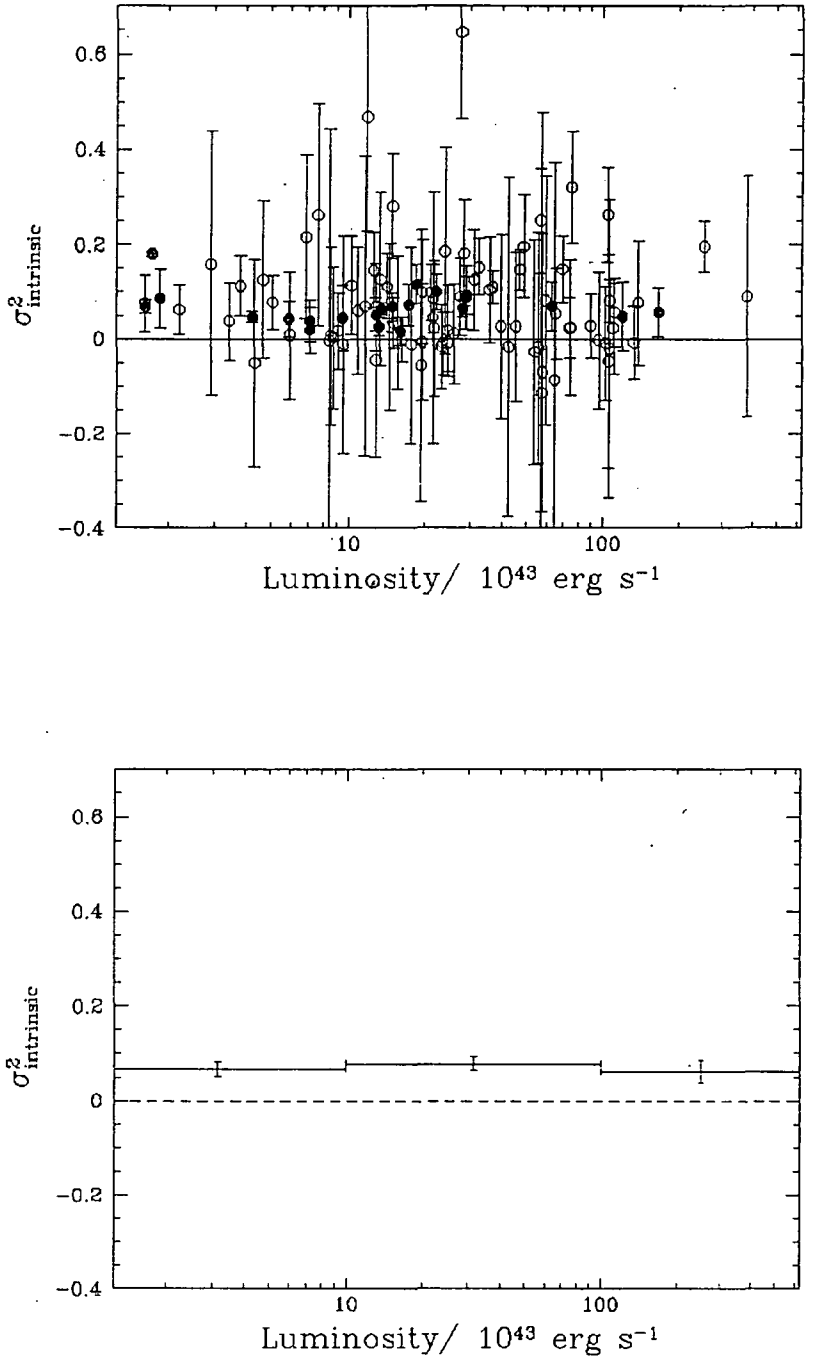

Figure 3.4: (a) Showing the intrinsic, noise subtracted variance in the light curves of 104 QSOs as a function of X-ray luminosity ($q_o = 0.5$, $H_o = 50$ km s^{-1} Mpc^{-1}). The 21 brightest QSOs are displayed in bold. (b) Showing the mean values of σ^2 in logarithmic luminosity bins.

Since QSOs evolve strongly with redshift, on Figure 3.5 the intrinsic variance is plotted as a function of L/L^*, where L^* is the characteristic break luminosity at the redshift of the QSO, according to the QSO X-ray luminosity function of Boyle et al (1994). The lack of any trend suggests that even QSOs which are characteristically luminous at a given epoch show no evidence for significantly smaller fluctuations.

In figure 3.6 the intrinsic variance for all QSOs is plotted as a function of redshift. There now appears to be very marginal evidence for a $\sim 40\%$ decrease in the mean amplitude at high redshift, but this is of no more than 1σ significance. Nevertheless, there is certainly no evidence for a factor of ~ 6 decrease by redshift $z = 2$, as predicted from an extrapolation of the local L_x/σ^2 relationship.

The results here appear to contradict the trend observed in local AGN, namely that more luminous AGN should show lower amplitude variability. This apparent discrepancy might be explained by reconsidering the physical implications of such a relationship. In particular, Green et al interpret the local relationship by suggesting that more luminous sources are physically larger in size. While this may be true of local AGN, applying this hypothesis to AGN at all redshifts would contradict the standard interpretations of QSO evolution.

As described above, QSOs are known to have evolved strongly with redshift. A typical L^* QSO at the break of the luminosity function is ~ 30 times more luminous by redshift $z \sim 2$. As outlined in Boyle et al (1987) there are at least two possible models:

- The evolution of successive generations of short lived (10^8yr) QSOs in which the mean intensity of QSO cycles diminishes. In this scenario most galaxies have been through a quasar epoch at least once.
- The evolution of individual, long lived QSOs which uniformly dim over time. In this scenario only $\sim 1\%$ of galaxies have ever undergone quasar activity, but would develop very massive black holes.

In the first model, we expect a typical QSO to harbour a black hole of mass $\sim 1 \times 10^8 h^{-2} M_\odot$ regardless of redshift. Black holes of this size allow the theoretically favoured accretion at Eddington limit (Rees 1984) for a QSO at peak activity. Thus the size of a typical emitting region is expected to be very similar at all redshifts and hence, using the crude arguments outlined above, we might expect similar fractional variability.

In the more controversial long lived model, QSOs have poured out a vast amount of energy over most of the age of the universe and should therefore develop extremely massive black holes. This can be calculated by integrating the total energy emitted by the QSO from redshift $z = 2$ to the present day. Assuming an accretion efficiency $\varepsilon = 0.1$

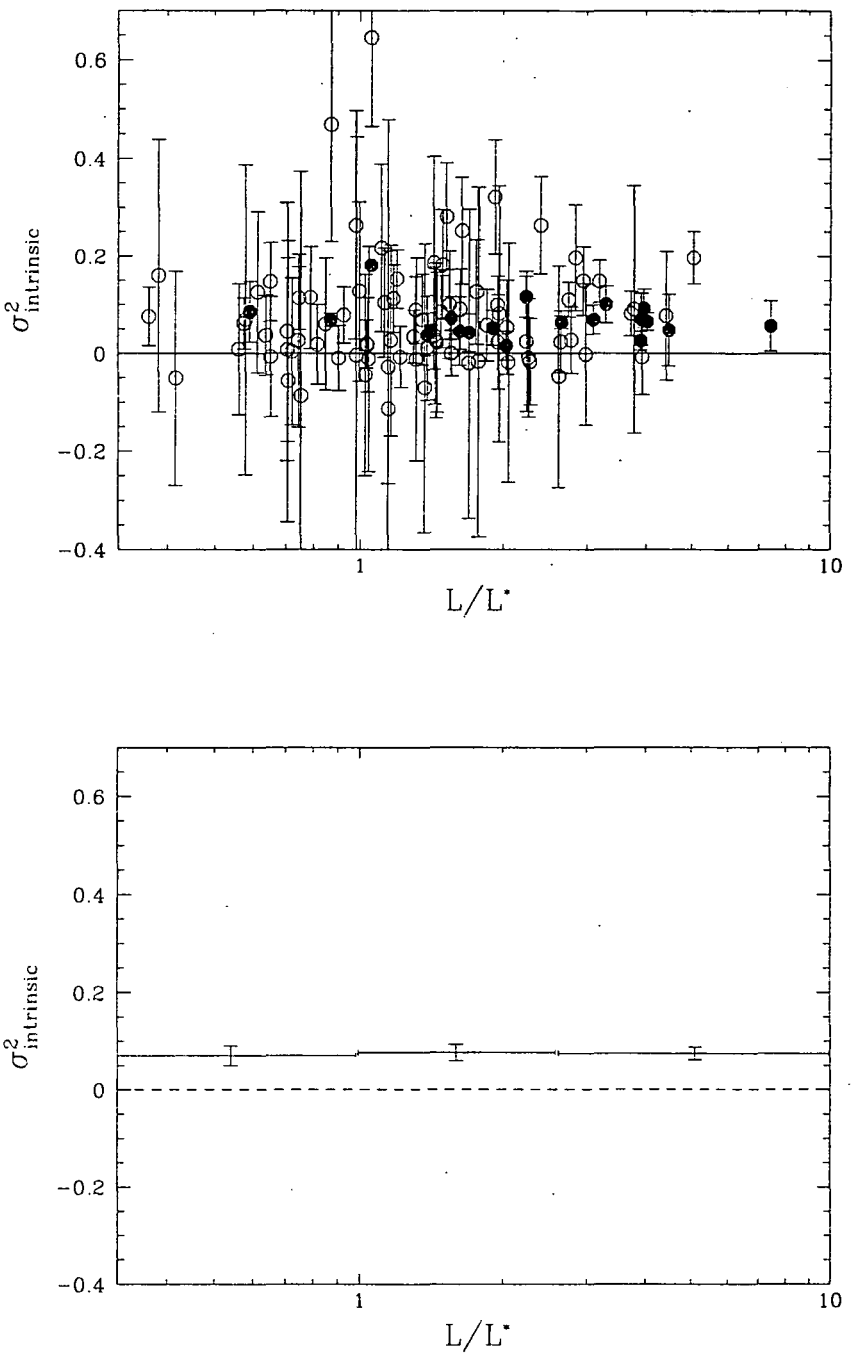

Figure 3.5: (a) Showing the intrinsic, noise subtracted variance in the light curves of 104 QSOs as a function of L/L^*, where L^* is the luminosity at the break of the luminosity function at the redshift of each QSO. The 21 brightest QSOs are displayed in bold. (b) Showing the mean intrinsic variance in logarithmic bins of L/L^*.

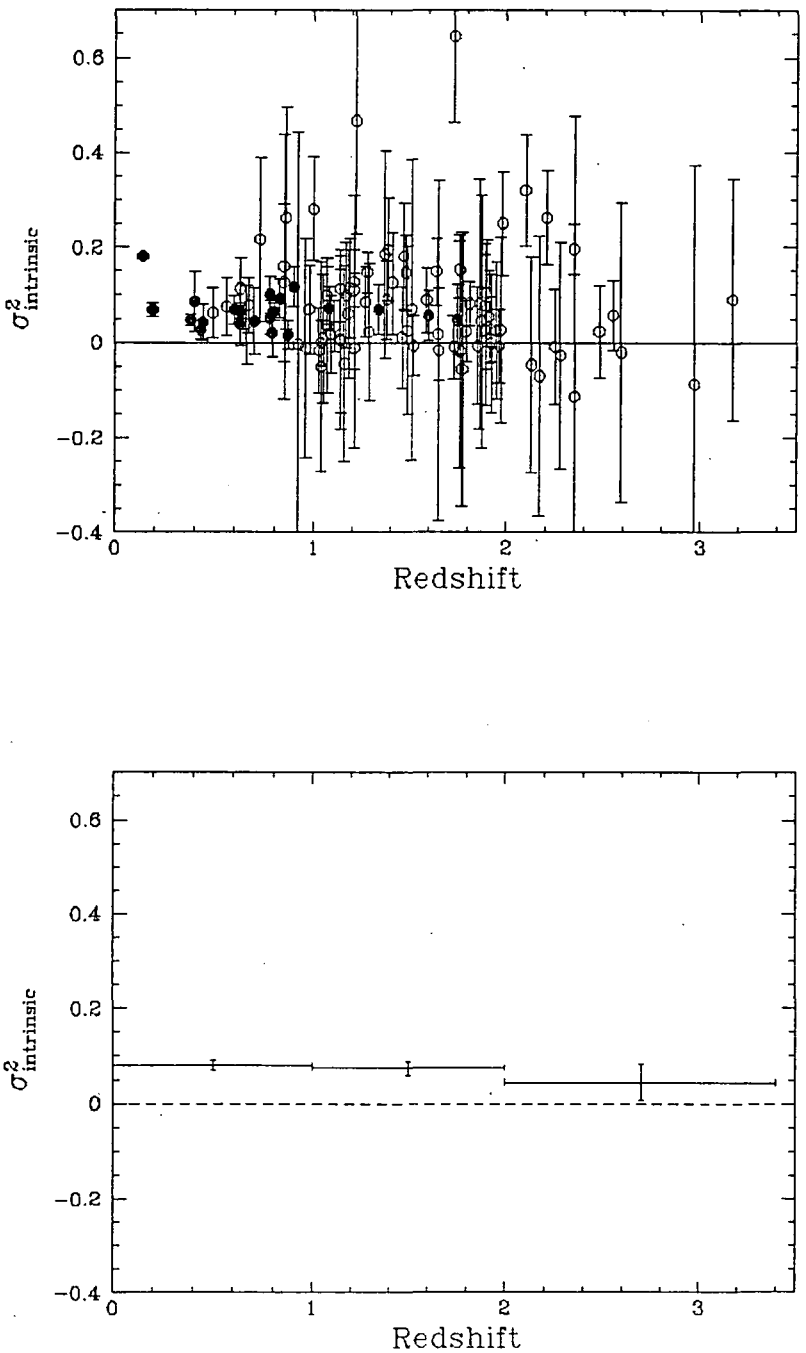

Figure 3.6: (a) Showing the intrinsic, noise subtracted variance in the light curves of 104 QSOs as a function of redshift. The 21 brightest QSOs are displayed in bold. (b) Showing the mean intrinsic variance in 3 redshift bins.

after Rees (1984) we obtain a black hole remnant of mass $\sim 1 \times 10^9 h^{-3} M_\odot$ for an L^* QSO at low redshift. Such enormous black holes are at least a factor of $\sim 10h^{-1}$ larger than the typical mass of a short lived QSO. It is therefore commonly assumed that this model can be ruled out by X-ray variability. However, although a few local AGN are certainly too variable to permit such massive black holes (eg. NGC4051, MCG-6-30-15), in general very large amplitude variations on short timescales are uncommon. Nevertheless, smaller masses have also been estimated using the velocities of line emitting clouds and their predicted distances from photoionisation arguments (Wandel & Mushotzky 1986, Padovani & Rafanelli 1988).

Thus to summarise, the two common interpretations of QSO evolution might crudely predict the following trends for variability amplitude with luminosity and redshift.

(i) In the short lived QSO model, there have been ~ 100 generations of QSOs from $z = 2$ to the present day, each lasting $\sim 10^8$ years. We therefore expect broadly similar black hole masses and size scales in L^* QSOs at all redshift and hence no trend with variability amplitude.

(ii) In the long lived QSO model, low redshift AGN are expected to have central engines an order of magnitude larger than their high redshift equivalents and hence the fractional variability ought to fall by a factor $10h^{-1}$ at low redshift.

In neither case do we expect the typical size scale to increase with redshift, as implied by an extrapolation of the local variability relationship. Thus the short lived QSO model, in which the mean size of the emitting regions is the same at all redshifts, is apparently favoured by our variability results. It should be noted that this is based entirely on the speculative premise that a larger source gives rise to smaller amplitude variability. A more complex coupling between variability amplitude and the luminosity of the source is entirely conceivable.

3.6 Biases in measuring variability amplitudes

The results presented here suggest no evolution in variability with redshift or luminosity. In comparing QSOs from different fields we have allowed for the differing exposure windows by trimming all light curves to be $\sim 2 \times 10^5$ seconds in length. Nevertheless, these results may still be biased by two other timescale effects:

Time dilation:

For a QSO at redshift z, a particular Fourier component in the light curve at frequency f will be observed at $f_{obs} = f/(1+z)$. For a "white noise" form of variability, the effect of redshift would be unimportant since the amplitude of variations will be the same at all frequencies. However, power spectrum analysis of local AGN suggests that the variability adopts a power law form $P(f) \propto f^{-1.5}$, ie. larger amplitude fluctuations at low frequencies. Thus if we assume a similar form for all QSOs, sampling higher frequencies in high redshift AGN may introduce a bias and artificially skew the distribution towards lower variability amplitudes. This could invalidate the comparison between QSOs of different redshift.

If we sample frequencies in a light curve in the range $f_{min} < f < f_{max}$ then the variance in the light curve will be given by (see Chatfield 1976):

$$\sigma^2 = \int_{f_{min}}^{f_{max}} P(f) df \tag{3.12}$$

If instead we observe the redshifted frequencies $f' = f/(1+z)$ then the difference in the expected amplitude (by integration of Equation 3.17), is a factor $(1+z)^{-0.5}$ for a power law of the form $P(f) \propto f^{-1.5}$. Thus the amplitude we have measured for QSOs of redshift $z \fallingdotseq 2$ should be increased by a factor ~ 1.7 for comparison with QSOs at zero redshift. This has no significant effect on the results presented here. Indeed, since there is marginal evidence for a decrease in amplitude by approximately the same factor, applying the correction only serves to strengthen the case for no evolution in variability.

Binning light curves:

Many of the fainter light curves are binned on longer timescales than bright QSOs to permit meaningful Poisson errors. This may have the effect of reducing the observable intrinsic variance by averaging out the high frequency variability. In principle this could bias the distribution of σ^2 with redshift or luminosity. However, this can be overcome by simply studying the bright and faint QSOs separately, thus ensuring that we sample the same range of frequencies. In fact there is no significant difference between

the resulting distributions and both show the same trends with luminosity and redshift. We conclude that any bias from rebinning is likely to be small.

3.7 Correlations with X-ray Spectra

There have been indications that local AGN with steep X-ray spectra show higher amplitude variability. Studying EXOSAT AGN, Green et al (1993) found a relationship between the amplitude of variability and the photon index of the form $A \propto \Gamma^{6.2\pm1.3}$, which was significant at $> 95\%$ confidence. This was interpreted in the context of reprocessing models for AGN. The presence of cold material in the central regions of active galaxies can reprocess the intrinsic power law emission by reflection and produce a 'reflection hump' near 10keV (Pounds et al 1990). This would harden the X-ray spectrum in the EXOSAT passband. Since rapid variability will be smoothed out during reprocessing, this could explain why harder sources in the Green et al sample show lower variability. However, since the contribution from reflected components is negligible in the *ROSAT* energy range, we do not expect this mechanism to be relevant in our analysis, even for high redshift QSOs.

There have been indications that the newly emerging population of narrow-line Seyfert 1 galaxies (NLS1) show particularly steep spectra ($\Gamma > 3$) and large amplitude variability (Brandt et al 1994, Boller et al 1995). Although we find no evidence for NLS1 among our sample, it would nevertheless be interesting to determine whether variability and steep energy spectra are related.

In Figure 3.7 the $0.5 - 2\,\mathrm{keV}$ intrinsic variability amplitude is plotted as a function of the spectral hardness (see Chapter 4) for all 104 QSOs. A minor correction was applied to the hardness ratios to take account of the differing levels of absorption by galactic hydrogen. For clarity, error bars are not shown although the 21 brightest QSOs with flux $> 1 \times 10^{-13}\mathrm{erg\,s^{-1}cm^{-2}}$ (and hence the smallest errors) are displayed in bold symbols. There is no significant trend with spectral index. Alternative definitions of the hardness ratios were also investigated (to probe the softest energies below 0.5 keV) and again there is no evidence for a trend. Thus it would appear that variability is not restricted to QSOs of a particular spectral shape.

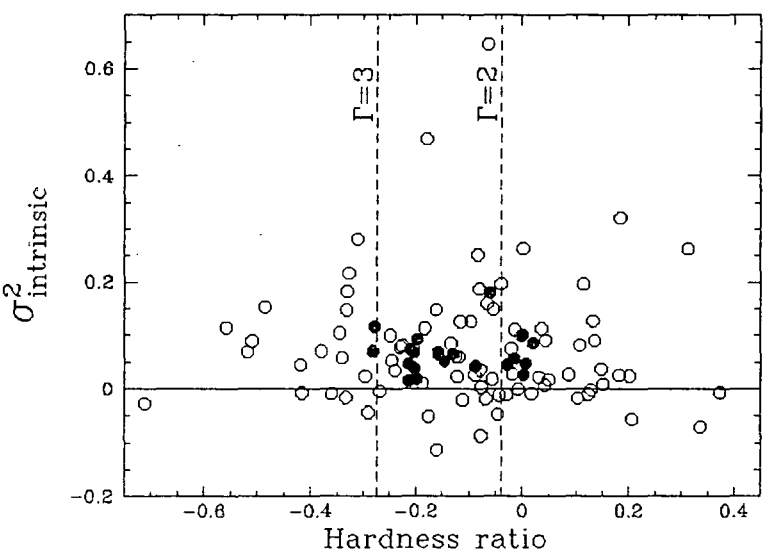

Figure 3.7: Showing the intrinsic variance as a function of the $0.5-2\,\mathrm{keV}$ hardness ratio. The 21 brightest QSOs displayed in bold. The equivalent hardness ratios for two power law models are also displayed for comparison.

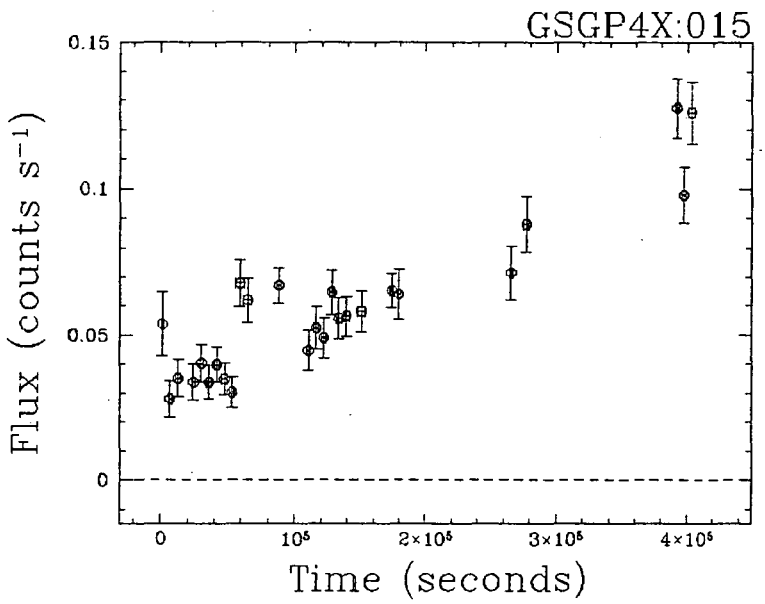

Figure 3.8: Light curve of the variable Seyfert galaxy, GSGP4X:015

3.8 A highly variable Seyfert galaxy

3.8.1 Constraining size scales

The light curve for GSGP4X:015 is displayed again in Figure 3.8. This object was optically identified as a Seyfert 1 galaxy at redshift $z = 0.15$. A χ^2 test yields a $> 99.99\%$ probability that the X-ray flux does not remain constant and as such this is the most significantly variable QSO in the sample.

The large amplitude of variability seen here is not typical of the QSO population. This can be seen in Figure 3.3 where GSGP4X:015 can be distinguished as the object with brightest flux, significantly more variable than any of the other 20 QSOs with flux $> 1 \times 10^{-13}$erg s^{-1}cm^{-2}. This remarkable object more than triples in luminosity steadily over the 4 day observation. There is also a significant flare after $\sim 6 \times 10^4$ seconds during which the luminosity doubles between successive orbits of the satellite, ie. on a time scale of less than 96 minutes. Such variability can provide tight constraints on the size scale of the emitting region and the mass of the central black hole. For a large enough change in flux we assume that most of the emitting region is involved. Such a change cannot occur more rapidly than the light crossing time of the source, thus $R_{em} < c\Delta t$. Models for accretion onto a supermassive black hole (Rees 1984) predict that the bulk of the X-ray emission occurs at ~ 5 Schwarzschild radii and thus $R_{em} = 5R_S = 10GM/c^2$. Hence we obtain an upper limit on the black hole mass:

$$M/M_{\odot} < 2 \times 10^4 \Delta t \tag{3.13}$$

The long term trend in the light curve gives a crude doubling timescale of $\sim 2 \times 10^5$ seconds, from which we obtain:

$$M < 4 \times 10^9 M_{\odot} \tag{3.14}$$

The shorter flare gives a much tighter constraint:

$$M < 1.2 \times 10^8 M_{\odot} \tag{3.15}$$

This second limit is very difficult to reconcile with a long lived model for QSO evolution, which would predict a remnant mass an order of magnitude larger. These arguments assume of course that the change in flux occurs over a large fraction of the emitting region. For large enough fluctuations this is probably valid. As noted by Mushotzky et al (1993) there is a good correlation between estimates of the central mass from X-ray doubling timescales and a completely independent dynamical method which uses velocities of optical lines and their inferred orbital radii from photoionisation arguments, allowing the mass to be obtained using $v = \sqrt{\frac{GM}{r}}$. Nevertheless, it is possible that the shorter flare is due to a localised event such as a powerful supernova. However, the implied luminosity change, $\Delta L \sim 10^{43} ergs^{-1}$, is 100 times brighter than the most luminous X-ray supernova ever detected (Fabian & Terlevich 1996).

3.8.2 Spectral changes

The AGN GSGP4X:015 displays significant evidence for a change in energy spectrum as the flux increases. This is illustrated in Figure 3.9 where a hardness ratio is plotted as a function of time. This particular hardness ratio was defined to emphasise the difference between the hard and soft part of the spectrum, with $HR = \frac{H-S}{H+S}$ where H and S give the total flux in the $0.1 - 0.5\,\mathrm{keV}$ and $1 - 2\,\mathrm{keV}$ bands respectively.

It is clear than this object becomes softer as the flux increases. Similar behaviour has been observed in a number of local Seyfert galaxies (Halpern 1985, Nandra et al 1991, Grandi et al 1992, Yaqoob et al 1993). The explanation for such variability is far from clear. In some cases the variability can be explained by relative changes in the normalisations of the power law and reprocessed spectral components (Nandra et al 1991). In others a steepening in the intrinsic power law continuum can explain the

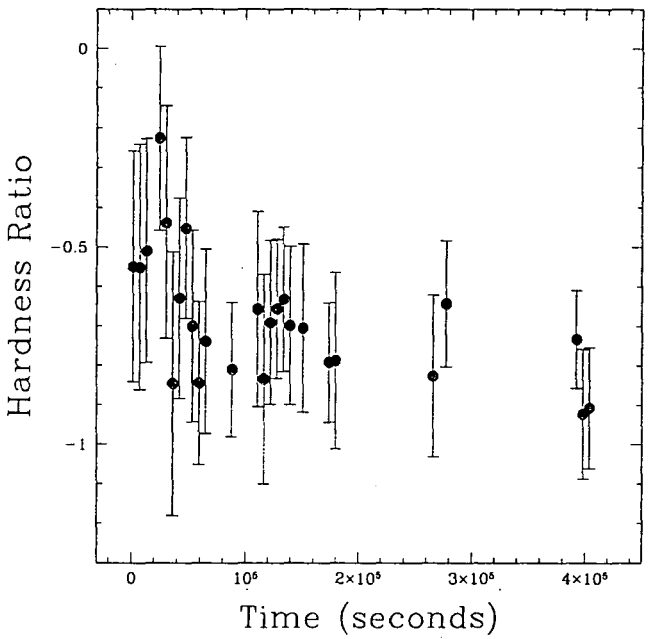

Figure 3.9: Showing the hardness ratio $HR = \frac{H-S}{H+S}$ as a function of time in GSGP4X:015 with a hard band H defined from $1 - 2\,\mathrm{keV}$ and a soft band S from $0.1 - 0.5\,\mathrm{keV}$

observations. There are also AGN where the variability can be explained by changes in the ionisation state of a so-called "warm absorber" (eg. Nandra et al 1990). Theoretically, as the luminosity of the central source increases the ionisation state of this material increases and reduces the opacity to low energy photons.

3.8.3 Spectral fitting

To investigate the emission processes occurring in this AGN, spectral fits were first performed on the total flux. A raw spectral file was obtained from a circular region enclosing 95% of the expected photons. Background subtraction was carried out using a nearby source free region, but amounts to a negligible fraction of the total counts. The resulting channel spectrum divides energies from $0.1 - 2.4\,\mathrm{keV}$ into 20 spectral bins. Spectral fitting was then carried out using the the XSPEC spectral fitting software. The results are summarised in Table 3.3.

The first trial model was a simple power law absorbed by the galactic column of neutral hydrogen (1.8×10^{20}atom cm^{-2}). This gave a very poor fit to the data ($\chi^2_{red} = 6.10$). The residuals suggested the need for an additional soft excess component below 0.7 keV and further photoelectric absorption at the softest energies below 0.2 keV.

Adding an intrinsic absorbing column improved the fit ($\chi^2_{red} = 4.3$) but emphasized the need for an additional soft emission component. Many local AGN show evidence for such a soft energy excess (Saxton et al 1993). This is commonly believed to be thermal black body emission from the accretion disk. An additional black body component was therefore added and this improved the fit substantially ($\chi^2_{red} = 1.23$). Thus the best fitting model consists of a steep intrinsic power law ($\Gamma = 2.97$), an absorbing column of $\sim 2 \times 10^{21}$ atom cm^{-2} and a black-body component with temperature kT$\sim$ 30 eV. The unfolded X-ray spectrum is displayed in Figure 3.10 with the best fitting model components.

A warm absorber model was also attempted, but in order to give an acceptable fit to the data a very deep, low energy edge was required ($\sim$ 0.5 keV) which is unphysical in terms of any photoionisation models (Reynolds, private communication).

In an attempt to explain the changing hardness ratios, two separate spectra were obtained from the high and low states of the light curve. The low state was defined from the first 9 time bins when the QSO is at lowest flux. The high state was defined from the period of maximum flux during the final 5 time bins in Figure 3.8. Spectral fitting was performed using the model which gave a best fit to the full data (model 3). The first notable finding is the lack of change in the intrinsic absorbing column as the source brightens. Since a change in N_H produces a very distinct feature in the spectrum we can immediately rule one explanation for the variability in which the change in flux is due to a variable absorber, such as a cloud moving across the line sight. Such a model is appealing as this would attenuate soft X-rays and harden the spectrum when the flux is low, as observed in GSGP4X:015. However, the absorbing column remains constant at a value of $\sim 2 \times 10^{21}$ atom cm^{-2}. The spectral changes must therefore be caused by the emission components. There are also no significant changes in the temperature of the black body or in the intrinsic slope of the power law spectrum. The only significant changes are in the normalisations of these two components.

This prompted another model in which the values of N_H, kT and Γ were fixed in order to better constrain the changes in normalisation (model 4). The results show that while the normalisation of the black-body changes by a factor of $\sim$ 2.7 between low and high states, the normalisation of the power law changes by only a factor $\sim$ 1.8, thus explaining the spectral change in a somewhat complex manner. In the popular reprocessing model (Pounds et al 1990) the excess soft X-rays are produced by the intrinsic power law source illuminating the accretion disk, which then thermalises and re-emits a black body spectrum. The fact that both emission components appear to brighten does suggests that they are linked in some way, but we expect the ratio of the two to remain constant with a negligible time lag. We certainly would not expect the soft excess to brighten by a larger factor than the intrinsic emission from which it is reprocessed. The steep spectrum of the power law also suggests that the hard energy

budget available for reprocessing is likely to be insufficient to explain the soft excess. It therefore seems likely that at least part of the soft X-ray excess arises from some intrinsic emitting process rather than reprocessing. Further evidence for such a component has been obtained with *ROSAT* observations of NGC5548 (Done et al 1995) where the soft excess brightens without a corresponding change in the hard power law.

Time range	Model	N_H	Black body		Power law		χ^2_{red}
			kT (eV)	Norm	Γ	Norm	
Full	1	–	–	–	2.13 ± 0.3	1.2×10^{-4}	6.10
Full	2	4 ± 1	–	–	2.78 ± 0.1	1.9×10^{-4}	4.30
Full	3	20 ± 3	30 ± 4	3.3×10^{-2}	2.97 ± 0.4	2.7×10^{-4}	1.23
Low state	3	20 ± 5	31 ± 6	2.4×10^{-2}	2.94 ± 0.3	2.2×10^{-4}	1.91
High state	3	20 ± 7	29 ± 4	7.2×10^{-2}	3.22 ± 0.3	4.4×10^{-4}	0.86
Low state	4	(20)	(30)	2.5×10^{-2}	(2.94)	2.3×10^{-4}	1.83
High state	4	(20)	(30)	6.7×10^{-2}	(2.94)	4.1×10^{-4}	0.83

Table 3.3: Spectral fits to the variable AGN GSGP4X:015. N_H is the intrinsic column density in excess of galactic absorption, measured in units 10^{20} atom cm^{-2}. In the first fits to the high and low states (model # 3), an absorbed power law + black body model is used with freely varying parameters. In the second fits to high and low states (model # 4) the intrinsic column, black body temperature and power law slope remain fixed at the values obtained from the best fit to the full data.

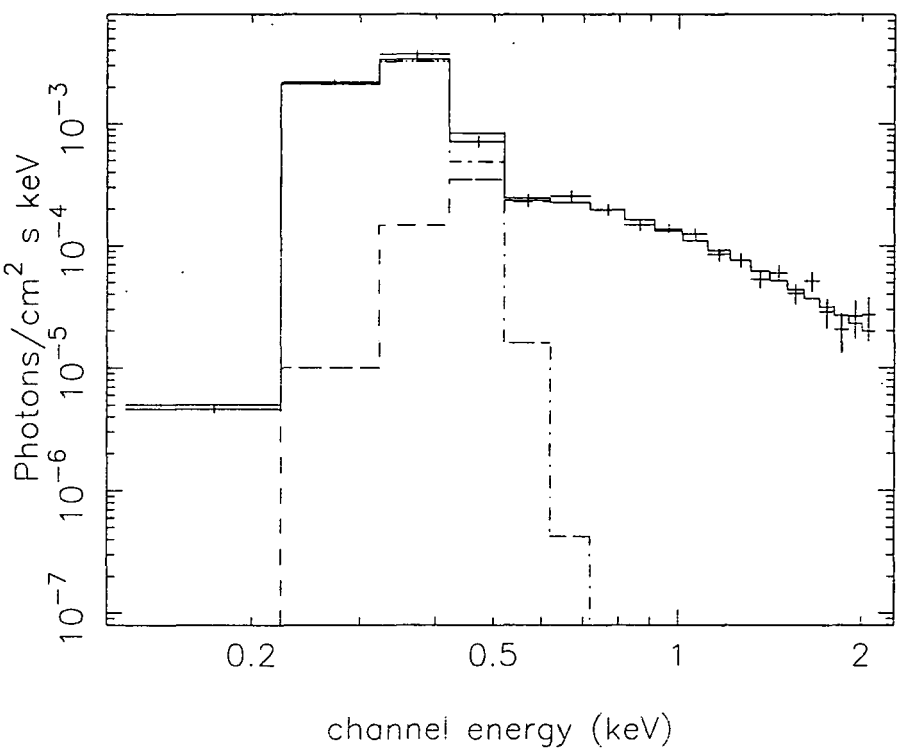

Figure 3.10: 0.1 – 2 keV unfolded X-ray spectrum of the variable QSO GSGP4X:015. The dashed line shows the contribution from the power law in the spectral model. The broken dashed line shows the thermal black body component. The sharp drop in flux below 0.2 keV is the signature of photoelectric absorption.

3.9 Summary and conclusions

The QSOs detected in our Deep *ROSAT* Survey have been used to study the variability characteristics of a flux limited sample of over 100 X-ray selected QSOs. Previous variability studies have concentrated on local, bright AGN.

A simple χ^2 test showed that 22 of the 104 testable QSOs show evidence for variability with $> 90\%$ significance. Of these, 12 are significant at $> 95\%$ of which 4 are significant at $> 99\%$ confidence level. Simulations were then carried out to reveal what amplitude of variability could have been detected in a given QSO. The results suggest that, given sufficient signal to noise, most QSOs would reveal evidence for low level variability. Of the 7 QSOs in which variability of 30% rms is detectable, 6 show significant variability.

In order to combine the results from QSOs with fluctuations just below the level of significant detection, a method is developed to estimate the amplitude of intrinsic fluctuations. In agreement with the analysis of detectable variability, the resulting distribution suggests that variability with rms fluctuations $< 40\%$ are a common feature of the QSO population. At brighter fluxes, most QSOs show evidence for variability significantly above zero. The mean amplitude of variability is equivalent to $\sim 27\%$ rms fluctuations.

There is no evidence for any evolution in variability amplitude with luminosity or redshift. This is in disagreement with a trend observed for local AGN (Green et al 1993, Lawrence and Papadakis 1993), in which more luminous AGN display lower amplitude variability. This may be explained if the typical size scale is the same for QSOs at all redshifts, as expected in a short lived model for AGN evolution.

Finally, the variability of a local $z = 0.15$ Seyfert galaxy is analysed in detail. This AGN, the brightest X-ray source in the sample, undergoes a factor of four increase in flux over the 4 day observation. A significant change by a factor of two occurs on a timescale of 6000 seconds, suggesting an upper limit of $M < 1.2 \times 10^8 M_\odot$ for the black hole mass. This AGN also exhibits spectral changes as the flux increases, becoming softer as it brightens. These changes cannot be explained in a straightforward manner. Detailed spectral fitting suggests that the changes are due to differential brightening between the soft excess and power law components in the spectrum. This would not be expected in standard reprocessing models, particularly given the steep spectrum of the power law component. Such behaviour suggests a separate component in the soft X-ray excess which is not reprocessed.

Chapter 4

The faint galaxy contribution to the X-ray background

In this chapter we investigate the contribution of faint galaxies to the X-ray background. By cross-correlating galaxy positions with unidentified *ROSAT* sources we overcome the problem of confusion to determine how many of these galaxies are truly X-ray luminous. We then probe deeper to determine the galaxy contribution to the remaining unresolved X-ray background.

4.1 Introduction

The X-ray background was the first cosmic background radiation to be discovered (Giacconi et al 1962) but despite over 30 years of study the origin and nature of this radiation is still a major unsolved problem. The most significant progress has been made in the soft X-ray band below 3keV since the launch of high resolution imaging satellites such as *Einstein* and more recently with *ROSAT*. By resolving as many sources as possible in the deepest exposures *ROSAT* exposures (Hasinger et al 1993) up to 70% of the $0.5-2\,\mathrm{keV}$ XRB can now been resolved into discrete sources.

Using a survey of 7 deep (21-49ks) *ROSAT* fields we have detected over 400 X-ray sources above a 4σ threshold to an approximate flux limit of $S(0.5-2.0\mathrm{keV}) \sim 4\times10^{-15}\mathrm{erg\,s^{-1}cm^{-2}}$. By optical spectroscopy we then attempt to identify the optical counterparts to these X-ray sources. The spectroscopic identification for 2 of these fields is described in Chapter 2. Using this technique it has been shown that broad-line QSOs directly account for at least 30% of the total $0.5-2\,\mathrm{keV}$ XRB flux (Shanks et al 1991). However, as a larger sample of QSOs became established, detailed studies of the QSO

X-ray luminosity function (Boyle et al 1994) and the source number count distribution (Georgantopoulos et al 1996) have shown that QSOs are unlikely to form more than 50% of the XRB at 1keV. The existence of a new X-ray emitting population was therefore postulated.

A further problem in explaining the XRB with QSOs is the shape of their X-ray spectra. The first studies found that the spectra of resolved sources, the majority of which were QSOs, were considerably steeper than the spectrum of the background itself (Turner & Pounds 1989, Fabian et al 1989). This implies that a new faint population with a very hard X-ray spectrum is required. Recent deep *ROSAT* studies are beginning to resolve such a population as they find evidence for hardening in the mean source spectra at faint fluxes (Hasinger et al 1993, Vikhlinin et al 1995, Almaini et al 1996). However, there have been suggestions that this hardening is not due to the emergence of a new population but rather a change in the properties of QSOs. Vikhlinin et al (1995) argue that the X-ray spectra of QSOs may harden at high redshift due either to an intrinsic change in the emission properties (Morisawa & Takahara 1990) or to intervening absorption from damped Ly-α systems. However, the results of Chapter 5 suggest that the X-ray spectra of QSOs *do not* change with flux or redshift and that the observed change in mean spectral properties is therefore due to the emergence of another unidentified population.

In recent years it has become clear that X-ray emission from galaxies can make a significant contribution to the XRB. Using *Einstein* observations of local galaxies, Giacconi et al (1987) extrapolated the observed X-ray to optical flux ratios to the faintest ($B < 27.5$) optical counts of Tyson et al (1988) and found that normal galaxies could produce at least 13% of the XRB at 2keV. Griffiths and Padovani (1990) used the observed evolution in the 60μm luminosity of IRAS galaxies and the local X-ray to infra-red ratios to estimate that IRAS and starburst galaxies seen to high redshift could produce 10-30% of the 0.5-3keV XRB. As pointed out by Ward et al (1993), the X-ray emission mechanism in these galaxies is unclear, but starburst activity and obscured AGN are possible explanations.

Other studies tested the galaxy contribution using the two-point cross-correlation W_{xg} between the hard (2-10 keV) XRB and various optical and infra-red galaxy catalogues (Lahav et al 1993, Miyaji et al 1994, Carrera et al 1995). These galaxy catalogues were generally fairly shallow ($z < 0.1$) but by correcting for the effects of clustering and extrapolating the measured volume emissivity to z$\sim$5 it was shown that 10-30% of the XRB could be explained by sources associated with galaxies. However because of the unknown error in such an extrapolation and the uncertain evolutionary properties of galaxies it is clearly desirable to probe more distant objects directly. The clearest evidence that fainter galaxies could be important contributors to the XRB came from the study of Roche et al (1995). Using the improved sensitivity and angular resolution of the

ROSAT satellite they were able to probe fainter limits and much smaller angular scales ($\sim 15''$). By cross-correlating faint galaxy catalogues with X-ray sources they obtained a $2-3\sigma$ detection implying that $B < 21$ galaxies account for $\sim 5\%$ of the X-ray sources. However they obtained a more significant ($\sim 5\sigma$) signal by removing the X-ray sources and cross-correlating with 3 deep (21-49ks) images of the *unresolved* XRB. The results implied that galaxies to a limit of $B = 23$ directly contribute $\simeq 17\%$ of the 1keV XRB. A simple extrapolation to $B < 28$ showed that galaxies could account for $\sim 30\%$ of the XRB or possibly more with evolution.

Although clearly an important result, a strong cross-correlation signal was only obtained for the deepest field analysed by Roche et al and so the statistical error remains uncertain. This field also contains extended X-ray emission from a galaxy cluster which may bias the results and no allowance was made in the interpretation for galaxies fainter than $B = 23$ which may themselves be X-ray luminous and clustered with the catalogued galaxies. In this chapter we intend to perform an independent and more rigorous test of these results on 3 deep (~50ks) *ROSAT* exposures, including the GSGP4 field analysed by Roche et al. First we will perform a cross-correlation of the unidentified X-ray sources with faint galaxies. We will then probe deeper into the unresolved XRB and attempt to deconvolve the effect of galaxy clustering using specific models of the galaxy population. For the new fields we have also used COSMOS scans of photographic plates in UBRI (Jones et al 1991) with which it may be possible to obtain information on the colour and type of galaxies responsible for the X-ray emission. If a significant signal is detected we will then consider the cross-correlation signal as a function of magnitude to obtain an estimate of the evolution of X-ray emissivity with redshift.

4.2 Cross-correlating X-ray sources with faint galaxies

4.2.1 Data and method

During the optical identification it was found that many X-ray sources appear to be associated with faint galaxies on photographic plates. Due to the high sky density of galaxies at faint magnitudes however (~10000 deg^{-2} at B<23, Metcalfe et al 1991) and the $\sim 15''$ radius X-ray error circle, many of these will be chance coincidences. If we look deep enough we can find a galaxy counterpart to any X-ray source. We will therefore adopt a statistical approach to determine the contribution made by galaxies to the X-ray source counts.

The 3 deepest *ROSAT* fields from the survey will be used in this analysis, including the GSGP4 field analysed by Roche et al (1995). Full details of the X-ray source detections and optical follow-up observations for the 2 deepest fields (BJS855

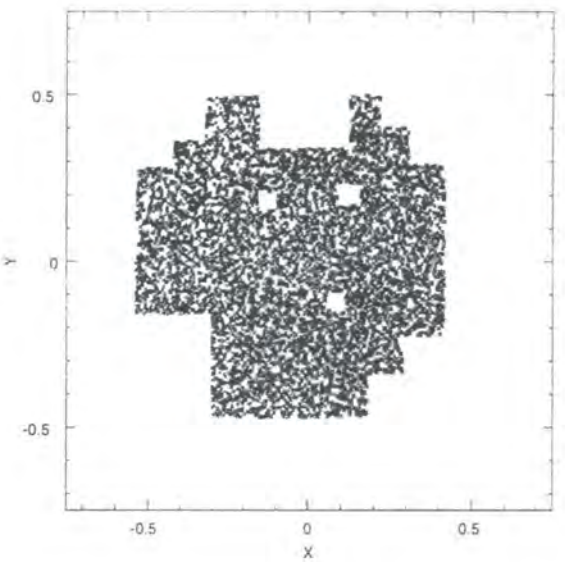

Figure 4.1: Showing the positions of 8714 galaxies with magnitudes $B < 23$ on the BJS855 field after transformation to X-ray coordinates (scaled to degrees).

and BJS864) are given in Chapter 2. The optical galaxy catalogues were obtained from COSMOS plate scans of Anglo-Australian Telescope photographic plates, calibrated with magnitudes and a star-galaxy separation flag. This optical data was previously used for the galaxy clustering and number count analyses of Stevenson et al (1985) and Jones et al (1991). B_j and R band photometry were available for the GSGP4 field and U, B, R, I photometry for the newer BJS855 and BJS864 fields. Further details of the plate reduction and zero point magnitude calibration are given in Jones et al (1991). Astrometric solutions to convert the plate co-ordinates into R.A. and Dec. were already in existence from the UVX QSO survey of Boyle (1990) and Boyle, Jones & Shanks (1991). As discussed in Chapter 2, a second transformation was then required to convert R.A. and Dec. into the (x,y) *ROSAT* pixel coordinates. This was performed using approximately 10-15 bright stars and UVX QSOs with definite counterparts on each *ROSAT* image. These gave 6 coefficient astrometric transforms with rms positional errors of between 7.1 and 8.4 arcseconds, as expected given the resolution of the *ROSAT* PSPC. On Figure 4.1 we show the resulting positions of $B < 23$ galaxies on one of the fields (BJS855) in X-ray coordinates. The plate edges and larger plate holes are clearly visible, where bad data has been flagged around bright objects or in some case where plate defects were detected in the plate measuring process (Jones et al 1991).

In calculating the cross-correlation of optical positions with X-ray sources the number of galaxies were counted in successive annuli of $5''$ width around each X-ray source. This distribution was then compared with the counts obtained by placing 50,000

random points over each of the field areas, taking care to avoid the plate edges and "holes". A two point cross-correlation function $C_{xo}(\theta)$ of X-ray and optical sources can then be defined as:

$$C_{xo}(\theta_i) = \frac{N_{xo}(\theta_i)N_r}{N_{xr}(\theta_i)N_o} - 1 \tag{4.1}$$

where, N_r is the total number of random points, N_o the number of optical plate sources being correlated and $N_{xo}(\theta_i)$ and $N_{xr}(\theta_i)$ give the number of X-ray/optical and X-ray/random pairs respectively.

4.2.2 Results

Removing only the X-ray sources identified with QSOs or galactic stars we cross-correlate the positions of the remaining 149 unidentified 4σ sources with the objects classified as galaxies on photographic plates. These optical galaxies were split into a bright sample with $B < 21$ and a fainter sample with $21 \leq B \leq 23$. The results are shown in Table 4.1, where we display the number of galaxies found within 20″ of an X-ray source compared to the distribution expected by chance. A 20″ radius was chosen as this approximately corresponds to the 2σ *ROSAT* PSPC positional error.

Considering first the cross correlation with brighter $B < 21$ galaxies, on each field we find an excess compared to a random distribution. Overall we find 33 source-galaxy pairs compared to 18.6 expected from a random distribution, amounting to a 3.3σ rejection of the null hypothesis that the two distributions are not correlated. This would indicate that $\simeq 14.4 \pm 5.7$ of these X-ray sources are due to $B < 21$ galaxies. On Figure 4.2(a) we display the source-galaxy cross-correlation in 10″ radial bins.

To probe deeper, we repeat the cross-correlation with the ~5000 fainter galaxies in the magnitude range $21 \leq B \leq 23$. We find 161 galaxies within 20″ of an X-ray source compared to 125.5 expected by chance. This represents a 3.2σ rejection of the hypothesis of no correlation and indicates that $\simeq 35.5 \pm 11.1$ of these X-ray sources are due to faint galaxies. The cross-correlation function is displayed in Figure 4.2(b) for the 3 fields combined.

Thus overall we appear to have significant evidence that $\simeq 50 \pm 13$ of the 149 unidentified X-ray sources are due to galaxies with $B < 23$, strengthening the initial findings of Roche et al (1995) who only found significant signal with brighter $B < 21$ galaxies. Thus from a total of 236 sources on 3 deep fields we have shown that faint ($B < 23$) galaxies contribute $\sim 21 \pm 6\%$ of the total source counts to an approximate limit of $S(0.5 - 2.0\text{keV}) \sim 4 \times 10^{-15}\text{erg s}^{-1}\text{cm}^{-2}$.

Magnitude range	Field	Pairs $< 20''$	Expected	Excess significance
$B < 21$	GSGP4	12	5.97	2.5σ
	BJS855	11	6.31	1.9σ
	BJS864	10	6.32	1.5σ
	Total	33	18.6	3.3σ
$21 \leq B \leq 23$	GSGP4	60	48.3	1.7σ
	BJS855	49	39.2	1.7σ
	BJS864	52	38.0	2.3σ
	Total	161	125.5	3.2σ

Table 4.1: Showing the number of faint galaxies found within $20''$ of unidentified X-ray sources on 3 deep fields compared to the number expected by chance. The galaxies are split into those with $B < 21$ and fainter galaxies with $21 \leq B \leq 23$.

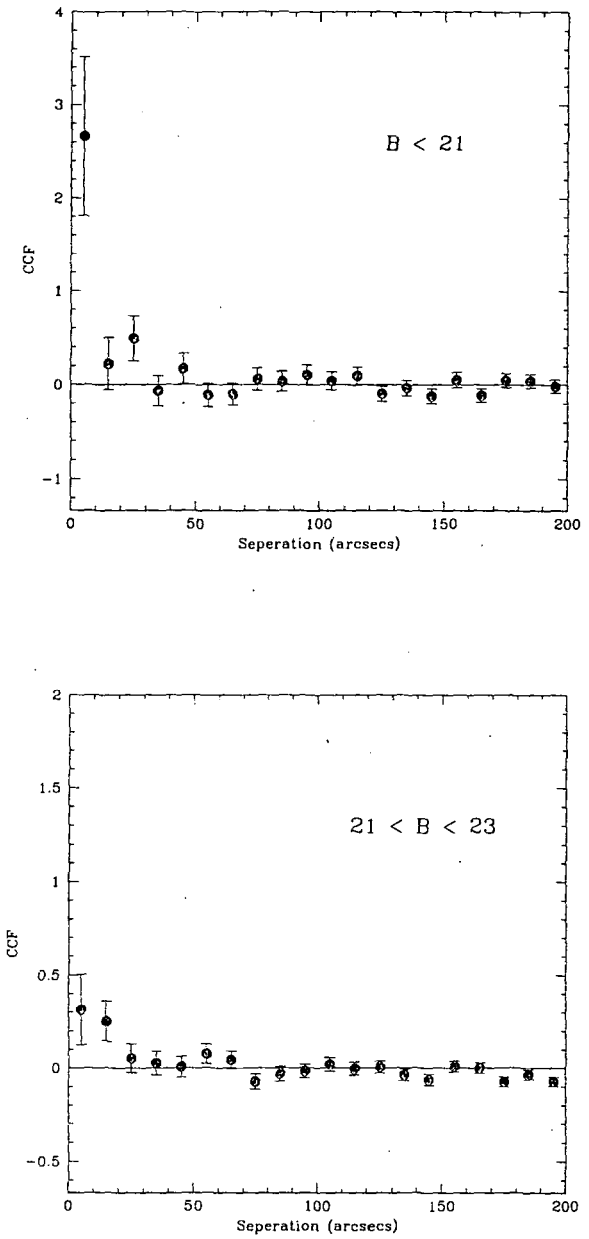

Figure 4.2: (a) The cross-correlation function $C_{xo}(\theta)$ of unidentified X-ray sources from 3 deep fields with $B < 21$ mag galaxies. On (b) we repeat the analysis with fainter $21 \leq B \leq 23$ mag galaxies. Note the change in scale compared to (a). Error bars are due to $\sqrt{N}$ statistics.

However when we scale this 21% galaxy contribution by the median flux of the unidentified X-ray sources ($\sim 7 \times 10^{-15}$erg s^{-1}cm^{-2}) we obtain a total contribution of $1.2 \pm 0.2 \times 10^{-9}$ erg s^{-1} cm $^{-2}$ sr^{-1} which accounts for only $\sim 4\%$ of the total XRB. We will therefore attempt to probe deeper in Section 4.3 by cross-correlating with the remaining unresolved XRB on deep *ROSAT* images.

4.2.3 Correlation with galaxy colour

To constrain the type of galaxy contributing to the cross-correlation signal we now consider galaxies separated by colour. When brighter ($B < 21$) galaxies were divided into blue and red subsets at $B - R = 1.5$ Roche et al (1995) found no significant difference in the cross-correlation with unidentified X-ray sources. We confirm this finding for the 3 deep fields analysed here. We find 22 blue galaxies within 20″ of an X-ray source compared to 10.9 expected from a random distribution and 11 red galaxies when we expect 6.6, each representing approximately a factor of $\sim$2 excess. The two cross-correlation results are displayed in Figure 4.3(a).

For fainter ($21 \leq B \leq 23$) galaxies however Roche et al found a total cross-correlation of only marginal significance and had insufficient statistics to provide a test with galaxy colour. With our more significant (3.2σ) cross-correlation using many more faint sources we may be able to test this for the first time. Splitting the fainter galaxies into blue and red subsets we find marginal evidence that *redder* galaxies give a stronger correlation, as displayed on Figure 4.3(b). Considering the pair counts within 20″ we find 61 red galaxies compared to 40.5 expected from a random distribution and 100 blue galaxies when we expect 88. Thus while both blue and red galaxies appear to contribute to the X-ray sources, a larger fraction of the red galaxies appear to be X-ray luminous ($33.7 \pm 13\%$ compared with $12.0 \pm 10\%$). If confirmed by the deeper analysis in the section 4.3 this result may provide an important clue in understanding the unusually high X-ray flux from these galaxies. It should be stressed however that the difference detected here, at only $\sim 2\sigma$, is of low statistical significance.

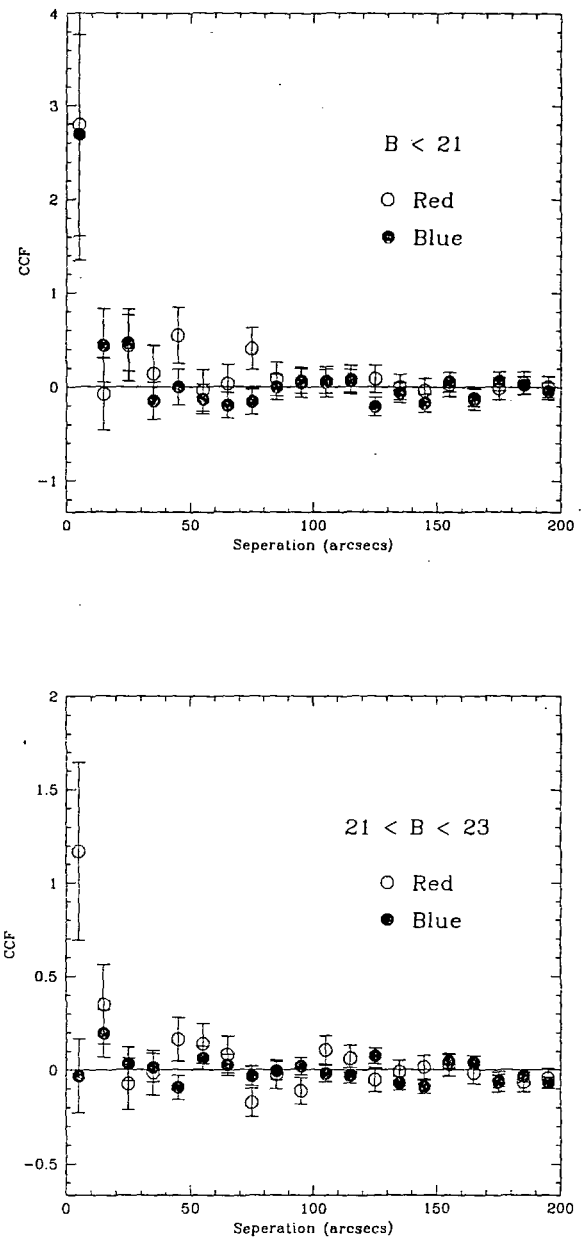

Figure 4.3: The cross-correlation function $C_{xo}(\theta)$ of unidentified X-ray sources from 3 deep fields with (a) $B < 21$ mag galaxies and (b) with fainter $21 \leq B \leq 23$ mag galaxies. In each case galaxies have been separated into blue and red subsets, dividing at $B - R = 1.5$. Note the change in scale from (a) to (b).

4.2.4 The properties of X-ray luminous galaxies

By adopting a statistical approach we have shown that $\sim 51 \pm 13$ of the 149 unidentified sources are due to faint galaxies. In most cases however it is impossible to unambiguously associate a galaxy with a particular X-ray source given the high surface density of faint galaxies. At brighter optical magnitudes the confusion problem becomes less pronounced. For the purposes of the spectral analysis of Chapter 4 and the luminosity function analysis (Griffiths et al 1996) we therefore selected a restricted sample of "probable" X-ray luminous galaxies chosen to have optical magnitudes $B < 21.5$ and to lie within $20''$ of a previously unidentified X-ray source. Only the objects firmly identified as galaxies by optical spectroscopy were included. In total 26 sources met this criteria on the 3 deepest fields, 20 of which were identified as emission-line galaxies and 6 showed only absorption line features. We will now estimate the fraction of these identifications which are spurious by cross-correlating these and the remaining unidentified X-ray sources with galaxies to the same magnitude limit. Many of these unidentified X-ray sources, particularly at brighter fluxes, had only stellar optical counterparts and may therefore have been classified as QSOs were it not for the unforeseen pointing problems of the Autofib instrument (see Chapter 2). As a correction for this we remove the unidentified X-ray sources brighter than $1 \times 10^{-14} ergs^{-1} cm^{-2}$ whose closest optical counterpart within $20''$ is a stellar UV excess ($U - B < 0$) object. Optical identification on the previous 5 fields suggests almost all of these sources are QSOs. Cross-correlation with the remaining sources suggests that $\sim 60\%$ of the source-galaxy associations are real. This in turn leads to an estimate that $\sim 40\%$ of the "probable" galaxy candidates are spurious. The true error estimate is likely to be lower than this however since most of the probable X-ray galaxies show emission lines while emission line galaxies account for fewer than half of all galaxies at these magnitudes (Tresse et al 1994). The fraction of false identifications could therefore be as low as $\sim 20\%$.

Previous analysis of the first five fields from this survey have revealed that unidentified X-ray sources show a steeper number count relation than AGN and may exceed their surface density at faint X-ray fluxes below 10^{-15}erg s^{-1}cm^{-2} (Georgantopoulos et al 1996). The cross-correlation results presented here suggest that $\sim 34 \pm 9\%$ of these unidentified sources are due to galaxies. A preliminary estimation of the luminosity function for these galaxies shows QSO-like luminosity evolution of the form $L_X \propto (1+z)^{3.35 \pm 1}$ (Griffiths et al 1996). The inclusion of the deeper data obtained in Chapter 2 will be described elsewhere (Griffiths et al in preparation) but serves only to strengthen the original findings. Similar conclusions are emerging from other surveys (Boyle et al 1995a, McHardy et al 1995). It therefore seems clear that faint galaxies are emerging as a significant new X-ray population. In the Section 4.3 we will probe deeper into the unresolved XRB to determine the total contribution from these galaxies.

As described in Griffiths et al (1995), a remarkable feature of these X-ray emitting galaxies are their extremely high X-ray luminosities, typically two orders of magnitude more luminous than galaxies observed locally (Fabbiano 1989) despite comparable optical luminosities. This has led to speculation on the possible emission mechanism. Obscured AGN (Comastri et al 1994), starburst activity (Treyer et al 1992) or advection dominated quasar remnants (Di Matteo & Fabian 1996) are among the possible alternatives. As outlined in Griffiths (1995) the optical colours and "D" parameters (measuring the strength of the break in the continuum below CaII H&K) suggest a range of Hubble types among these galaxies. Furthermore, using the equivalent width of the OII emission line as an indicator of starforming activity, the galaxies also appear to be a mixture of "active" (W[OII]> 10Å) and "passive" types and thus starburst phenomena alone cannot account for all of these objects. Without the spectral coverage to obtain redshifted Hα/[NII] or Hβ/[OIII] it is also difficult to distinguish starburst galaxies from Seyfert 2.

Two of these galaxies (GSGP4X:091 and GSGP4X:069) show significant evidence of photoelectric X-ray absorption of the order $N_H \sim 10^{21} - 10^{22}$ atom cm^{-2} (see Chapter 5), implying the presence of highly luminous X-ray sources buried within the galaxies. Obscured AGN would seem a likely explanation since the implied unobscured luminosities are $\sim 10^{44}$ erg s^{-1} (0.5 – 2.0 keV). Overall therefore these findings are consistent with the work of Boyle et al (1995a), who studied high signal to noise optical spectra of X-ray luminous galaxies at much brighter optical magnitudes. Using standard optical line ratios, the galaxies were classified as a mixture of starburst and Seyfert 2 galaxies, although in many cases the discrimination was ambiguous. Further work is clearly required to determine the true nature of these unusual galaxies. A number of observational tests will be discussed in Chapter 6.

4.3 Cross-correlating the unresolved X-ray background with faint galaxies

4.3.1 Aims

In this section we attempt to extend the cross-correlation technique to probe the remaining unresolved component of the cosmic X-ray background and thus investigate the origin of X-ray emission beyond the limit of significant source detection. By performing a similar analysis Roche et al (1995) found a positive signal and deduced that faint galaxies could contribute $\sim$ 30% of the total unresolved XRB at 1keV. However, this discovery was only significant for their deepest (GSGP4) field and requires verification. By performing an independent analysis on this and a further two deep fields we hope to confirm this important result. The effect of galaxy clustering and the contribution

from galaxies fainter than our optical magnitude limit will also be taken into account more rigorously. Using UBRI optical plate photometry it may also be possible to obtain information on the colours and type of galaxies contributing to the signal. Finally, by performing the analysis with different magnitude slices of the galaxy sample we may be able to deduce the redshift evolution of X-ray emissivity from faint galaxies.

4.3.2 The data

The X-ray images used in this analysis were obtained from deep ($\sim$ 50ks) *ROSAT* observations reduced using the STARLINK *Asterix* X-ray data reducing package. Since the X-ray background below 0.5 keV is dominated by galactic emission and solar scattered X-rays (Snowden & Freyberg 1993) the images used in the cross-correlation are extracted from only the 0.5 – 2 keV data. Data from periods of high particle background were also removed from the analysis, excluding approximately 10% of the photons when the Master Veto Rate was above 170 counts s^{-1} (Plucinsky et al 1993). As described in Chapter 2, additional data was available for the BJS855 and BJS864 fields from serendipitous pointings obtained using the *ROSAT* data archive, offset 6 and 7 arcminutes respectively from the original field centres. This data was processed separately before a mosaic of the final images was produced. The 4σ sources were then removed from the data using a range of exclusion radii suitable for excluding 98% of the photons, depending on the off-axis angle of the source. This radius varied from 30.6″ for a source on axis to 75.6″ for a source at a radius of 20 arcminutes. Inspection of the resulting images revealed that only one source showed evidence for being extended and could not be successfully removed in this way. This source, GSGP4X:032, was identified as a distant ($z = 0.54$) galaxy cluster and in fact the only cluster identified on these fields. A 70% larger radius was required to successfully remove this source. Finally, only the central 16 arcminute regions were used in the cross-correlation analysis since the sensitivity of the PSPC drops off rapidly beyond 20 arcminutes (Hasinger et al 1992). For the BJS855 and BJS864 fields, where deeper exposures have been obtained by adding additional archive data, only regions of the final image lying within 16 arcminutes of *both* field centers are used. An example image, binned on 5″ pixels, is displayed on Figure 4.4 before and after source extraction.

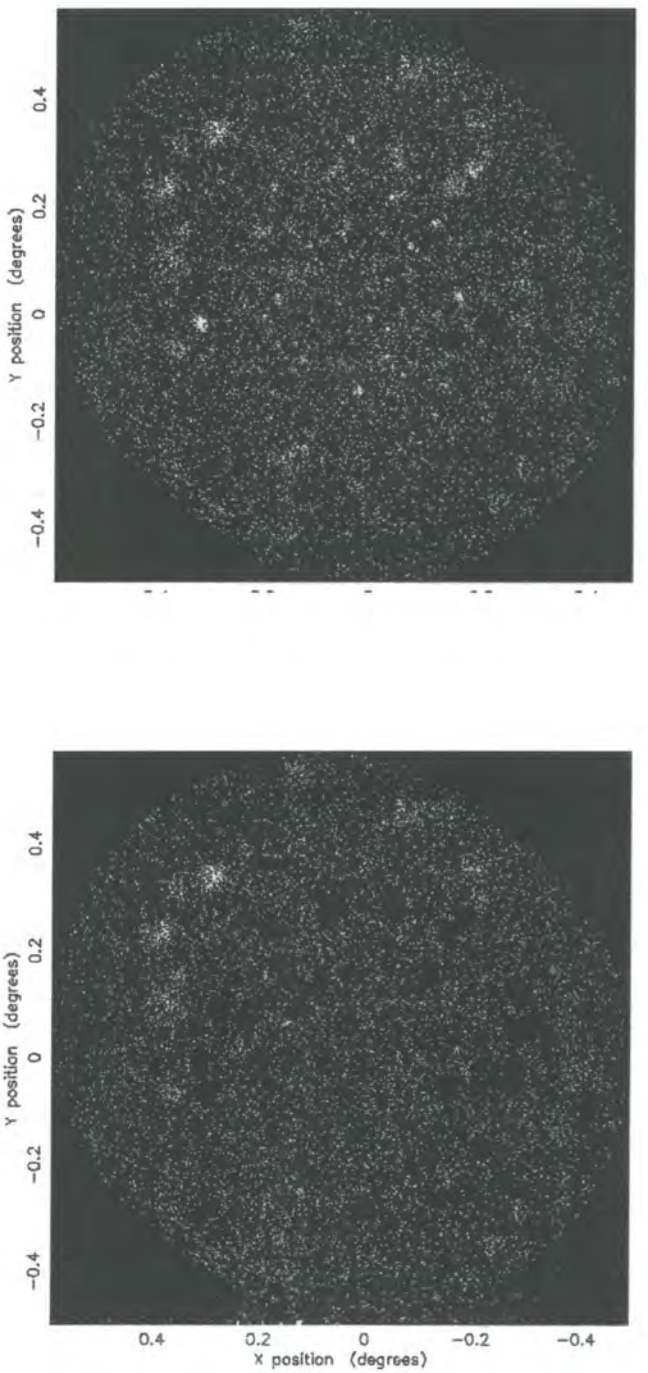

Figure 4.4: (a) Deep (52ks) *ROSAT* mosaic of the BJS864 field. On (b) we display the same field with the central 4σ sources removed. Note that the outer regions containing a few blurred sources are not used in the analysis.

4.3.3 Cross-correlation results

A two point cross-correlation between the unresolved X-ray images and the faint galaxy catalogues was obtained by counting the number of X-ray photons in successive annuli around each galaxy and comparing this with the mean pixel intensity. By repeating for every galaxy in the field (avoiding holed regions), the cross-correlation is defined by:

$$W_{xg}(\theta_i) = \frac{\sum N_x(\theta_i)}{\sum N_p(\theta_i)\,\langle N_X \rangle} - 1 \tag{4.2}$$

where $N_x(\theta_i)$ and $N_p(\theta_i)$ are the total number of X-ray photons and pixels respectively within annulus i of each galaxy, $\langle N_X \rangle$ is the mean number of photons per pixel and the summations occur over all the galaxies in the field. Error estimates were obtained by splitting each field into 4 quadrants and obtaining the cross-correlation for each separately. The error on W_{xg} was then estimated from the error on the mean from these quadrants.

The resulting two point cross-correlations between faint $18 < B < 23$ galaxies and the unresolved XRB are shown in Figure 4.5 in $15''$ bins. It is clear that a significant positive signal has been detected on each field. The errors on the first two bins alone ($< 30''$) suggest individual detections $> 3\sigma$ significance. The independent analysis of the GSGP4 field is seen to be in excellent agreement with the results of Roche et al (1995). Thus we find further strong evidence that faint galaxies are not only significant contributors to the resolved X-ray source counts but also to the fainter, as yet unresolved component of the X-ray background. In Table 4.2 we show the number of galaxy-photon pairs within $30''$ of the galaxies compared to the counts expected from a random distribution. The excess X-ray photons close to galaxies suggest $\gtrsim 3.5\sigma$ detections on each field assuming Poisson statistics. We have clearly confirmed the initial findings of Roche et al (1995).

In Figure 4.6 we show W_{xg} for the 3 deep fields combined, where we have summed galaxy-photon pairs across all fields and calculated the expected counts by combining the 3 separate $\sum N_p(\theta_i)\,\langle N_X \rangle$ terms. Errors have been estimated in the same manner as before by calculating 4 cross-correlations from the quadrants of each field and using the error on the mean values of W_{xg}.

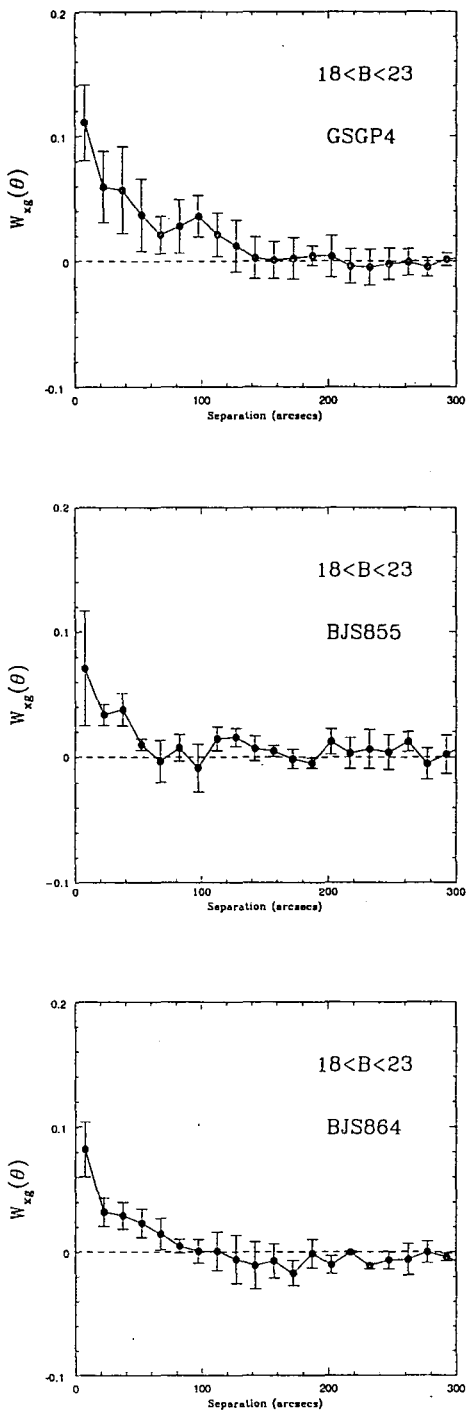

Figure 4.5: The cross-correlation function $W_{xg}(\theta)$ of the unresolved 0.5−2keV X-ray background with faint $18 \leq B \leq 23$ galaxies on 3 deep fields.

Field	Photons $< 30''$	Expected	Excess significance
GSGP4	8575	8154	4.5
BJS855	5763	5490	3.6
BJS864	7771	7414	3.8
Total	22079	21078	6.7

Table 4.2: Results of the cross-correlation of $18 \leq B \leq 23$ catalogue galaxies with the unresolved $0.5 - 2.0\,\mathrm{keV}$ X-ray background on 3 deep fields, comparing the number of $0.5 - 2.0\,\mathrm{keV}$ X-ray photons found within $30''$ with a random distribution.

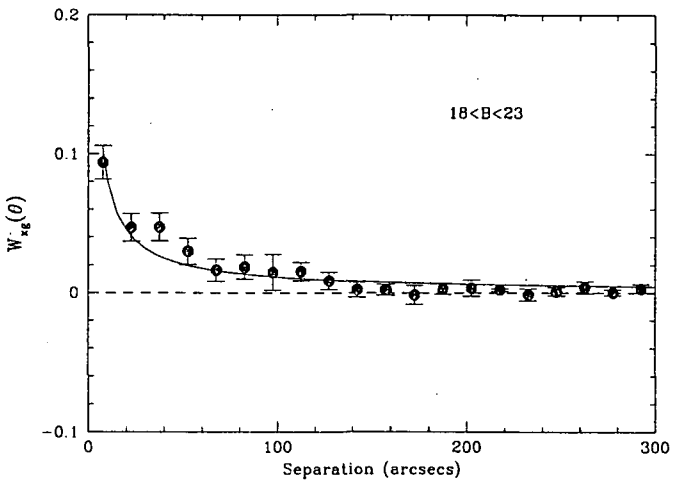

Figure 4.6: The total cross-correlation function $W_{xg}(\theta)$ of the unresolved $0.5 - 2.0\,\mathrm{keV}$ X-ray background on 3 deep *ROSAT* fields with $18 \leq B \leq 23$ galaxies. Also shown is the best fitting model of the form $W_{xg}(\theta) = A_{xg}\theta^{1-\gamma}$, where $\gamma = 1.8$ (see Section 4.3.5).

4.3.4 The effect of galaxy clustering

We have established a highly significant cross-correlation between the unresolved component of the cosmic XRB and faint galaxies. A naive interpretation of the excess photons would imply that $\sim 30\%$ of the XRB can be explained by $18 \leq B \leq 23$ galaxies. Galaxies do not randomly sample the sky however and are well known to show evidence of clustering and structure on the scales probed by our analysis. It is therefore probable that a non-negligible fraction of the enhanced signal in the cross-correlation is due to the clustering of galaxies with each other. In effect, the galaxies will correlate with the emission of their neighbours as well. One approach (see Roche et al 1995) is to apply an approximate correction using the *angular* clustering of the observed optical galaxies. However this will not account for the X-ray emission arising from fainter unseen objects ($B > 23$) which may be clustered with the galaxy catalogue.

To demonstrate this effect, following Treyer et al (1995), we consider the images split into cells each of small solid angle ω. The cross-correlation W_{xg} between galaxies

and the XRB can then be written in an alternative form:

$$W_{xg} = \frac{\langle (I-\bar{I})(N-\bar{N})\rangle}{\langle I\rangle\langle N\rangle} \tag{4.3}$$

$$= \frac{\langle NI\rangle}{\langle N\rangle\langle I\rangle} - 1 \tag{4.4}$$

where the averaging occurs over all cells of solid angle ω. Next we assume (after Peebles 1980) that each cell can be divided into volume elements δV_k containing either $n_k = 1$ or 0 galaxies. Therefore $N = \sum n_k$ and $I = \sum i_k$ where an intensity element i_k relates to the X-ray emissivity of the volume element by $i_k = (\rho_k / 4\pi r_k^2)\delta V_k$. Thus the terms in equation 4.4 can now be written:

$$NI = \sum n_k i_k + \sum_{j\neq k} n_j i_k \tag{4.5}$$

$$\langle NI\rangle = \int_{cell} \frac{\rho_g}{4\pi r_l^2} dV + \int_{cell}\int_{cell} n_1 \frac{\rho_2}{4\pi r_{l_2}^2}[1+\xi(r_{12})]dV_1 dV_2 \tag{4.6}$$

$$\langle N\rangle\langle I\rangle = \int_{cell} n_1 dV_1 \int_{cell} \frac{\rho_2}{4\pi r_{l_2}^2} dV_2 \tag{4.7}$$

where ρ_g is the X-ray emissivity arising from catalogued galaxies and ρ_2 is the emissivity arising from the sources clustered with those galaxies. The luminosity distances to these objects are given by r_l and r_{l_2} for a given cosmology. The function $\xi(r_{12})$ is the *spatial* cross-correlation function, giving the excess probability (above random) of finding an X-ray source at a physical distance r_{12} from a galaxy.

W_{xg} may now be written:

$$W_{xg} = \int \frac{\rho_g}{4\pi r_l^2 \langle I\rangle\langle N\rangle} dV + \int\int n_1 \frac{\rho_2}{4\pi r_{l_2}^2 \langle I\rangle\langle N\rangle} \xi(r_{12}) dV_1 dV_2 \tag{4.8}$$

$$= W_p + W_c \tag{4.9}$$

Therefore two terms contribute to the cross-correlation of faint galaxies with the X-ray background. The first is the contribution from the individual catalogued galaxies themselves, known as the *poisson* term. The second term (W_c) arises from the clustering of these galaxies with other background X-ray sources. It is therefore necessary to make specific assumptions about the X-ray emitting galaxy population before their true contribution to the X-ray background can be determined. This effect is discussed in detail in the work of Treyer et al (1995) where a prescription for modelling these populations is presented. We will now apply this formalism to our data.

4.3.5 Modelling the galaxy population

First we assume that any diffuse component of the $0.5-2.0\,\mathrm{keV}$ XRB is negligible in comparison with the source component and model the observed volume emissivity of the source population using an evolutionary parameter q such that:

$$\rho_{\mathrm{XRB}}(z) = \rho_s(z) = \rho_0(1+z)^q \tag{4.10}$$

Thus the intensity of the XRB per unit solid angle is given by:

$$\bar{I} = \frac{1}{\Delta\omega}\int_z \frac{\rho_s(z)}{4\pi r_l^2(z)}\mathrm{d}V \tag{4.11}$$

We will further assume that the spatial cross-correlation of galaxies with the X-ray sources $\xi(r,z)$ to be the same as the auto-correlation of faint galaxies with themselves. Arguably the most serious assumption, this effectively states that only galaxies are contributing to the observed cross-correlation signal.

Next we must characterise the properties of the galaxy population at a given redshift. Deep spectroscopic surveys (eg. Glazebrook et al 1995) have measured the galaxy $N(m,z)$ to optical magnitudes of $B \simeq 24$. We hope to model even deeper than this however. Fainter galaxies lack redshifts but Tyson et al (1988) and Metcalfe et al (1992) have obtained deep galaxy number counts $N(m) = \int_z N(m,z)\mathrm{d}z$ to a limit of $B \simeq 28$. Therefore as the best fit to the available data we will follow the method of Treyer at al (1995) and assume the distribution proposed by Efstathiou (1995) for the B_j band:

$$N(m,z) = N(m)\frac{3z^2}{2z_c^3(m)}\exp\left[-\left(\frac{z}{z_c(m)}\right)^{3/2}\right] \tag{4.12}$$

where:

$$z_c(m) = \begin{cases} 0.0113(m-17)^{1.5} + 0.0325 & \text{if } 17 < m \leq 22 \\ 0.0010(m-17)^3 + 0.0325 & \text{if } m > 22. \end{cases}$$

Integration of this relation to the faintest magnitudes at $B = 30$ gives the total expected *optical* volume emissivity at redshift z:

$$\rho_B(z) \simeq 3.8\times 10^{41}(1+z)^{1.3}\,h\,\mathrm{ergs^{-1}Mpc^{-3}} \tag{4.13}$$

Next we must model the clustering properties of the galaxy population and its evolution with redshift. We will adopt the standard form (Peebles 1980):

$$\xi(r,z) = (1+z)^{-(3+\epsilon)} \left(\frac{r}{r_o}\right)^{-\gamma} \tag{4.14}$$

where r is the spatial separation between the sources and ϵ models the clustering evolution. The clustering of local bright galaxies are well approximated by this power law form with $\gamma = 1.8$ and $r_0 = 5\ h^{-1}$Mpc. Faint blue galaxies however appear to be much less strongly clustered and we will assume best fitting parameters $r_0 = 2\ h^{-1}$Mpc and $\epsilon = -1.2$ as proposed by Efstathiou (1995).

Describing an X-ray emitting galaxy population in this way, Treyer et al (1995) have calculated the theoretical angular cross-correlation of galaxies with the X-ray background. The detailed calculations are somewhat cumbersome and will not be repeated here. However they find that W_{xg} obeys a simple power law of the form:

$$W_{xg}(\theta) = A_{xg}\theta^{1-\gamma} \tag{4.15}$$

where the amplitude is given by:

$$A_{xg} = \frac{\rho_o r_o^{\gamma} H_{\gamma} f(\aleph)}{4\pi \bar{I} \bar{N}} \tag{4.16}$$

In this expression $\bar{I}$ is the mean intensity of the unresolved XRB and $\bar{N}$ gives the number of catalogue galaxies per steradian. The function H_{γ} is given by:

$$H_{\gamma} = \int_{-\infty}^{+\infty} dx (1+x^2)^{-\gamma/2} \tag{4.17}$$

Assuming the standard $\gamma = 1.8$ we obtain $H(\gamma) = 3.68$. Defining a global evolution parameter $\aleph = \gamma - \epsilon + q - 5$, the function $f(\aleph)$ takes the form:

$$f(\aleph) = \int_z \mathrm{d}z (1+z)^{\aleph} r_c^{1-\gamma} \int_{B=18}^{B=23} N(m,z)\mathrm{dm}. \tag{4.18}$$

Thus we may re-arrange Equation 4.16 to obtain a value for the local X-ray volume emissivity ρ_o using our chosen description of the galaxy population and our observed X-ray parameters $\bar{I}$ and W_{xg}.

To obtain $\aleph$ we need a value for the parameter q which describes the evolution in the *observed* X-ray emissivity (Equation 4.10). For now we will make the assumption that the luminosity ratio L_X/L_{opt} remains constant at all redshifts and hence:

$$\rho_x(z) \propto \rho_B(z)(1+z)^{\alpha_B - \alpha_X} \tag{4.19}$$

In the B band we will assume a spectrum $\alpha_B \sim 1$ since the faint blue galaxy population is dominated by late type galaxies. In the X-ray band we will use an energy index of $\alpha_X \sim 0.6$, consistent with the spectra of the individually identified X-ray luminous galaxies (see Chapter 5). Inserting $\rho_B \propto (1+z)^{1.3}$ from the $N(z)$ fit of Efstathiou et al (Equation 4.13), leads to:

$$\rho_x(z) = \rho_o(1+z)^{1.7} \tag{4.20}$$

Thus by definition the parameter $q = 1.7$ and hence $\aleph = \gamma - \epsilon + q - 5 = -0.7$.

Finally we require the amplitude of the observed angular cross-correlation function $W_{xg}(\theta)$. Fitting the standard power law model of the form $W_{xg}(\theta) = A_{xg}\theta^{1-\gamma}$ to the combined cross-correlation (Figure 4.6) we obtain a best fitting index of $\gamma = 1.86 \pm 0.07$. Since this is consistent with the expected $\gamma = 1.8$ we fix the slope at this value and fit only for the amplitude. This yields (measuring θ in radians):

$$W_{xg}(\theta) = (1.55 \pm 0.13 \times 10^{-5}) \times \theta^{-0.8} \tag{4.21}$$

The mean intensity of the unresolved XRB from the 3 deep *ROSAT* fields used here is $\bar{I} = 1.59 \pm 0.2 \times 10^{-8}$ erg s^{-1} cm $^{-2}$ sr^{-1} and $\bar{N} = 2.64 \times 10^7$ galaxies sr^{-1} in the magnitude range $18 < B \leq 23$. Putting all of this together we may now obtain the local X-ray volume emissivity via equation 4.16 (using $q_o = 0.5$, $\Lambda = 0$):

$$\boxed{\rho_o \simeq 4.6 \pm 0.7 \times 10^{38} h \,\mathrm{ergs^{-1}Mpc^{-3}}}$$

However our sample is dominated by fainter, more distant galaxies with an expected median redshift of $\bar{z} = 0.27$ (by integration of Equation 4.12) for which:

$$\rho_x(\bar{z}) = \rho_o(1+\bar{z})^q \simeq 6.9 \pm 1.1 \times 10^{38} h \,\mathrm{ergs^{-1}Mpc^{-3}} \tag{4.22}$$

4.3.6 The contribution of faint galaxies to the unresolved XRB

The mean X-ray to optical luminosity ratio for the $18 < B < 23$ galaxies can now be estimated using:

$$\left\langle \frac{L_X}{L_B} \right\rangle = \frac{\rho_0}{\rho_B(0)} = 1.21 \pm 0.18 \times 10^{-3} \tag{4.23}$$

It is worth noting that this ratio is ~ 10 times higher than typical local galaxies (Fabbiano et al 1989), suggesting some evolution in the X-ray to optical ratios. We will discuss this further in Section 4.3.8.

This ratio may be used to calculate the total contribution of $18 < B < 23$ galaxies to the unresolved XRB. It is insufficient to simply scale $\frac{L_X}{L_B}$ by the total blue band flux as this would not allow for the differing optical and X-ray spectral indices of the galaxy population. We therefore multiply by the optical flux from each redshift slice separately using $N(m, z)$ from Equation 4.12 and apply the necessary k-corrections.

Thus the total X-ray emission per sr^{-1} due to $18 < B < 23$ galaxies can be estimated using:

$$\Delta \bar{I}_g = \left\langle \frac{L_X}{L_B} \right\rangle \times \int_z \mathrm{d}z (1+z)^{\alpha_B - \alpha_X} \int_{B=18}^{B=23} 10^{-0.4(m-\kappa)} N(m,z) \mathrm{d}m \tag{4.24}$$

$$= 3.3 \pm 0.5 \times 10^{-7} \mathrm{ergs}^{-1}\mathrm{cm}^{-2}\mathrm{sr}^{-1} \tag{4.25}$$

This accounts for 20±3% of the unresolved X-ray background, where the error is derived entirely from the uncertainty in the observed X-ray quantities, $W_{xg}(\theta)$ and $\bar{I}$. However it should be noted that this estimate also relies on very specific assumptions about the distribution and clustering properties of the galaxy population. In particular since $\rho_o \propto r_o^{-\gamma}$ (from equation 4.16), a more strongly clustered model with $r_o = 5h^{-1}$Mpc will reduce the contribution considerably to only $\sim 5\%$. However such strong clustering is difficult to reconcile with the low amplitude of the observed $\omega(\theta)$ for galaxies (Efstathiou et al 1995). Nevertheless, such models might still be permissable if we postulate the existence of a significant population of faint blue galaxies at high redshift. Such an extended distribution would dilute the observed $\omega(\theta)$ (Roche et al 1993) and allow a strong clustering model, but recent redshift surveys to $B = 24$ (Glazebrook et al 1995) favour a more local population of faint blue galaxies.

To determine the "total" galaxy contribution to the XRB we simply integrate Equation 4.24 to the faintest galaxies at $B \simeq 30$ and arbitrarily high redshifts. This process becomes increasingly uncertain as we extrapolate the redshift distribution be-

yond $B = 24$, but nevertheless using the estimate of $N(m, z)$ from Equation 4.12 and integrating to $z = 2$ we formally obtain $\sim 50\%$ of the unresolved $0.5 - 2.0\,\mathrm{keV}$ XRB, rising to $\sim 60\%$ when extended to $z = 4$. With additional evolution in the X-ray to optical luminosity ratios (see Section 4.3.8) it is possible to reach almost $\sim 100\%$ of the residual XRB flux, but given the uncertainties already inherent in this procedure it will probably suffice to say that galaxies can produce a significant fraction of the XRB at least as high as the contribution from QSOs.

4.3.7 Blue and red galaxies

To constrain the colour and type of galaxies producing the cross-correlation signal we use R band plates to separate the sample into blue and red subsets, dividing at $B - R = 1.5$. The cross-correlations were then carried out separately for each dataset. The results (Figure 4.7) show no significant difference in the cross-correlation amplitudes, suggesting that galaxies of all morphological types are contributing to the signal. This would appear to refute the tentative result obtained in section 4.2.2, where cross-correlation with X-ray sources gave a higher amplitude with red galaxies, although this result was only significant at $\sim 2\sigma$.

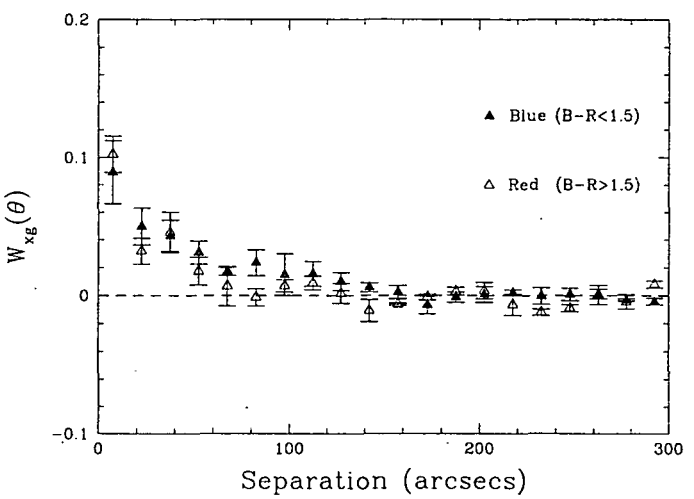

Figure 4.7: The cross-correlation function $W_{xg}(\theta)$ of galaxies with the unresolved $0.5 - 2.0\,\mathrm{keV}$ XRB, separating blue from red galaxies and combining the results from three *ROSAT* fields.

4.3.8 Constraining evolutionary parameters

In estimating the X-ray volume emissivity as a function of redshift and hence the total contribution to the X-ray background an implicit assumption has been that $L_X \propto L_{opt}$ at all redshifts.

To study this assumption further we now consider cross-correlating with successively fainter magnitude slices of the galaxy population. Modifying equations 4.16 and 4.18 we can obtain theoretical cross-correlations of the unresolved XRB with galaxies between the magnitude limits $[m1, m2]$:

$$\delta A_{xg} = \frac{\rho_0 r_0^{\gamma} H_{\gamma}}{4\pi \bar{I} \bar{N}_{\Delta m}} \int_z \mathrm{d}z (1+z)^{\aleph} r^{1-\gamma} \int_{m_1}^{m_2} N(m,z) \mathrm{dm} \tag{4.26}$$

We can normalize this by the observed cross-correlation from the full ($18 < B \leq 23$) galaxy sample, giving:

$$\delta A_{xg} = \frac{A_{xg}}{f(\aleph)} \int_z \mathrm{d}z (1+z)^{\aleph} r^{1-\gamma} \int_{m_1}^{m_2} N(m,z) \mathrm{dm} \tag{4.27}$$

Thus by performing the cross-correlation with different magnitude slices the resulting amplitudes may, in principle, allow us to constrain the evolutionary parameter $\aleph$ and hence the evolution in X-ray emissivity.

The galaxy catalogue was therefore split into "bright" ($18 < B \leq 21$) and "faint" ($21 \leq B \leq 23$) subsets and two separate cross-correlations carried out. The results are displayed in Figure 4.8. The brighter sample clearly give a higher cross-correlation amplitude. As before we fit power law models of the form $W_{xg}(\theta) = A_{xg}\theta^{1-\gamma}$ to the observed distributions, fixing γ at the value 1.8. With θ measured in radians these give amplitudes of $2.25 \pm 0.24 \times 10^{-5}$ for the bright galaxies and $1.38 \pm 0.16 \times 10^{-5}$ for the fainter sample..

To compare with a range of theoretical predictions we evaluate the integral in equation 4.27 to obtain expected values for these amplitudes as a function of the evolutionary parameter $\aleph$. These are displayed in Figure 4.9 for both magnitude slices. For comparison the shaded area shows the 1σ confidence region on the *observed* amplitude for the brighter galaxies and the corresponding preferred values of $\aleph$. For the fainter sample however the weaker dependence of A_{xg} on $\aleph$ does not allow us to provide any useful constraints on the evolutionary parameter. This is expected however since, by construction, Equation 4.27 is normalized by the amplitude of the full $18 < B \leq 23$ dataset and therefore dominated by these fainter galaxies.

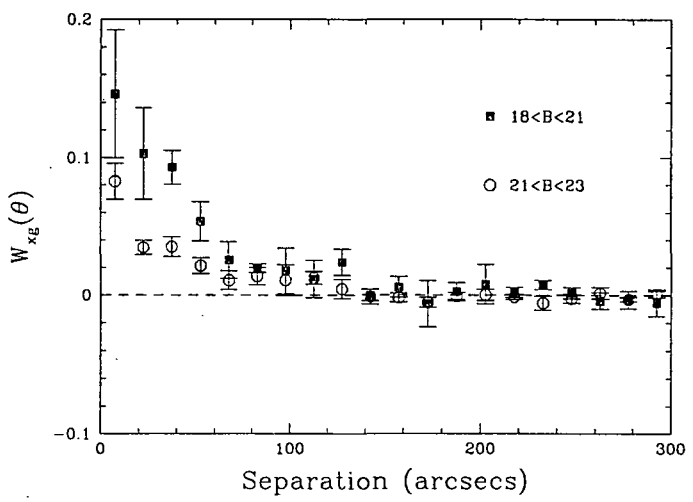

Figure 4.8: The cross-correlation function $W_{xg}(\theta)$ of galaxies with the unresolved $0.5-2.0\,\mathrm{keV}$ XRB from three *ROSAT* fields. The galaxies are split into a bright and faint sample.

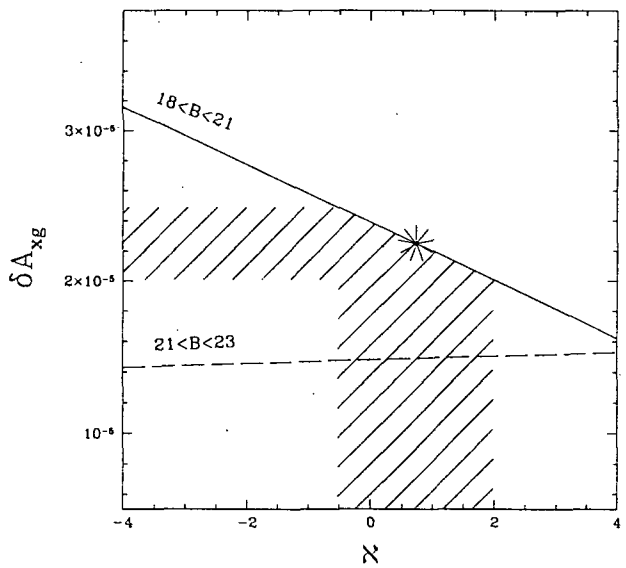

Figure 4.9: Showing the expected relationship between the amplitude of the cross-correlation function W_{xg} and the evolutionary parameter $\aleph$ for brighter $18 < B \leq 21$ galaxies (solid upper line) and the fainter $21 \leq B \leq 23$ galaxies (lower dashed line). The shaded region displays the 1σ error bounds on the *measured* amplitude for the brighter galaxies and the corresponding range of $\aleph$.

The errors on δA_{xg} suggest values of $\aleph$ in the range $-0.52 < \aleph < 1.98$. This global parameter was defined $\aleph = \gamma - \epsilon + q - 5$ where q describes the evolution of the X-ray emissivity as a function of redshift (Equation 4.10) and γ and ϵ characterise the clustering properties of the galaxy population (see Equation 4.14). We will therefore assume that the latter two quantities are relatively well defined in comparison with the parameter q and adopt the values $\gamma = 1.8$ and $\epsilon = -1.2$ from Efstathiou et al (1995). This leads to values of $q = 2.73 \pm 1.25$ and thus a best estimate for the evolution of the X-ray emissivity due to galaxies:

$$\rho_x(z) = \rho_o(1+z)^{2.73\pm1.25} \tag{4.28}$$

This is in broad agreement with our previously assumed value of $q = 1.7$, obtained on the assumption that $L_X \propto L_{opt}$, with a tentative suggestion of some additional evolution in L_X. Using a spectral index of $\alpha_x \sim 0.6$ we can obtain our best estimate for the X-ray luminosity evolution of faint galaxies:

$$L_x \propto (1+z)^{3.33\pm1.25} \tag{4.29}$$

which is very similar to the X-ray evolution of AGN. Similar forms have been obtained by considering the luminosity function of individually identified X-ray luminous galaxies at much brighter fluxes (Griffiths et al 1996, Boyle et al 1995a) which follow $L_x \propto (1+z)^{2.3}$.

If the X-ray to optical luminosity ratios evolve in the manner suggested here this will increase the galaxy contribution to the XRB (Equation 4.12). As before, if we integrate Equation 4.12 to $B = 30$ and redshift $z = 2$ our estimate of the total galaxy contribution rises from 50% to $\sim 70\%$ ($q_o = 0.5$, $\Lambda = 0$).

4.4 Summary and conclusions

By cross-correlating faint galaxy catalogues with unidentified X-ray sources a strong (4.2σ) signal was detected indicating that individual galaxies with magnitude $B < 23$ account for $21 \pm 6\%$ of all X-ray sources to a limiting flux of $\sim 4 \times 10^{-15}\mathrm{erg\,s^{-1}cm^{-2}}$ in the $0.5 - 2.0\,\mathrm{keV}$ band. This builds on the results of Roche et al (1995) who found a significant signal in cross-correlation with brighter $B < 21$ galaxies, attributing $\sim 6\%$ of the X-ray sources to these brighter objects. Scaling the 21% galaxy fraction by the median flux of the unidentified X-ray sources leads to $\sim 3-4\%$ of the total XRB intensity.

To probe deeper we cross-correlate with individual photons in the remaining unresolved XRB images. Significant signals were obtained on all 3 deep *ROSAT* images, each of similar amplitude, independently confirming the results obtained by Roche et al (1995). When the optical galaxy catalogue is separated into blue and red subsets, dividing at $B - R = 1.5$, there was no significant difference in the cross-correlations. This would suggest that a mixture of galaxy colours and morphologies contribute to the observed signal.

To translate these cross-correlations into a total fraction of the unresolved XRB a specific description of the galaxy population is adopted, modelling the evolution, number density and clustering properties of the faint blue galaxy population using the formalism developed by Treyer & Lahav (1995). By comparing the theoretical XRB cross-correlation with the observed signal an estimate for the local X-ray volume emissivity was obtained at $\rho_o \simeq 4.6 \pm 0.7 \times 10^{38} h\,\mathrm{ergs^{-1}Mpc^{-3}}$ ($q_o = 0.5$, $\Lambda = 0$). Scaling the implied X-ray to optical luminosity ratio by the integrated blue band flux leads to an estimate that $B < 23$ galaxies account for $\sim 20\%$ of the unresolved XRB. Extrapolation to fainter limits ($B = 30$) and high redshift ($z = 2$) suggests that this fraction increases to $\sim 50\%$. These estimates have a strong dependence on the assumed clustering properties of the galaxy population ($\delta I_{xrb} \propto r_o^{-1.8}$) and could be reduced by a factor of four if faint galaxies cluster with the scale length observed for local bright galaxies, $r_o = 5h^{-1}\mathrm{Mpc}$.

However recent results (see Efstathiou et al 1995) favour weaker clustering at faint blue magnitudes which would support a more significant contribution of galaxies to the XRB.

To constrain the evolution of X-ray emissivity with redshift, separate cross-correlations were carried out with two magnitude slices of the galaxy population. The resulting difference in amplitude suggests that faint galaxies evolve strongly with redshift such that:

$$L_x \propto (1+z)^{3.33\pm1.25} \tag{4.30}$$

which represents the first evidence that the X-ray emission from faint blue galaxies evolves as strongly as AGN. Similar results have been obtained by analysing the brightest narrow emission line galaxies emerging from deep *ROSAT* exposures (Griffiths et al 1996, Boyle et al 1995a) . Such evolution leads to a revised estimate that galaxies contribute in the range 50 – 100% of the unresolved XRB.

Having established the existence of a population of highly luminous X-ray galaxies, the next intriguing question is the origin and nature of this activity. Boyle et al (1995b) have obtained high resolution optical spectroscopy for a selection of individual X-ray galaxies at much brighter magnitudes which suggests a mixture of starburst and Seyfert 2 activity. In many cases however the classification was ambiguous. Type 2 AGN provide a natural explanation since the expected X-ray absorption can readily reproduce the flat spectra of the XRB (Comastri et al 1995, Madau et al 1994). At least two of the brighter X-ray galaxies identified in Chapter 5 show clear evidence of X-ray obscuration. The discovery of a high redshift counterpart to this population adds further credence to this possibility (see Chapter 2).

Starburst activity is another possible explanation. There have been suggestions that massive X-ray binaries formed in the wake of star formation in early, low metallicity epochs may provide a strong source of hard X-ray emission (Griffiths and Padovani 1990), as described in Chapter 1.

Infra-red spectroscopy may provide a means to test between these competing theories. Seeing through the obscuring dust to detect, for instance, a broad Paschen α line would conclusively prove the existence of a hidden AGN. However it seems likely that both of the above mechanisms contribute to the XRB to some extent. Some additional hot thermal emission from galaxies in clusters or groups is also expected, but this certainly cannot explain the harder XRB above $\sim 10\,\mathrm{keV}$. A third explanation has emerged recently which describes low luminosity AGN residing in seemingly normal galaxies as the end products of quasar evolution (Di Matteo & Fabian 1996). In this scenario it is predicted that most galaxies might harbour a massive black hole as the remnant of

an earlier, more active quasar epoch. The resulting low accretion efficiency will form a hot bloated ion torus (Rees 1984) which may give rise to advection dominated accretion. This leads to a two temperature gas in which the ions are much hotter than the electrons. The electron temperature saturates at $\sim 100\,\mathrm{keV}$ and gives rise to Bremsstrahlung radiation. A superposition of many such sources over a range of redshifts can then provide a good fit to the XRB.

Further observations are required to distinguish between these competing explanations. This will be discussed further in Chapter 6.

Chapter 5

The X-ray Spectra Of Faint ROSAT sources

In this chapter we present an X-ray spectral analysis of the sources detected in our deep *ROSAT* survey. A long standing problem in X-ray astronomy has been the identification of a source population with a spectrum as flat as the residual background. Here we investigate this problem and compare the spectral properties of the different source types.

5.1 Introduction

The launch of the *ROSAT* X-ray satellite has allowed us to detect X-ray sources at least an order of magnitude fainter than ever before. We have undertaken a major observational programme to understand the nature of the faint X-ray sources from deep ($21 - 49$ ks) *ROSAT* PSPC exposures. The aim of this survey is to identify sources at the faintest possible flux limits in an attempt to understand the nature and origin of the cosmic X-ray background (XRB). Details of the optical spectroscopic identification for 2 of the deepest fields are described in Chapter 2. So far we have identified over 150 QSOs from 7 *ROSAT* fields and shown that QSOs make up at least $\sim 30\%$ of the XRB at 1keV (Shanks et al 1991). However, studies of the QSO X-ray luminosity function (Boyle et al 1994) and the number count distribution (Georgantopoulos et al 1996) suggest that the known QSO population is unlikely to form more than 50% of the total XRB flux. QSOs also show relatively steep X-ray spectra with indices of $\Gamma = 2.2 \pm 0.1$ while the extragalactic XRB from 1-10 keV has a flatter power-law index of $\Gamma = 1.4$ (Gendreau et al 1995). This suggests that we need a new faint source population with a flatter X-ray spectrum to account for the remainder of the background radiation.

From these deep *ROSAT* exposures it is also beginning to emerge that many of the remaining faint X-ray sources correspond to galaxies with $B < 21$, which appear to be a mixture of absorption and emission line galaxies with optical spectra and redshifts typical of the galaxy population. However the implied X-ray luminosities are $10 - 100$ times higher than those of similar galaxies locally (Roche at al 1995a, Griffiths et al 1995, McHardy et al 1995). The nature of the X-ray emission mechanism in these galaxies is still not clear, but recent work at brighter flux limits (Boyle et al 1995b) suggests that some may be Seyfert 2 or starburst galaxies. The clearest evidence that faint galaxies are significant contributors to the XRB has come from the spatial cross-correlation of XRB fluctuations and faint $B < 23$ galaxies. The original results of Roche et al (1995a) have now been confirmed with an independent analysis on two new deep fields (see Chapter 4). These statistical methods avoid the source confusion problem that prevents faint galaxies from being unambiguously associated with X-ray sources. The amplitude of the cross-correlation implies that $B < 23$ galaxies directly contribute some $20\pm3\%$ of the 1keV XRB. There is also evidence for strong evolution in the X-ray emissivity of galaxies with redshift (see section 4.3.8). An extrapolation to $B < 30$ galaxies suggests that faint galaxies could contribute as large a fraction of the XRB as QSOs and could explain the remainder of the XRB at 1keV.

In this chapter we investigate the X-ray spectra of all the sources identified on our 7 *ROSAT* fields. Other deep surveys (Hasinger et al 1993, Vikhlinin et al 1994) have revealed the possibility that the spectra of the source population may harden as we go to fainter X-ray fluxes, perhaps indicating that we are beginning to identify the missing faint sources required to explain the remainder of the X-ray background. In this work we attempt to identify the type of source responsible for this trend.

5.2 Observational data

5.2.1 The sample

In this chapter we use 7 deep ($21-49$ ks) pointed observations from the *ROSAT* PSPC with optical identifications from the X-ray source catalogue of Shanks et al (in preparation). These are well studied optical fields selected from the ultra-violet excess (UVX) survey of Boyle et al (1990). Our analysis is restricted to the central 18 arcminute radius of the *ROSAT* pointings to maximise the sensitivity of our observations since the point spread function of the PSPC rapidly increases beyond the central 20 arcminute radius. Due to the considerable contamination from both the galactic background and solar scattered X-rays below 0.5keV (Snowden & Freyberg 1993) we optimise the sensitivity of source detection by concentrating on the 0.5-2.0keV data.

Most of this chapter will concentrate on the original 5 *ROSAT* fields from this survey. Two newer observations have been obtained (BJS855 and BJS864), as described in Chapter 2, but since the completeness of optical identification is considerably lower on these fields they will be excluded from the initial analysis to avoid diluting any spectral differences. At the end of the chapter however we will repeat the analysis on these observations and reconcile the results from all seven fields.

Full details of the X-ray source detections and optical spectroscopic identifications are given elsewhere (see Chapter 2 and also Shanks et al, in preparation) and so only brief details will be given below. Sources were identified using the standard PSS algorithm within the *ASTERIX* data processing package, which detects peaks above a certain threshold and matches the expected PSF to the background fluctuations to determine whether the source is real. In this way, 356 X-ray sources were detected above a 4σ significance and 197 sources were detected above 5σ in the 0.5-2keV band on the original 5 *ROSAT* fields. Optical counterparts to these X-ray sources were identified from COSMOS and APM measurements of J and U band UK Schmidt plates. Astrometric transforms between *ROSAT* X-ray and COSMOS/APM co-ordinates were set up using the Durham/AAT UVX QSOs detected by *ROSAT* on each field. Low resolution (12Å) optical spectra were then obtained for the nearest optical counterpart to each X-ray source using the AUTOFIB multi-object system at the Anglo-Australian Telescope.

A summary of the optical identifications of the 4σ sources is given in Table 5.1. Note that this is considerably less complete than the identifications of the smaller list of 5σ sources listed in Georgantopoulos et al (1996) since in this work we are attempting to probe fainter flux limits. Of the 257 sources for which optical identifications were attempted, 128 were identified as QSOs and Seyfert 1 galaxies which directly account for ~30% of the total XRB at 1keV (Shanks et al 1991). Less than 10% of the sources were found to be galactic late type stars. Of the remaining positive identifications, 10 continuum objects and the emission from a galaxy cluster were also detected (Roche et al 1995b). However, as can be seen from Table 5.1, a large fraction of the sources remain unidentified or unobserved (both hereafter referred to as the "unidentified" sources). In many cases, observing limitations prevented the object from being observed or the S/N in the optical spectra was too poor to allow a reliable identification. Interestingly however, ~100 of these unidentified X-ray sources appeared to be associated with faint, "normal" galaxies on photographic plates and for 38 of these sources the optical counterpart was firmly identified as a galaxy by spectroscopy. However, due to the high sky density of galaxies at faint magnitudes (~10000 $\deg^{-2}$ at B<23, Metcalfe et al 1991) and the ~25″ FWHM X-ray error circle, many of these will be chance coincidences. A reliable estimate of the contribution of faint galaxies to the XRB can only be determined statistically (see Chapter 4). However, for the galaxies at brighter limiting magnitudes the confusion problem becomes less pronounced. We therefore identify a sample of "probable" galaxy candidates with B<21.5 for which the optical counterpart lies within 20″ of the X-ray

AGN	128
Stars	27
Continuum	10
Clusters	1
Unobserved	96
Unidentified	89
(Probable galaxies)	(23)
Total	356

Table 5.1: Summary of optical identifications to 4σ sources from 5 deep *ROSAT* fields.

source. By cross-correlating with COSMOS and APM galaxy catalogues on these fields to the same magnitude limit we estimate that ~6 of this restricted sample will spurious identifications. 15 of these galaxies were identified with narrow emission line features and 8 were identified as absorption line galaxies.

5.2.2 Obtaining raw X-ray spectra

For each source the X-ray counts used to determine fluxes, hardness ratios and spectra were obtained using a circle that encloses 90% of the source photons. The radius of this circle increases with off axis angle (Hasinger et al 1992) and is also energy dependent. For a mean photon energy of 1keV this varies from 24.6″ on axis to 56.6″ at the maximum off axis angle of 18 arcminutes. Data from periods of high particle background were excluded from the analysis, excluding approximately 10% of the data when the Master Veto Rate was above 170 counts s^{-1} (Plucinsky et al 1993). Due to the faint nature of many of these sources, considerable care was taken in choosing an area for background subtraction. Possible problems include irregularities in the galactic background or a contamination from solar scattered X-rays. However after the subtraction of sources, the residual background level was found to remain constant over the 18 arcminute central region and no significant gradient in the background level was apparent on any of the fields. Circular areas of 4 to 6 arcminute radius were then chosen from source free regions to perform the background subtraction, correcting for the vignetting effects between the source and background boxes. Further instrumental corrections were then applied. For the energy independent factors (dead time and the obscuration by wires) this amounts to a multiplicative factor of ~1.3 for each spectrum.

Thus the flux, S_i in the i^{th} spectral bin will be given by

$$S_i = (f/T) \times \left[N_{i,source} - (r_S/r_B)^2 \times F_V \times N_{i,bck}\right] \tag{5.1}$$

where $f_c = f_{dead-time} \times f_{wires} \simeq 1.3$ is the instrument correction factor, T is the exposure time, $N_{i,source}$ and $N_{i,bck}$ are the number of photons in the source and background boxes, F_V is the vignetting correction and r_S, r_B are the radii of the source and background boxes respectively.

The resulting variance for each bin will therefore be given by

$$\mathrm{Var}(S_i) = (f/T)^2 \times \left[N_{i,source} + (r_S/r_B)^4 \times F_V^2 \times N_{i,bck}\right] \tag{5.2}$$

For the purposes of spectral fitting, energy dependent factors (due to vignetting and the photons lying outside the source box) are stored as a file extension to give an effective area at each energy.

5.3 Hardness ratios

5.3.1 QSOs and unidentified sources

Since the majority of our sources have fewer than 100 total counts in the *ROSAT* band detailed spectral fitting is not possible. We therefore derive model independent hardness ratios to compare the spectral properties of these sources. By forming a "soft" energy band (S) from the $0.5-1$ keV flux and a "hard" band (H) from $1-2$ keV we define the hardness ratio as:

$$HR = \frac{H-S}{H+S} \tag{5.3}$$

As explained above, our sample was initially selected by excluding the data below 0.5 keV to allow a higher efficiency in source detection. We therefore ignore the very soft flux in the first instance and define our hardness ratios from $0.5-2$ keV in order to characterise the source population fairly without a preferential selection of hard sources. To test for possible systematic biases that might arise due to the combined energy and radial dependence of the PSF the entire sample was split into sources lying within a 10 arminute radius from the centre of the PSPC and those lying beyond. No trend in hardness ratios with off-axis angle was apparent at any flux, as verified by a Kolmogorov Smirnov test on the data.

Removing the known galactic stars, BL Lac objects and the cluster emission we plot the mean hardness ratios for the other 313 X-ray sources on Figure 5.1, binned as a function of flux. These results appear to show a hardening of the mean source spectra

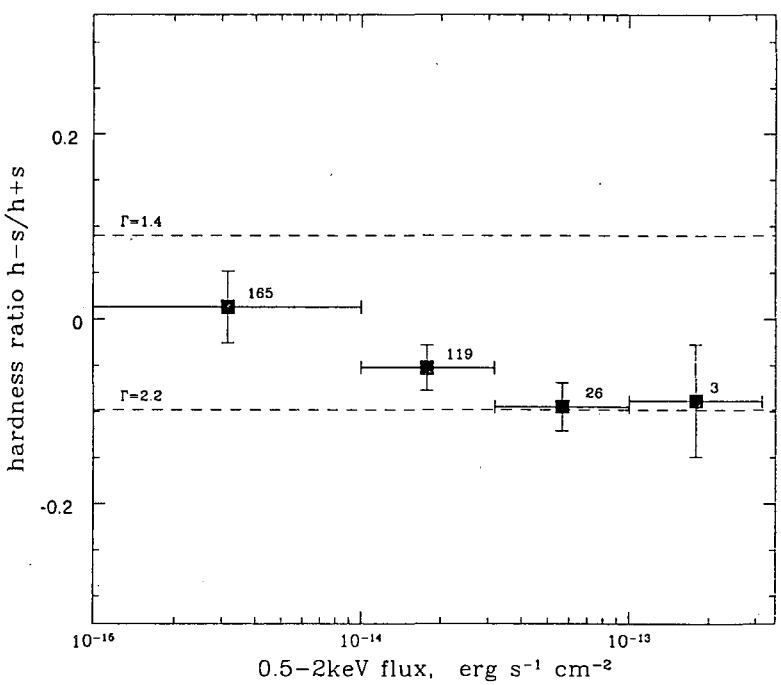

Figure 5.1: Mean $0.5 - 2$keV hardness ratios for 313 X-ray sources from 5 deep (21-49 ks) *ROSAT* fields binned according to flux. Error bars represent the 1σ errors in the mean. The number of X-ray sources within each bin is indicated and for comparison, the hardness ratios for 2 power law models (modified by galactic absorption) are also shown.

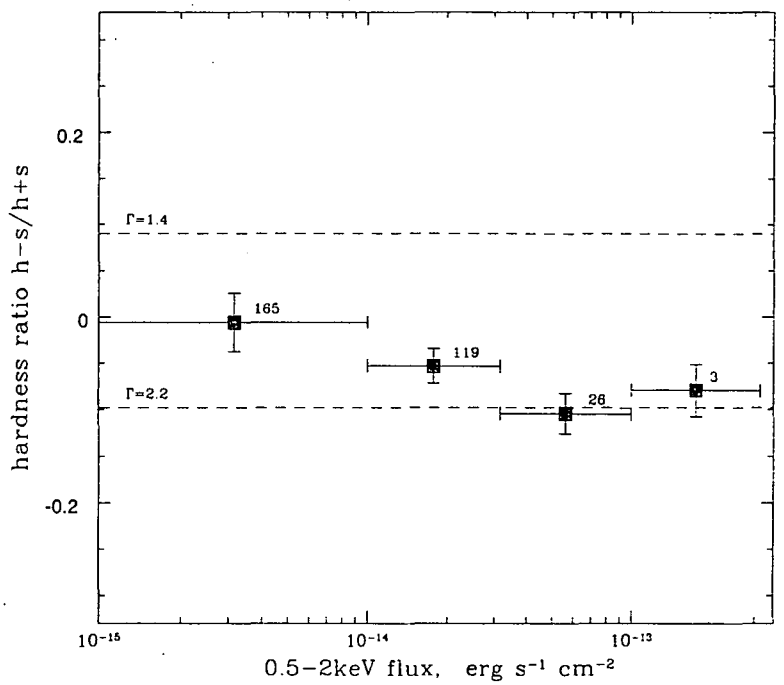

Figure 5.2: Similar to Figure 5.1, but showing the $0.5 - 2$keV hardness ratios for the *stacked* spectra of the sources in each flux bin.

with decreasing flux, as previously suggested by Hasinger et al (1993) and Vikhlinin (1994). Note that replacing the remaining objects has a negligible effect on these results.

A possible problem in analysing *mean* hardness ratios is an artificial skewness in the distribution at faint fluxes. If the instrument is more sensitive in either the H or S bands, individual hardness ratios may be skewed towards $+1$ or -1 as the flux tends to zero and becomes dominated by noise. To overcome this, we will plot hardness ratios of the *stacked* spectra in each flux bin, as shown on Figure 5.2. The similarity of these distributions suggest that this problem does not significantly affect our data. The slight difference between these diagrams is entirely consistent with stacked spectra being more biased towards brighter objects.

Since AGN are the main contributors to the total source flux over the energy range investigated here (Boyle et al 1994), there have been suggestions that an evolution in AGN X-ray spectra may be responsible for the trend in hardness ratios (see Vikhlinin et al and references therein). A hardening of QSO spectra towards higher redshift is postulated, due to either a change in the actual intrinsic spectrum or the effect of intervening absorption from damped Lyα systems. On Figure 5.3(a) we plot the individual hardness ratios, separating QSOs from the other, mostly unidentified sources. The dominant fea-

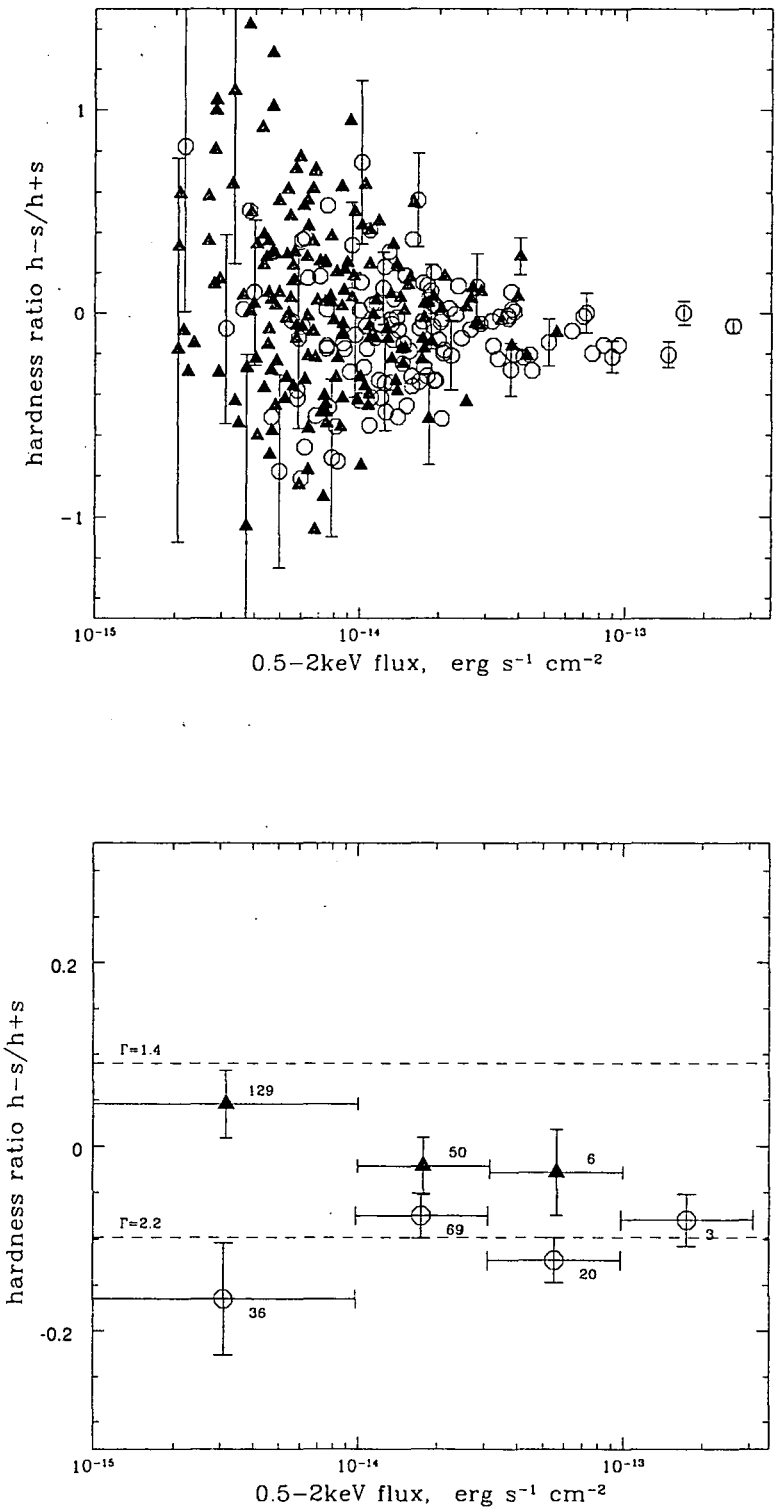

Figure 5.3: (a) Individual 0.5 – 2 keV hardness ratios as a function of flux for QSOs (unfilled circles) and unidentified X-ray sources and galaxies (filled triangles). For clarity, the appropriate 1σ errors are only displayed for a representative selection of sources. On (b) we plot hardness ratios for stacked spectra binned according to flux, as on Figure 5.2, but separating the QSOs from the unidentified sources and galaxies. Note the change in scale compared to (a).

ture on this diagram is the large spread in hardness ratios towards fainter fluxes due to counting statistics. Figure 5.3(b) displays the hardness ratios for the stacked spectra in 4 flux bins. Two features are immediately apparent from these distributions. They appear to show that the unidentified sources have harder mean X-ray spectra than QSOs, regardless of the source intensity. Secondly, the *QSOs show no evidence for spectral hardening with decreasing flux* which seems to indicate that the change in mean source spectra at faint X-ray flux is due to the emergence of another population from within the unidentified sources with an overall harder spectrum than QSOs. Given the incomplete spectroscopic identification in our survey, the unidentified population almost certainly contains some contamination from unidentified steep spectrum QSOs. The mean spectrum of the remaining population may therefore be even harder than indicated on Figure 3.2.

On Figures 5.4(a) and 5.4(b) we also plot QSO hardness ratios as a function of redshift. Again, this illustrates the lack of spectral evolution in our QSO sample from 0.5-2keV, suggesting that broad line AGN are unlikely to account for the missing hard component of the cosmic XRB. Interestingly however, in the softer band below 0.5keV (where the cosmic X-ray background is dominated by galactic emission) there *does* appear to be evidence for a change in QSO spectra with redshift. In this band it is now widely accepted (see Mushotzky et al 1994) that the spectra of QSOs have a significant contribution from a soft excess component, generally believed to be thermal emission from an accretion disk. Using the same sample of QSOs in an independent analysis, Stewart et al (1994) find evidence for a hardening in the spectra of QSOs with redshift in this softer band which has been attributed to changes in the thermal black-body component (see also Mushotzky et al 1993). This evolution is due in part to a redshifting of the soft excess component out of the *ROSAT* passband for higher redshift QSOs, but there also appears to be evidence for a change in the temperature and normalisation of this component. However, we are concerned here with the origin of the missing hard component of the extragalactic X-ray background above 0.5keV and in this band (as shown by Figures 5.3 and 5.4) we find no evidence for any evolution in the X-ray spectra of QSOs.

5.3.2 X-ray luminous galaxies

In Section 5.2 we noted that ~100 of the 184 unidentified sources appear to be associated with faint optical galaxies. The cross-correlation results of Chapter 4 suggest that many of these are likely to be genuine X-ray sources but due to the high sky density of "normal" field galaxies at faint magnitudes there will also be a significant number of chance associations. We therefore selected a restricted sample of the most likely galaxy candidates with brighter optical magnitudes (B<21.5) and lying within 20″ of the X-ray source. In total 23 galaxies meet this criteria from which we expect only

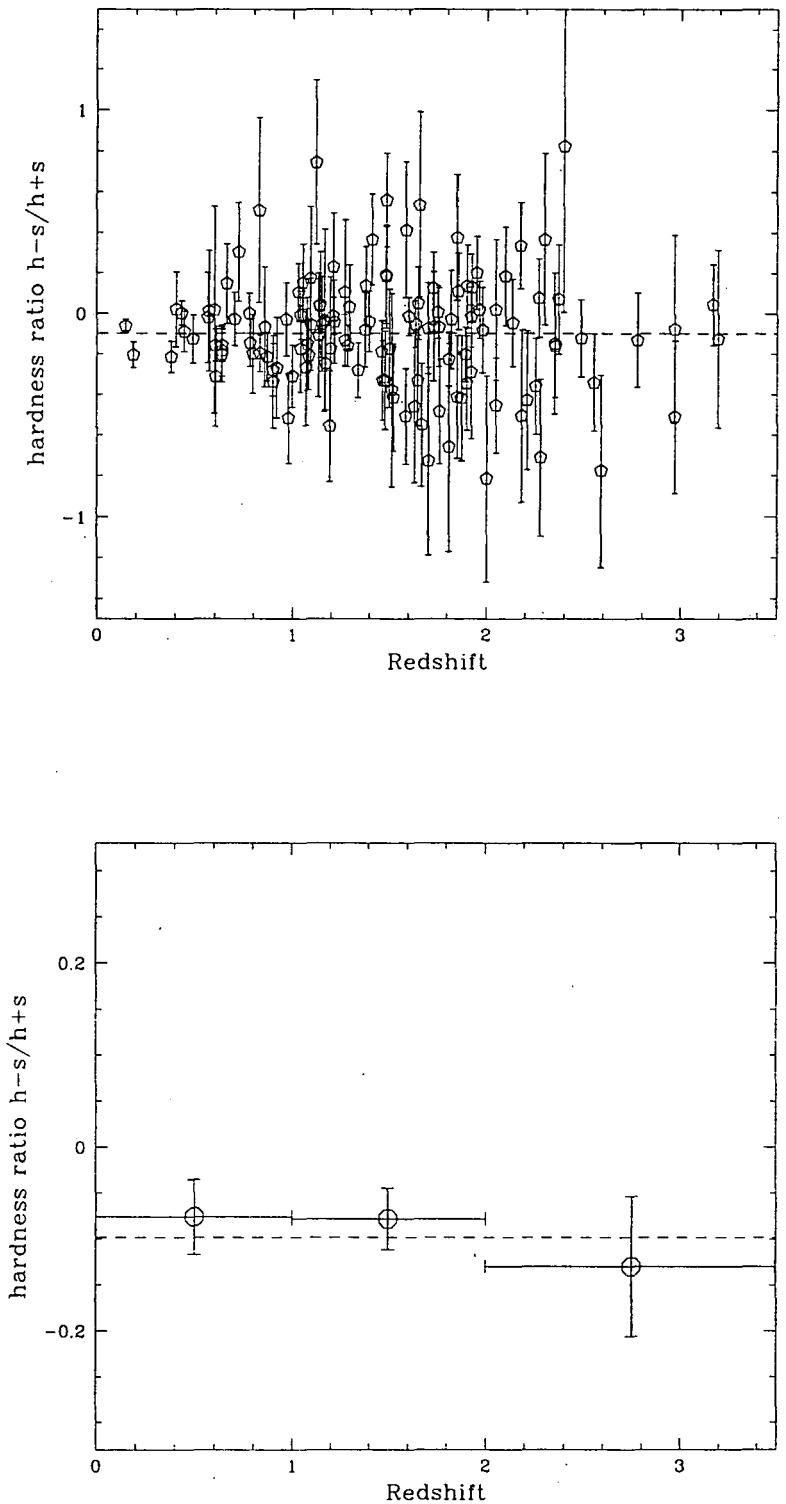

Figure 5.4: (a) Showing hardness ratios as a function of redshift for the 128 QSOs detected on these fields, while (b) shows the mean hardness ratios when binned according to redshift with 1σ errors representing the rms error on the mean. The dotted line shows the mean QSO hardness ratio.

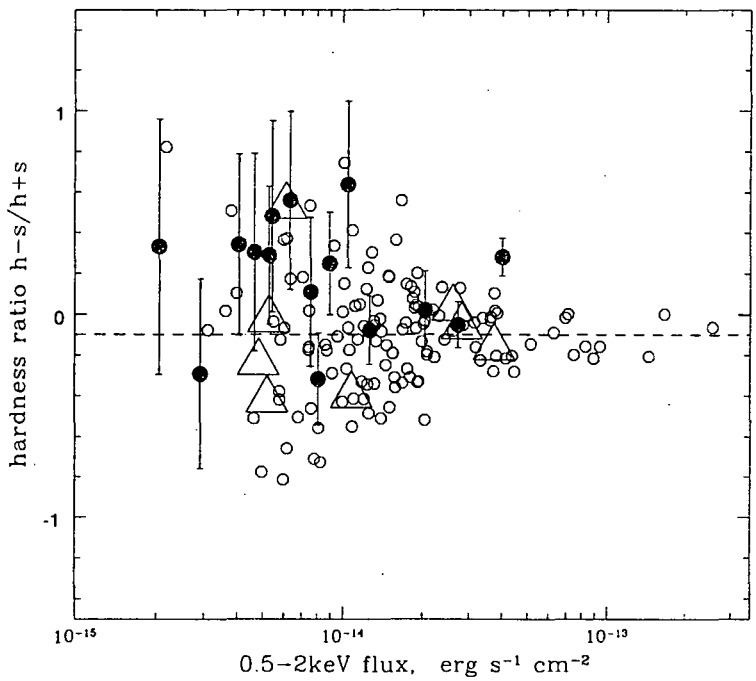

Figure 5.5: Hardness ratios as a function of flux for the 23 most likely X-ray emitting galaxies with the sample of 128 QSOs (unfilled circles) for comparison. Galaxies are separate into 8 absorption line objects (unfilled triangles) and 15 narrow emission line galaxies (filled circles). The mean hardness ratio for QSOs is also displayed (dotted line) and for clarity the 1σ error bars are only displayed for the emission-line galaxies.

$\sim$6 to be spurious identifications. The hardness ratios for these X-ray sources and the 128 QSOs are displayed on Figure 5.5, in which the 15 narrow emission line galaxies are separated from the 8 absorption line galaxies. Despite the limited sample and the large errors on individual faint sources, there is clearly evidence that the emission line galaxies in particular come from a harder population than the QSOs. While the 8 absorption line galaxies are evenly distributed about the mean hardness ratio for QSOs, 13 of the 15 emission line galaxies lie formally above this mean value. On Figure 5.6 we display the hardness ratios for QSOs and emission line galaxies binned according to flux. A Kolmogorov-Smirnov test yields a 98.6% probability that the hardness ratios associated with the emission line galaxies and QSOs do not arise from the same parent population. The cumulative distributions are shown on Figure 5.7.

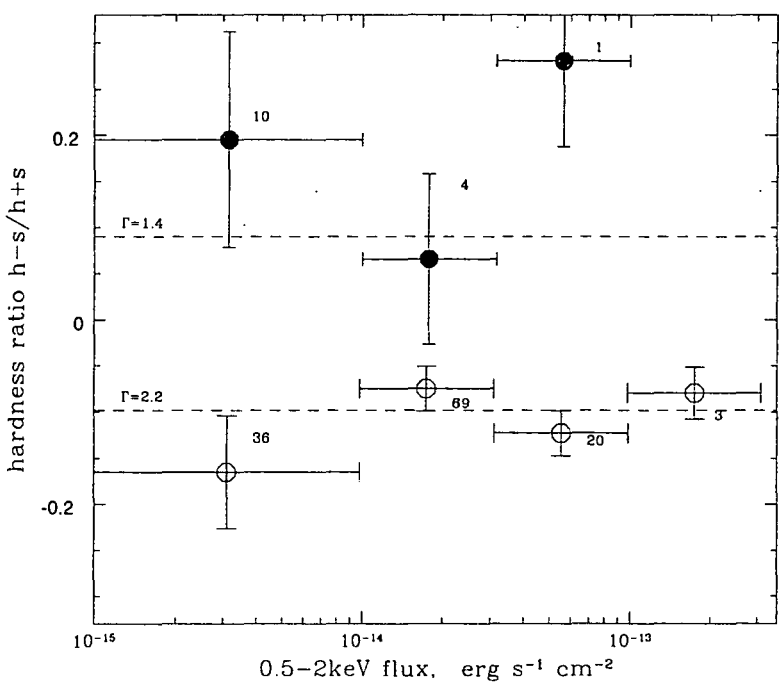

Figure 5.6: Hardness ratios for the stacked spectra of the 15 emission line galaxies (filled circles) and 128 QSOs (unfilled circles) shown Figure 5.5.

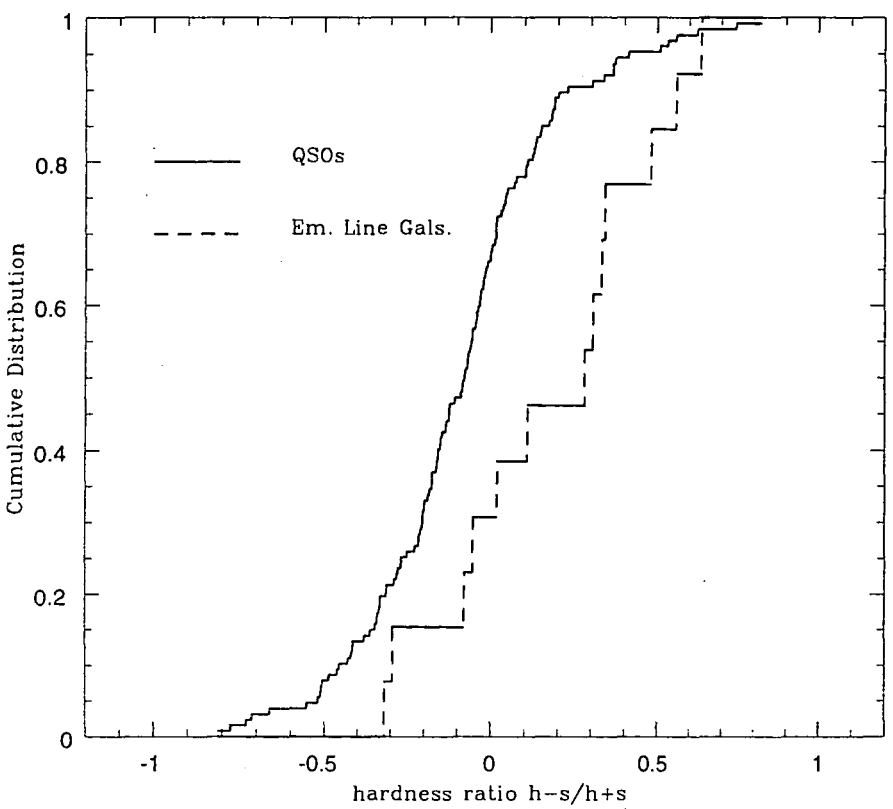

Figure 5.7: Cumulative probability distributions for the 15 emission line galaxies and 128 QSOs shown on Figure 5.5 (Kolmogorov-Smirnov test).

5.4 Spectral fitting

Field	RA	DEC	N_H	Exposure time
GSGP4	00 57 28.7	-27 38 24	1.8	48955
SGP2	00 52 04.8	-29 05 24	1.8	24494
SGP3	00 55 00.0	-28 19 48	1.8	21062
QSF1	03 42 09.6	-44 54 36	1.7	26144
QSF3	03 42 14.3	-44 07 48	1.7	27358

Table 5.2: Summary of *ROSAT* fields, with coordinates in J2000 and galactic column density in 10^{20} atom cm^{-2}.

5.4.1 Stacked spectra

In Section 5.4 we used hardness ratios to analyse the X-ray spectra of individual faint sources. In this section we analyse the X-ray spectra in more detail using the full resolution of the PSPC detector by stacking together the spectra of different source types.

Details of the five *ROSAT* fields used in this analysis are summarised in Table 5.2. The column densities of galactic hydrogen are very similar on each field, but a mean value weighted by exposure times was used if any stacked spectra were obtained from different fields. For the spectral fitting, the response matrix DRM_06 was used for observations made before October 1991 (QSF1 and QSF3) while the matrix DRM_036 was used for observations made after that date (SGP2, SGP3 and GSGP4). Although problems in the calibration of the PSPC (see Turner et al 1995) can lead to some uncertainties in the spectral fits, we are primarily concerned with broad *differences* between the spectra of different sources which should be unaffected by these problems.

Using the XSPEC spectral analysis package we attempt fitting power-law models (modified only by galactic absorption) to the stacked spectra of QSOs, unidentified X-ray sources and the subset of probable galaxies. We emphasise that no particular physical significance should be attributed to these models and we are merely attempting to parameterise the spectral differences between the source types. For comparison with the hardness ratio analysis in section 5.3 we also perform the fits using only the 0.5-2keV data. The results (see Table 5.3) confirm that the unidentified sources, on average, have a harder spectrum than QSOs. In agreement with the hardness ratio analysis, the subset of probable X-ray emitting galaxies (emission line galaxies in particular) appear to have a significantly harder spectrum than QSOs. The raw channel spectra for the QSOs, unidentified sources and the subset of narrow-line X-ray galaxies are displayed on Figure 5.8 with the best fitting power-law models.

Energy	Source Type	No.	Γ	$\chi^2_{\rm red}$
$0.5-2.0\,$keV	QSOs	128	2.23±0.04	0.51
	Unidentified	185	1.81±0.06	0.95
	Probable galaxies	23	1.64±0.14	1.18
	(Em. line gal.)	15	1.36±0.18	1.91
	(Abs. line gal.)	8	2.21±0.23	1.25
$0.1-2.0\,$keV	QSOs	128	2.30±0.01	8.70
	Unidentified	185	1.74±0.03	3.17
	Probable galaxies	23	1.69±0.06	1.45
	(Em. line gal.)	15	1.51±0.09	1.79
	(Abs. line gal.)	8	1.94±0.08	1.02

Table 5.3: Results of power-law fits to the stacked spectra from all fields, separated according to QSOs, unidentified sources and the subset of probable galaxies. Fits are performed using the $0.5-2.0\,$keV data for comparison with the hardness ratio analysis and with the full $0.1-2.0\,$keV *ROSAT* band. Values of photoelectric absorption are fixed at the mean galactic value.

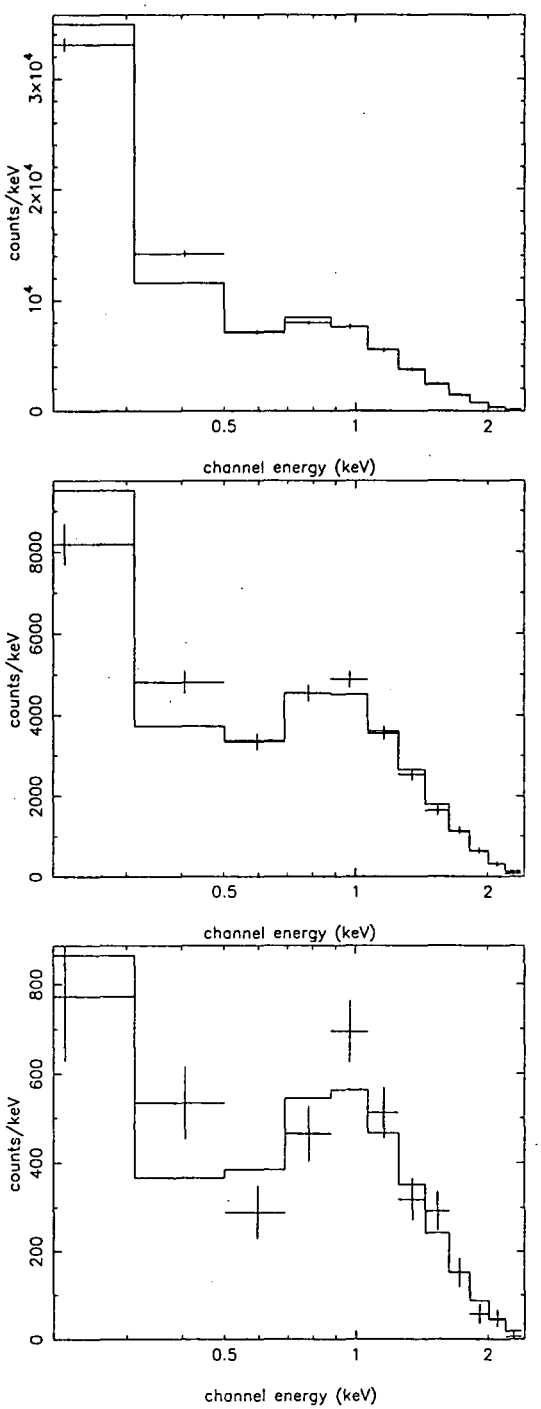

Figure 5.8: The stacked $0.1 - 2.0$ keV X-ray spectra with the best fitting power-law models for (a) the 128 QSOs ($\Gamma = 2.30 \pm 0.01$) , (b) the 185 unidentified X-ray sources ($\Gamma = 1.74 \pm 0.03$) and (c) the 15 probable narrow emission-line galaxies identified as a subset of (b) ($\Gamma = 1.51 \pm 0.09$). In each case the photoelectric absorption was fixed at the mean galactic value.

		QSOs		Unidentified	
Energy	Field	Γ	χ^2_{red}	Γ	χ^2_{red}
0.5 – 2.0 keV	GSGP4	2.13±0.08	1.52	1.65±0.11	1.08
	SGP2	2.16±0.11	1.56	1.74±0.15	1.01
	SGP3	2.38±0.10	1.43	2.30±0.13	0.89
	QSF1	2.19±0.12	1.44	1.84±0.19	0.25
	QSF3	2.44±0.11	1.98	1.71±0.17	1.69
0.1 – 2.0 keV	GSGP4	2.08±0.03	5.63	1.36±0.07	3.83
	SGP2	2.28±0.03	4.65	1.63±0.07	2.37
	SGP3	2.27±0.03	3.84	2.23±0.04	0.96
	QSF1	2.41±0.03	2.11	1.85±0.09	0.30
	QSF3	2.64±0.03	1.98	1.95±0.07	1.68

Table 5.4: Results of power-law fits to the stacked spectra from each field, fixing the photo-electric absorption to the galactic values shown in Table 5.2. The fits are performed using the 0.5 – 2.0 keV data and the full 0.1 – 2.0 keV *ROSAT* band.

Treating each of the 5 *ROSAT* fields separately, Table 5.4 displays the results of power-law fits to the stacked spectra of QSOs and unidentified sources. On 4 of the 5 fields there are significant spectral differences between the spectra. Note that the largest difference comes from the deepest (49ks) exposure on the GSGP4 field while on the shortest (21ks) exposure on SGP3 the difference in spectra is negligible, consistent with the picture that a harder population is emerging at fainter fluxes, in agreement with Figure 5.2.

As Tables 5.3 and 5.4 show, a simple power-law is a reasonable fit to all the stacked data above 0.5keV for all source types. For the full band 0.1 – 2 keV fits however, the values of χ^2_{red} suggest that more detailed models are required to fit the data. For the QSOs in particular, a soft excess component is required below 0.5keV, as described by Stewart et al (1994), but since we are interested only in their contribution to the extragalactic XRB we make no attempt to model this here. Since the 0.5 – 2.0 keV hardness ratios for QSOs remain constant with redshift this would indicate that we are dealing with a power-law spectrum above 0.5 keV without a significant contribution from a soft excess component.

5.4.2 Individual galaxy spectra

Source	S ($\mathrm{erg\,s^{-1}cm^{-2}}$)	N_{bins}	Γ	χ^2_{red}	Max. N_H	Redshift	Em/Abs
GSGP4X : 091	4.01×10^{-14}	7	0.14±0.30	2.77	10.8×10^{21}	0.416	Em
GSGP4X : 017	3.72×10^{-14}	7	2.25±0.09	1.24	0.05×10^{21}	0.105	Abs
QSF1X : 020	2.81×10^{-14}	7	1.95±0.21	0.33	0.40×10^{21}	0.382	Abs
GSGP4X : 048	2.71×10^{-14}	7	1.82±0.15	1.83	0.35×10^{21}	0.155	Em
SGP3X : 006	2.52×10^{-14}	4	1.62±0.18	0.64	0.56×10^{21}	0.258	Abs
QSF1X : 036	2.04×10^{-14}	4	2.49±0.18	0.67	0.01×10^{21}	0.551	Em
GSGP4X : 069	1.26×10^{-14}	4	0.79±0.51	3.67	6.70×10^{21}	0.213	Em
GSGP4X : 064	1.08×10^{-14}	3	1.77±0.45	0.55	2.90×10^{21}	0.097	Abs
SGP3X : 033	1.04×10^{-14}	4	2.01±0.21	0.78	0.30×10^{21}	0.195	Em
Faint (10)	$< 1.00 \times 10^{-14}$	7	1.69±0.16	0.70	0.49×10^{21}	-	Em
Faint (4)	$< 1.00 \times 10^{-14}$	4	1.68±0.31	1.03	1.20×10^{21}	-	Abs

Table 5.5: Summary of $0.1 - 2.0\,\mathrm{keV}$ spectral fits to the brightest 9 X-ray emitting galaxies plus the stacked spectra of the fainter galaxy sources. For the power-law fits the photoelectric absorption is fixed at the galactic value. Column 6 lists the 90% upper limits to the intrinsic absorption at the redshift of the galaxy in $\mathrm{atom\,cm^{-2}}$, assuming an underlying power-law of $\Gamma = 2.2$.

The stacked X-ray spectra for the X-ray luminous galaxies appear to be significantly flatter than the combined spectra for the QSOs in our survey. While most of the individual sources yield a total of fewer than 40 X-ray photons in the $0.1 - 2.0\,\mathrm{keV}$ band , it is important to establish whether the overall flat spectrum is due to individual spectra that are intrinsically flat or possibly (as predicted by, eg. Comastri et al 1995) a superposition of absorbed X-ray spectra with correspondingly distinct low energy cutoffs.

In Table 5.5 we show the results of power-law fits (with galactic absorption) for X-ray spectra of the 9 brightest galaxies with a flux $S(0.5 - 2.0\ \mathrm{keV}) > 1 \times 10^{-14}\mathrm{erg\,s^{-1}cm^{-2}}$. For the fainter galaxies no meaningful information could be extracted individually. These spectra were therefore stacked together before spectral fitting, separating only the 4 absorption and 10 emission line objects. A power-law model gives a reasonable fit to 7 of the 9 brightest galaxies and to the stacked spectra of the fainter sources, with photon indices $\Gamma = 1.62$ to 2.49. For 2 galaxies however (GSGP4X:091 and GSGP4X:069), simple power-law models do not give an acceptable fit to the data. Both of these are emission line galaxies and they both show very hard X-ray spectra with $\Gamma < 1$.

- **GSGP4X:091** For this object, the brightest of the galaxy candidates, a power-law plus galactic absorption model gives a very flat Γ=0.145 but is not a good fit to the data ($\chi^2_{\rm red}$=2.73). A thermal Raymond-Smith model also gives a very poor fit to the data. The lack of photons at soft energies seems to indicate photoelectric absorption. We therefore try adding an absorbing column at the redshift of the galaxy and assume an intrinsic power-law of Γ=2.2 (the mean value for QSOs). This gave a much improved fit with an intrinsic column density of $N_H = 7.5 \pm 1.8 \times 10^{21}$ atom cm^{-2} ($\chi^2_{\rm red}$=0.97). The channel spectrum and best fitting model are shown on Figure 5.9. Note that an equally good fit can be obtained with a similar degree of obscuration and a thermal Raymond-Smith model with a temperature of ~2keV. The X-ray spectrum therefore presents strong evidence that this is a highly luminous , obscured X-ray source with an unobscured $0.5-2$ keV rest-frame luminosity of $\sim 1.3 \times 10^{44}$ erg s^{-1} ($H_0 = 50$ km s^{-1}Mpc^{-1}, $q_0 = 0.5$).

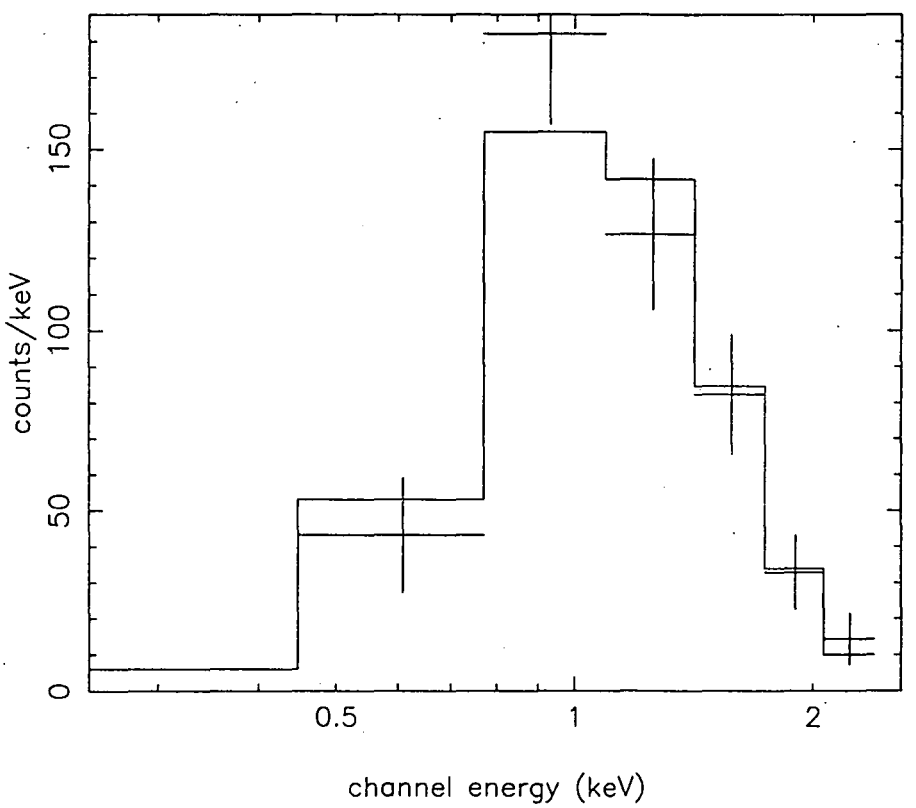

Figure 5.9: 0.1−2.4keV X-ray spectrum for the narrow-emission line galaxy GSGP4X:091 with the best fitting absorbed model.

- **GSGP4X:069** A power-law with only galactic absorption gives a very flat Γ=0.79, but this is not a good fit to the data ($\chi^2_{\rm red}$=3.62). This faint source has only 46 photons from $0.5-2.0\,$keV but nevertheless it also shows evidence for photoelectric absorption at low energies. Repeating the background subtraction with various source free regions near the source confirms that this is not a systematic effect. Adding an absorbing column at the redshift of the galaxy and fixing the intrinsic power-law component to $\Gamma = 2.2$ gave a much improved fit to the data ($\chi^2_{\rm red}$=0.53) with a restframe absorbing column of $N_H = 2.7 \pm 1.9 \times 10^{21}\,$atom cm^{-2}. The channel spectrum and best fitting absorbed model are shown on Figure 5.10.

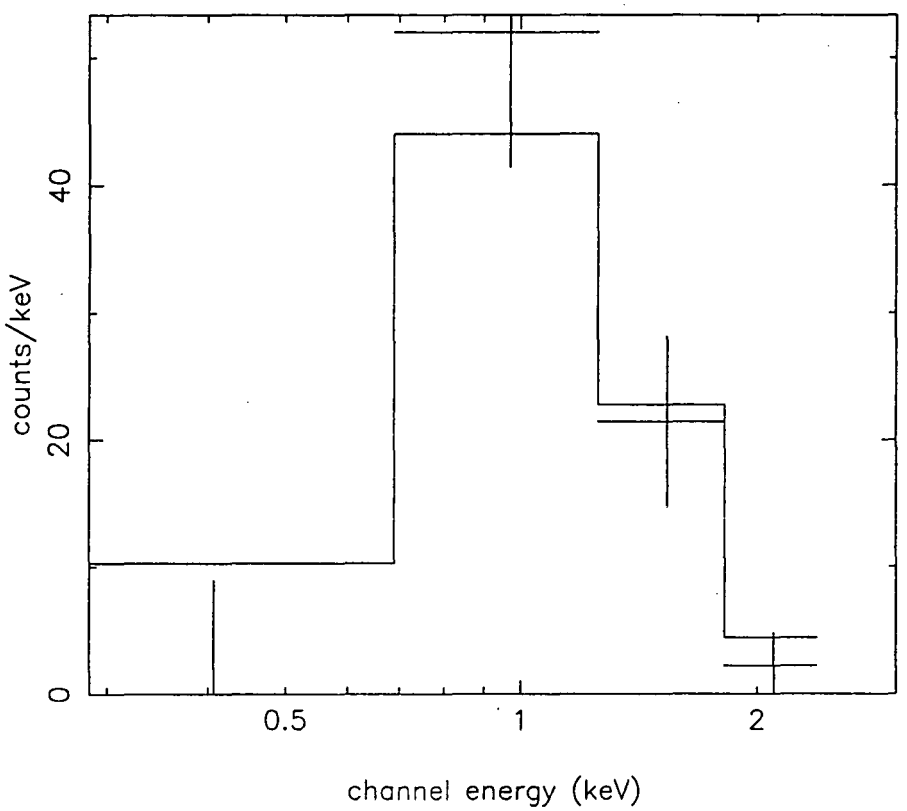

Figure 5.10: $0.1-2.4\,$keV X-ray spectrum for the narrow-emission line galaxy GSGP4X:069 with the best fitting absorbed model.

The results show that the X-ray luminous galaxies have a mixture of spectral properties, from very flat X-ray sources with evidence of significant photoelectric absorption to those with steep QSO-like spectra. While only these 2 galaxies *require* additional absorption above the galactic value, a number of the remaining galaxies and the stacked spectra of the fainter sources are best fit by power-law X-ray spectra significantly flatter than QSOs. It would be interesting to determine if these galaxies are intrinsically flat or whether this is also due to obscuration. Unfortunately there are insufficient photons to provide useful constraints on both the power-law index and the rest-frame absorption, but we find that these sources are equally well fit by a steeper power-law and a low level of photoelectric absorption ($N_H < 1.0 \times 10^{21}\,\mathrm{atom\,cm^{-2}}$). We estimate the upper limits on the intrinsic N_H by fixing the power-law component at the mean QSO value of Γ=2.2 and allowing the restframe absorption to vary.

5.5 The fields BJS855 and BJS864

We now consider the 2 newer *ROSAT* fields which were excluded from the previous analysis since (due to problems in fibre positioning) the optical identification is $\sim$ 30% less complete than the first 5 fields. A further complication is the higher galactic column density for these fields ($N_H = 3 \times 10^{20}\,\mathrm{atom\,cm^{-2}}$) which forces us to analyse the spectra separately.

As described in Chapter 1, additional X-ray data was obtained from the *ROSAT* data archive for both of these fields. These serendipitous pointings were offset 5.6 and 6.9 arcminutes from the centers of the BJS855 and BJS864 fields respectively. The additional spectral data was only added for sources lying within the 20 arcminute central radius of the offset field centre to avoid obscuration by wires and the significant drop in sensitivity beyond this radius. This gave a total of 57147 and 52466 seconds exposure in the overlapping regions. X-ray spectra were then obtained separately for each set of data before combining, thus allowing for the variation in the PSPC response with off-axis radius.

Removing only the known galactic stars Figure 5.11(a) shows the 0.5 – 2 keV hardness ratios for the 37 QSOs, 1 narrow-line QSO and the 65 unidentified sources and galaxies. On Figure 5.11(b) we plot the hardness ratios for the stacked spectra in each flux bin. The results show marginal differences between the QSOs and the remaining sources, though not as significant as the results from the original 5 *ROSAT* observations (see Figure 5.3). Nevertheless, the unidentified population does show evidence for hardening at the faintest flux while the QSOs retain the same mean hardness ratio. More detailed spectral fitting to the total stacked spectra gives a good fit with a power law slope of $\Gamma = 2.15 \pm 0.12$ for the QSOs and $\Gamma = 1.90 \pm 0.08$ for the unidentified sources.

However the density of QSOs on the other fields suggest that at least $\sim 30\%$ of the QSOs have not been identified in these observations. Once these QSOs have been identified it is probable that the true difference in spectra will be more significant.

As before, we now consider the subset of unidentified sources selected as the best galaxy candidates. Optical spectra and redshifts were obtained for 20 galaxies as optical counterparts to X-ray sources and from these 13 meet the criteria of having $B < 21.5$ and lying within 20 arcseconds of the X-ray source and are classified as "likely" X-ray sources. Cross-correlation with COSMOS galaxy catalogues to the same flux limit suggests that we only expect $\sim$3 of these to be spurious associations (see Chapter 4). Optical spectra reveal that 11 of these were identified as emission-line galaxies while 2 showed only absorption line properties. The hardness ratios for these X-ray sources compared with QSOs are shown on Figure 5.12(a). Once again, the emission-line galaxies show evidence for having a harder overall spectrum than QSOs, with 9 of these 11 galaxies lying formally above the mean value for QSOs. On Figure 5.12(b) we show the hardness ratios of the stacked spectra in different flux bins. While the only bright emission-line galaxy shows a steep X-ray spectrum, the stacked spectra of the 10 fainter galaxies give a hardness ratio consistent with a spectral index of $\Gamma = 0.9 \pm 0.4$, significantly harder than the QSOs.

Of the individual galaxies, only the bright emission line object has sufficient photons to permit a more detailed analysis than hardness ratios and this gives a relatively steep power law index of $\Gamma = 2.49 \pm 0.18$ (with galactic absorption) from $0.1 - 2\,\mathrm{keV}$. Stacking the 10 fainter emission-line galaxies a spectral fit with 7 energy bins gives a best fit power law slope of $\Gamma = 0.87 \pm 0.46$ from $0.1 - 2\,\mathrm{keV}$ (χ^2_{red}=0.61) with only galactic absorption. Including the bright object steepens the best fit to $\Gamma = 1.31 \pm 0.35$ (χ^2_{red}=1.36), still significantly flatter than the mean QSO spectrum.

Given the low signal to noise of individual spectra, we cannot distinguish whether these fainter galaxies have hard X-ray spectra because of photoelectric absorption (which might indicate an obscured AGN) or if they have spectra which are intrinsically flat. Fixing the power law index at the mean value for QSOs, $\Gamma = 2.2$, we can also obtain a good fit (χ^2_{red}=0.91) with an intrinsic absorbing column of $N_H = 5.2 \pm 2.0 \times 10^{21}\,\mathrm{atom\,cm^{-2}}$ at the mean redshift of the galaxies. It is of course possible that individual objects may have spectra consistent with higher absorbing columns, but we require better data to test this.

Overall therefore these results are broadly consistent with those obtained from the first 5 *ROSAT* observations.

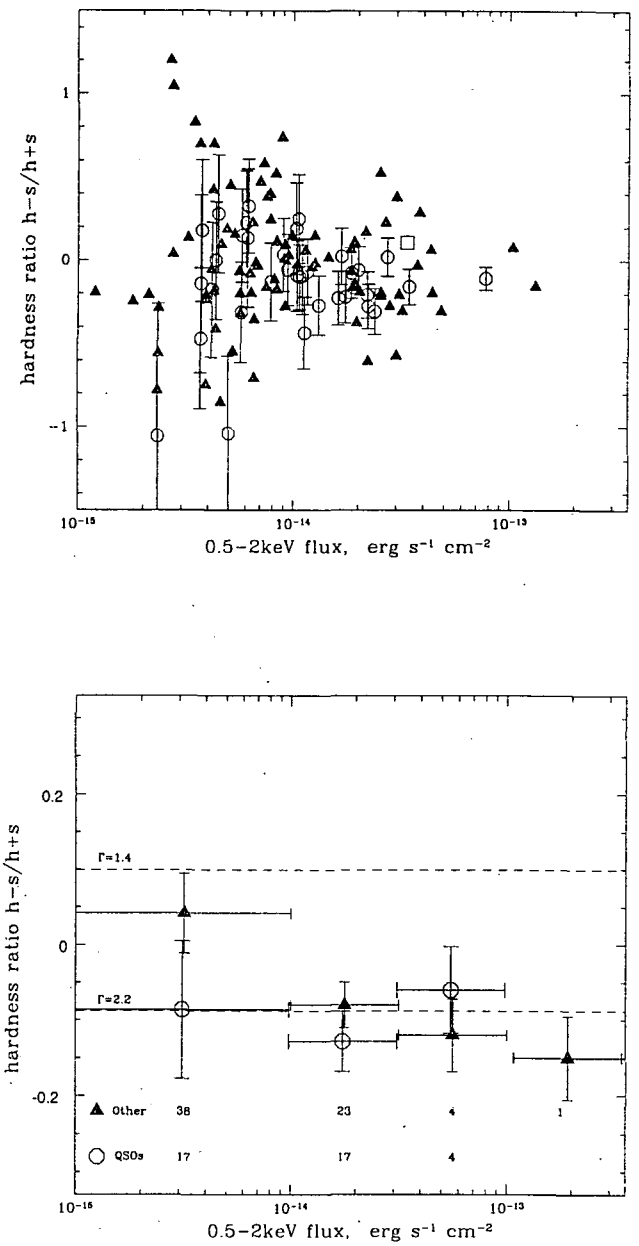

Figure 5.11: (a) Individual $0.5-2\,\mathrm{keV}$ hardness ratios vs flux for the 37 QSOs and 96 unidentified sources identified on the BJS855 and BJS864 fields. Appropriate 1σ errors are displayed only for the QSOs for clarity. On (b) we display the hardness ratios for the stacked spectra in each flux bin. The number of objects in each bin are shown. The hardness ratios for the two power law models are also displayed, modified to allow for the galactic absorbing column on these fields.

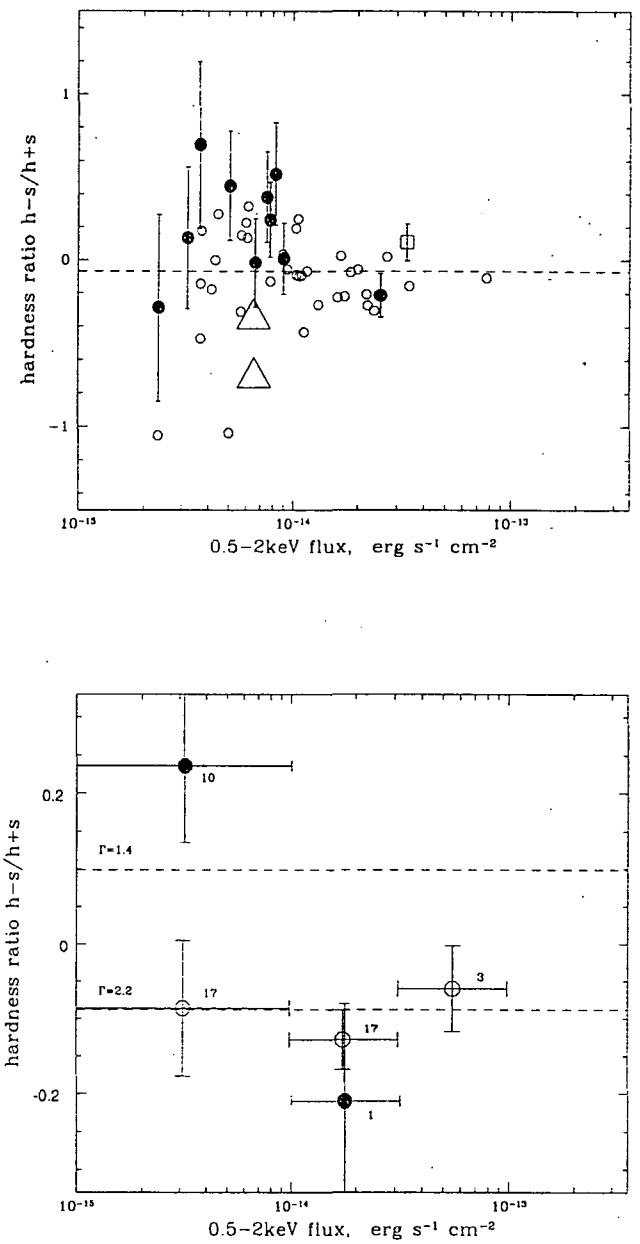

Figure 5.12: (a) Individual $0.5-2$ keV hardness ratios vs flux for the 37 QSOs (unfilled circles), 1 narrow-line QSO (unfilled square) and the 13 most likely X-ray emitting galaxies identified on the BJS855 and BJS864 fields. Galaxies are separated into 11 emission-line galaxies (filled circles) and 2 absorption line galaxies (unfilled triangles). The mean QSO hardness ratio is also displayed. On (b) we show hardness ratios for the stacked spectra in each flux bin.

5.6 Summary and conclusions

We have used a sample of over 400 X-ray sources detected on 7 deep (21-49ks) *ROSAT* fields to investigate the X-ray spectra of the source population. Using a hardness ratio analysis we confirm recent claims that the average source spectra harden towards fainter fluxes from an equivalent photon index of $\Gamma = 2.2$ at $S(0.5-2.0\,\mathrm{keV}) = 1 \times 10^{-13}\mathrm{erg\,s^{-1}cm^{-2}}$ to $\Gamma \simeq 1.7$ below $1 \times 10^{-14}\mathrm{erg\,s^{-1}cm^{-2}}$.

We then attempt to show the type of source responsible for this trend. So far 167 QSOs have been identified from this survey, and these are the dominant source population at X-ray fluxes above $1 \times 10^{-14}\mathrm{erg\,s^{-1}cm^{-2}}$, but at fainter fluxes the X-ray sources remain largely unidentified. On the 5 fields where the optical identifications are most complete we find that the unidentified sources have a harder mean X-ray spectrum than QSOs, regardless of source intensity. We also show that the QSOs detected so far in our survey show no evidence for spectral hardening with decreasing flux, implying that the change in mean spectra is due to the emergence of another population from within the unidentified sources.

The work of Chapter 4 suggests that many of the unidentified sources are X-ray luminous galaxies (see also Roche et al 1995, McHardy et al 1995). Taking a subset of 36 X-ray sources identified as the most likely galaxy candidates, we find that the 26 emission-line galaxies in particular have mean hardness ratios significantly harder than QSOs. Stacking the spectra of these faint sources, the emission-line galaxies yield a spectral index of $\Gamma = 1.51 \pm 0.09$ on the original 5 fields and $\Gamma = 1.31 \pm 0.35$ on the BJS fields, more consistent with the residual X-ray background. Individually, the galaxies show a range of spectral properties from very hard X-ray sources to those with soft, QSO-like spectra. At least 2 emission-line galaxies show evidence for significant photoelectric absorption in the range $N_H \sim 10^{21} - 10^{22}\,\mathrm{atom\,cm^{-2}}$.

Therefore these spectral results provide further evidence that X-ray luminous galaxies may be the solution to explaining the origin of the X-ray background.

Chapter 6

Conclusions

This thesis presents a study of faint X-ray sources in an attempt to understand the origin of the X-ray background and to investigate the variability characteristics of the QSO population. A number of interesting results were obtained which will now be summarised.

6.1 QSO X-ray variability

A study of QSO X-ray variability was carried out using a sample of over 100 QSOs identified in the optical spectroscopic follow-up of faint *ROSAT* sources. This represents the first study of a flux limited sample of typical radio quiet QSOs over a wide range of redshift and luminosity. Previous studies have concentrated on local, bright AGN. The main results were as follows:

(i) Given sufficient signal to noise, most QSOs show evidence for low level variability on timescales of hours to days. The mean amplitude of variability, $\sim$ 27% rms, appears to be 'typical' of the QSO population.

(ii) Contrary to the results found with local AGN, there is no evidence for a decline in variability amplitude with luminosity. The mean amplitude of variability remains constant over 2 orders of magnitude in L_x. Similarly, there is no evidence for any change in variability with redshift over the range $0.1 < z < 3$. This may suggest that the emitting regions in QSOs have the same physical size regardless of redshift, which favours a short lived model for QSO evolution.

(iii) There is no evidence to suggest that QSOs with a particular X-ray spectrum show differing variability amplitude.

(iv) A highly variable Seyfert galaxy was discovered. The large amplitude variability suggests an upper limit of $M < 1.2 \times 10^8 M_\odot$ for the black hole mass. This QSO also changes X-ray spectrum, becoming softer as the flux increases. Detailed spectral fitting suggests only one acceptable model for this variability in which the change in spectrum is caused by differential brightening of a soft excess relative to a steep power law component. Such variability is inconsistent with a reprocessing model for AGN.

6.2 The X-ray background

Much of this thesis is concerned with understanding the X-ray background and the nature of the faint X-ray source population. The main conclusions from this work are as follows:

(i) Cross-correlating the unidentified X-ray sources on 3 deep ($\sim$ 50ks) *ROSAT* fields with galaxy catalogues suggests that faint galaxies with $b_j < 23$ can account for $21 \pm 6\%$ of all X-ray sources to a limiting flux of $\sim 4 \times 10^{-15}$ erg s^{-1} (0.5-2keV).

(ii) By removing the X-ray sources and cross-correlating the *unresolved* XRB with faint galaxies a highly significant signal is obtained on 3 deep fields, confirming the results of Roche et al (1995). By comparing this signal with the theoretical cross-correlation, allowing for the enhancement due to clustering, an estimate for the local volume emissivity of galaxies is obtained at $\rho_o \simeq 4.6 \pm 0.7 \times 10^{38} h$ erg s^{-1} Mpc^{-3}. The mean X-ray to optical ratios imply that faint $b_j < 23$ galaxies account for $\sim 20\%$ of the XRB. Extrapolation to higher redshifts and fainter magnitudes increases this fraction to $\sim 50\%$.

(iii) Using a formalism developed by Treyer & Lahav (1995), cross correlations of the the unresolved XRB with two magnitude slices from an optical galaxy catalogue allows an estimate of the X-ray evolution of faint blue galaxies. The results imply very strong evolution of the form:

$$L_x \propto (1+z)^{3.3 \pm 1.2} \tag{6.1}$$

This leads to a revised estimate that faint galaxies can contribute $50 - 100\%$ of the unresolved XRB at 1keV.

(iv) An analysis of the X-ray spectra of faint *ROSAT* sources confirms recent findings that the mean spectrum hardens at increasingly faint X-ray flux. The optical identifications from our survey allow this analysis to be taken a step further. The results show that QSOs do not show this hardening and retain a steep spectrum

at faint fluxes. The trend in mean spectral index is caused by the emergence of an unidentified X-ray population at faint X-ray flux.

(v) A sample of X-ray luminous galaxies show significantly harder mean X-ray spectra than QSOs, with a mean photon index of $\Gamma \simeq 1.5 \pm 0.1$ compared to $\Gamma \simeq 2.2 \pm 0.1$ for QSOs.

(vi) A number of the brighter X-ray luminous galaxies permit individual spectral fitting. These show a wide range of X-ray spectra, from sources with steep X-ray spectra to those with evidence for significant photoelectric absorption. The stacked spectra of the fainter galaxies suggest 90% upper limits on the photoelectric absorption of $\sim 10^{21}$atom cm^{-2}.

(vii) A rare example of a luminous, high redshift obscured QSO has been discovered by X-ray selection. The UV spectrum shows narrow emission lines (< 900 km s^{-1}). A fairly hard X-ray spectrum ($\Gamma = 1.56$) suggests that the dust and gas associated with a moderate obscuring column of $\sim 2 \times 10^{21}$atom cm^{-2} is extinguishing the broad line region. The detection of broad $H\alpha$ confirms that this is an obscured QSO. The surprisingly high UV continuum ($M_B = -23.6$) suggests the presence of a bright host galaxy.

6.3 Future prospects

It now seems established beyond doubt that a population of faint galaxies, or some processes associated with them, emit vast quantities of X-ray emission which could in principle account for the origin of the XRB (Chapter 4). The hardness of their X-ray spectra (see Chapter 5) lend further weight to this possibility.

The pressing problem now is to understand the physical process giving rise to this energetic phenomena. As discussed in Chapter 1, there are currently three competing explanations: starburst activity, obscured AGN and advection dominated accretion.

Using standard optical line ratios, the brightest X-ray luminous galaxies appear to show a mixture of Seyfert 2 and starburst nuclei (Boyle 1995b), although in many cases the classification is ambiguous. On the basis of their optical magnitudes, X-ray luminosities and redshift distributions the two populations are identical. This suggests one underlying physical process, although it could still be that two entirely separate mechanisms are at work. High resolution optical spectra of the fainter X-ray luminous galaxies may shed more light on this matter. It may also be possible to detect faint broad wings on the emission lines if these galaxies do contain hidden active galactic nuclei.

High resolution imaging in the infra-red is being obtained which may help to

reveal any point-like red nuclei if these galaxies are harbouring obscured nuclei. Interpreting such observations should be conducted with care, as noted by Simpson (1994), since the presence of foreground dust and colour gradients in the stellar population can give spurious central red nuclei. Ground based imaging may be limited however, since the expected half light radius for most of these galaxies is of the order ~ 2 arcseconds. The unique imaging capabilities of the WFPC 2 instrument on the Hubble Space Telescope may be particularly useful in this respect, in particular for revealing star-forming regions or evidence of merging or disturbed activity.

Infra-red spectroscopy may provide a conclusive test of the obscured AGN hypothesis by allowing us to detect broad emission lines directly through the obscuring dust. If the nuclei are very heavily obscured the infra-red emission may still be obliterated, but in such a circumstance is it also difficult to produce the X-ray flux without a very large ($\sim$ 10%) scattered component. Spectrapolarimetry may then be useful to detect polarised broad line emission lines scattered around the obscuring medium and into our line of sight.

Deep radio and far infra-red observations may allow us to detect the signatures of starburst activity. The ion supported tori model of Di Matteo & Fabian should also be tested by searching for the distinctive emission peak at short radio wavelengths.

A combination of these techniques may eventually lead to an explanation for the violent activity which causes apparently normal galaxies to emit vast quantities of X-ray flux. After over 30 years of study we may be tantalizingly close to understanding the origin of the X-ray background.

References

Abraham R.G., McHardy I.M., In ESA, The 23rd ESLAB Symposium on Two Topics in X Ray Astronomy. Volume 2: AGN and the X Ray Background p865-870

Abramowicz M.A. et al 1991 A&A 245, 454

Almaini, O., Shanks, T., Boyle, B.J., Stewart, G.C. and Griffiths, R.E., (1995). Posters from the 17th Texas Symposium on Relativistic Astrophysics, MPE special report.

Almaini,O., Shanks,T., Boyle,B.J., Griffiths,R.E., Roche,N., Stewart,G.C. and Georgantopoulos,I. 1995, MNRAS In Press

Almaini O., Boyle B.J., Griffiths R.E., Shanks T., Stewart G.C. & Georgantopoulos I., 1995, MNRAS 277, L31

Antonucci R. 1993, ARA&A 31, 473

Antonucci R. & Miller J.S. 1985, ApJ 297, 612

Awaki H. et al 1991, PASJ 43, 195

Barr P. & Mushotzky R.F. 1986, Nature 320, 421

Blanco P.R., Ward M.J. & Wright G.S. 1990, MNRAS 242, 4

Boller T. et al 1992, A&AS, 261, 57

Boller T., Brandt W.N., Fink H. 1996 A&A 305, 53

Boyle B.J., Fong R., Shanks T., Peterson B.A., 1987 MNRAS 227, 717

Boyle B.J., Fong R., Shanks T., Peterson B.A., 1990 MNRAS 243, 1

Boyle B.J., Jones L.R., & Shanks, T., 1991 MNRAS 251, 482

Boyle B.J., Griffiths R.E., Shanks T., Stewart G.C., Georgantopoulos I. 1993, MNRAS 260, 49

Boyle B.J., Griffiths R.E., Shanks T., Stewart G.C., Georgantopoulos, I., 1994, MNRAS, 271,639

Boyle B.J., Griffiths R.E., Shanks T., Stewart G.C., Georgantopoulos, I., 1994, MNRAS, 271,639

Boyle B.J., McMahon R.G., Wilkes B.J., & Elvis M., 1995a, MNRAS 272,462

Boyle B.J., McMahon R.G., Wilkes B.J., & Elvis M., 1995b, MNRAS 276, 315

Brandt W.N. et al 1994, MNRAS 271, 958

Briel U.G. et al 1994, *ROSAT* Users Handbook

Carrera F.J. et al. 1995, MNRAS 275, 22

Comastri A., Setti G., Zamorani G. & Hasinger G., 1995, A&A, 296, 1

Chatfield C., The Analysis of Time Series: An Introduction, Chapman Hall Publishers, 1989.

Comastri A., Setti G., Zamorani G. et al. 1992, ApJ 384, 62

Di Matteo T. & Fabian A.C., 1996 MNRAS submitted

David L.P., Jones C. & Forman W. 1992, ApJ 388, 82

Done C. et al 1995, MNRAS 275, 417

Efstathiou G. 1995, MNRAS 272, L25

Elizalde F. & Steiner J.E., 1994 MNRAS 268, L47

Fabian A.C., Canizares C.R., Barcons X. 1989, MNRAS 239, 15

Fabian A.C. et al 1994, ApJ 436, L51

Fabian A.C. & Terlevich R. 1996, MNRAS 280, L5

Fabbiano G., Trinchieri G., Maddonald A., 1984, ApJ 284, 65

Fabbiano G. 1989 ARA&A 27, 87

Fabbiano G., Kim D. & Trinchieri G. 1992, ApJS 80, 531

Gendreau K.C. et al, 1995, Publ. Astron. Soc. Japan, 47, L5-L9

Georgantopoulos I., Stewart G.C., Shanks T., Griffiths R.E., & Boyle B.J., 1993, MNRAS 262, 619

Georgantopoulos I., Stewart G.C., Shanks T., Griffiths R.E., & Boyle B.J., 1996, MNRAS In press

Glazebrook K. et al 1995, MNRAS 275, L19

Giacconi R. et al 1962, Phys. Rev. Lett 9, 439

Giacconi R. et al 1979, ApJ 234, L1

Grandi P. et al 1992, ApJS 82, 93

Green P.J., Anderson S.F. & Ward M.J. 1992, MNRAS 254, 30

Green A.R., McHardy I.M. & Lehto H.J. 1993, MNRAS 265, 664

Griffiths R.E. & Padovani P. 1990, ApJ 360, 483

Griffiths R.E., Georgantopoulos I., Boyle B.J., Stewart G.C., Shanks T., Della Ceca R., 1995, MNRAS 275, 77

Griffiths R.E., Della Ceca R., Georgantopoulos I., Boyle B.J., Stewart G.C., Shanks T. & Fruscione A., 1996, MNRAS In press

Hasinger G., Turner J.T., George I.M., Boese G., 1992, GSFC Calibration Memo CAL/ROS/92-001

Hasinger G., Burg R., Giacconi R., Hartner G., Schmidt M., Trümper J., Zamorani G., 1993, A&A, 275, 1

Halpern J.P., 1985 ApJ, 290, 130

Heckman et al. 1993, In: The Nearest Active Galaxies, p 133, eds. J. Beckman

Hines D. et al 1991, ApJ, 374 L9

Hoyle F. 1963, ApJ 137, 993

Huchra J., Burg R., 1992, ApJ 393, 90

Iwasawa K. et al 1996, MNRAS, 279, 837

Jones L.R. et al 1991, MNRAS 249, 481

Kim D., Fabbiano G., & Trinchieri G. 1992, ApJ 393, 134

Krolik J. et al 1993, ApJ 402, 432

Kunieda A.H. et al 1990, Nature 345, 786

Lahav O. et al 1993, Nature 364, 693

Lawrence A. & Papadakis I. 1993, ApJ 414, L85

Madau P., Ghisellini G. & Fabian A.C. 1994, MNRAS 270, L17

Marshall F.E., Boldt E.A., Holt S.S. et al 1980, ApJ 235, 4

Marshall F.E., Holt S.S., Mushotzky R.F., Becker R. 1993 ApJ 269, L31

Marshall F.E., Avni Y., Tananbaum H., & Zamorani G. 1983, ApJ 269, 35

Mather J.C. et al 1990, ApJ, 354, L37

McCammon D, & Sanders W.T. 1990, Ann. Rev. Astr. Astrophys., 28, 657

McHardy I.M. & Czerny B. 1987, Nature 325, 696

McHardy I.M. 1990. In Proc. 23rd ESLAB Symp., ed. J. Hunt, B. Battrick, p. 1111. Paris: Eur. Space Agency

McHardy I.M. et al., 1995, Spectrum 6, 11

Metcalfe N., Shanks T., Fong R., Jones L.R., 1991, MNRAS 249, 498

Miller J.S., & Goodrich R.W. 1990, ApJ 355, 456

Miyaji T. et al 1994, ApJ 393, 134

Moran E.C., Halpern J.P., Helfand D.J. 1994, ApJ 433 L65

Morisawa K. et al 1990, A&A 236, 299

Mulchaey J.S. et al 1993, ApJ 414, 144

Mushotzky R.F., Done C., Pounds K.A., 1993, Ann. Rev. Astr. Ap., 31, 717

Mushotzky et al 1995, MNRAS 272 L9

Nandra K., Pounds K.A., Stewart G.C., George I.M., Hayashida K., 1991, MNRAS 248, 760

Padovani P. & Rafanelli P. 1988, A&A 205, 53

Papadakis I. & Lawrence A. 1993, Nature 361, 250

Parry I., Ellis R., Gray P., 1986, New Scientist, vol. 110, p. 36-39.

Peebles J.E. 1980, The large-scale structure of the universe, Princeton University Press

Plucinksy P.P., Snowden S.L., Briel U.G., Hasinger G., Pfeffermann E., 1993, ApJ 418, 519

Pounds K.A. et al 1990, Nature 344, 132

Roche N., Shanks T., Metcalfe, N., Fong, R., 1993, MNRAS 263, 360

Roche N., Shanks T., Georgantopoulos I., Stewart G.C., Boyle B.J., & Griffiths R.E., 1995a, MNRAS 273, L15

Rees M., 1984, Ann. Rev. Astr. Astrophys., 22, 417

Reynolds C.S. et al 1996, MNRAS submitted

Roche N., Shanks T., Almaini O., Boyle B.J., Georgantopoulos I., Stewart G.C., & Griffiths R.E., 1995b, MNRAS 276, 706

Saxton J.M. et al 1993, MNRAS 263, 63

Schwartz D.A., & Tucker W.H., 1988, ApJ 332, 157

Setti G. 1992 In: X-ray emission from AGN and the Cosmic XRB, eds. W. Brinkman W., J. Trumper

Shafer R. 1983. Ph.D. Thesis, University of Maryland

Shafer R. & Fabian A.C., 1983 In: Early Evolution of the Universe and its Present Structure, IAU Symposium No. 104, p. 333

Shanks T., Georgantopoulos I., Stewart G.C., Pounds K.A., Boyle B.J. & Griffiths R.E., 1991 Nat 353, 315

Shanks T., Almaini, O., Boyle, B.J., Della-Ceca, R., Done, C., Georgantopoulos, I., Griffiths, R.E., Rawlings, S.J., Roche, N., & Stewart, G.C., (1996). In Rontgensstrahlung from the Universe, in press.

Simpson C., 1994, MNRAS 271, 247

Simpson C., Ward M., Kotikainen J., 1994, 271, 250

Snowden S.L., Freyberg M.J., 1993, ApJ 404, 403

Stevenson P.R.F., Shanks T., Fong R., Macgillivray H.T., 1985, MNRAS 213, 953

Stewart G.C., Georgantopoulos I., Boyle B.J., Shanks T., Griffiths R., 1994, New Horizon Of X-ray Astronomy - first results from ASCA, p331, eds. F. Makino and T. Ohashi, Universal Academy Press, Tokyo

Stocke J. et al 1982, ApJ 252, 69

Tennant A.F. & Mushotzky R.F. 1983, ApJ 264, 92

Terlevich R. & Boyle B.J. 1993, MNRAS 262, 491

Terrell N.J. et al 1967

Turner M.J.L. & Pounds K.A. 1989, MNRAS 240, 833

Tresse L. et al 1994 in: Wide Field Spectroscopy And The Distant Universe, eds. Maddox S. et al

Treyer M.A. et al 1992, A&A 264, 11

Treyer M.A. & Lahav O. 1995 MNRAS Accepted

Trumper J. eds, MPE Report 235, p.414

Turner T.J, 1993, GSFC Calibration Memo CAL/ROS/93-007

Tyson J.A. 1988, AJ 96, 1

Vikhlinin A., Forman W., Jones C. & Murray S., 1995 ApJ 451, 564

Wandel A. & Mushotzky R.F. 1986, ApJ 306, L61

Ward M.J., Hughes D.H., Dunlop J.S., Appleton P.N., 1993 IAU Symposium No. 159, p. 311

Warwick R. & Stewart G.C., 1989 In: Two Topics in X-ray astronomy:AGN and the X-ray background, Proc. 23rd ESLAB Symposium, p. 727, ed. Hunt & Battrick

Watson M.G., Stanger V. & Griffiths R.E. 1984, ApJ 286, 144

Wright R., 1979, ApJ 232, 348

Yaqoob T., 1992, MNRAS 258, 198

Zamorani G. et al 1981, ApJ 245, 357

Zdziarski et al 1993 ApJ 405, 125

Appendix A

Optical spectra

Here we present the spectra of optical counterparts to X-ray sources from the BJS855 and BJS864 Deep *ROSAT* Survey fields. These are unfluxed spectra obtained with the Autofib system and the RGO spectrograph at the 3.9m Anglo-Australian Telescope. Details of the X-ray source detection, data reduction and optical identification are given in Chapter 2.

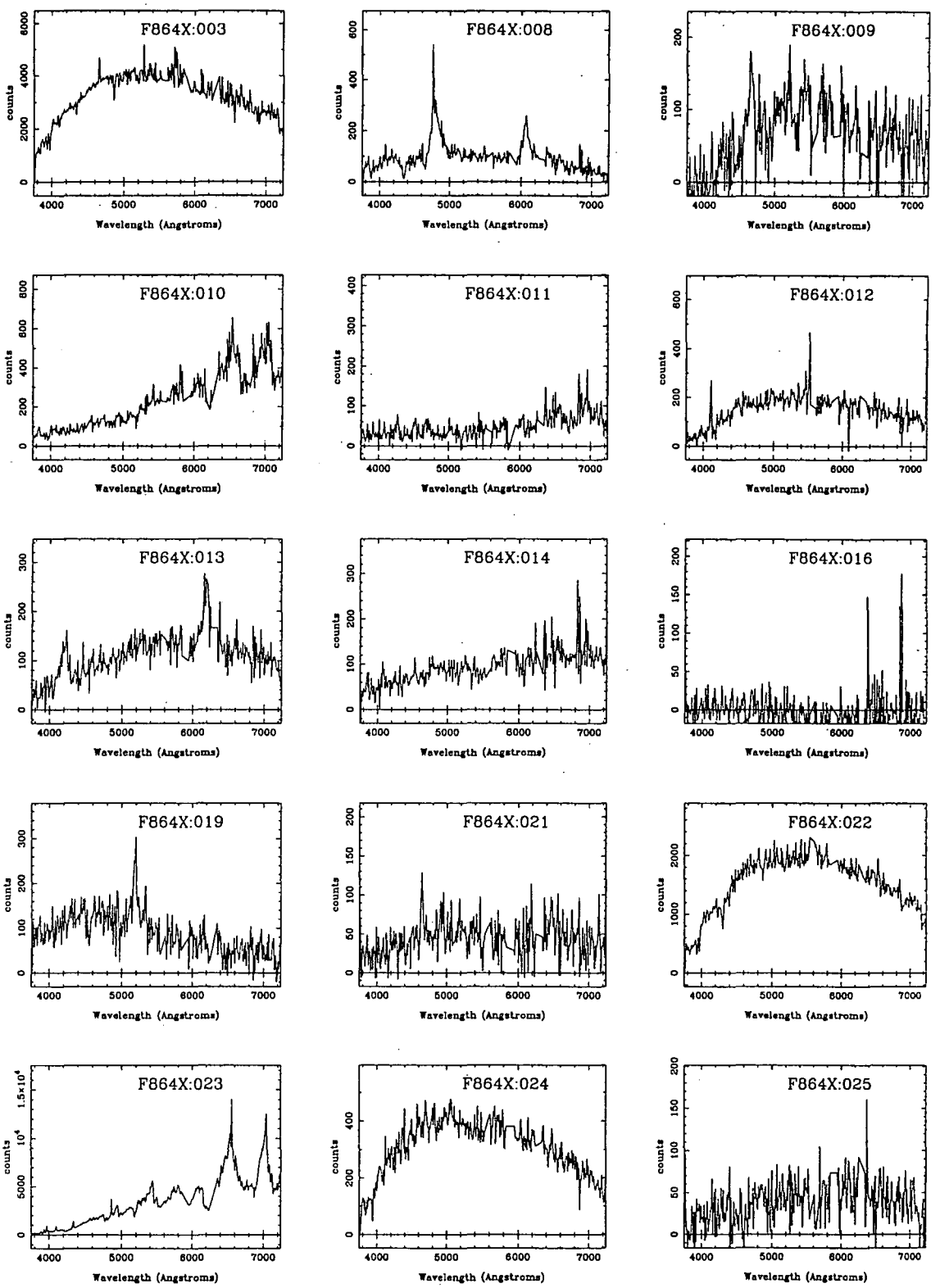

Figure A.1: Low resolution ($\sim$ 12Å) spectra of optical counterparts to X-ray sources on the BJS864 field. Counts give the total number of photons per 10Å bin.

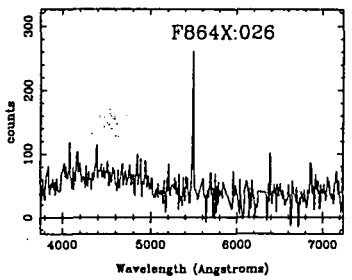
F864X:026
counts
Wavelength (Angstroms)

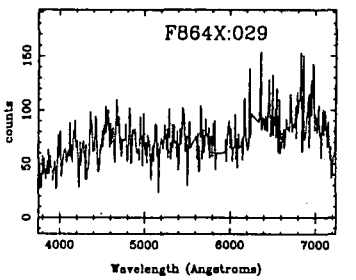
F864X:029
counts
Wavelength (Angstroms)

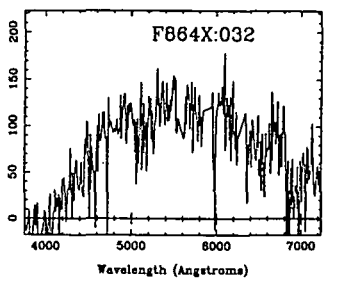
F864X:032
counts
Wavelength (Angstroms)

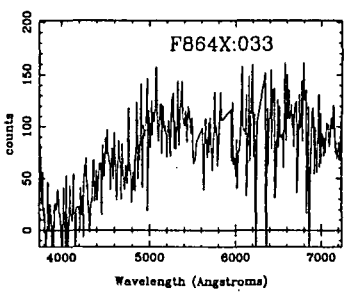
F864X:033
counts
Wavelength (Angstroms)

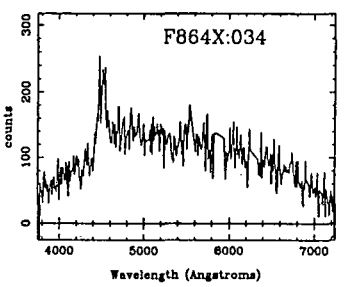
F864X:034
counts
Wavelength (Angstroms)

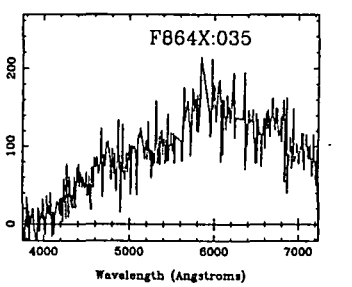
F864X:035
counts
Wavelength (Angstroms)

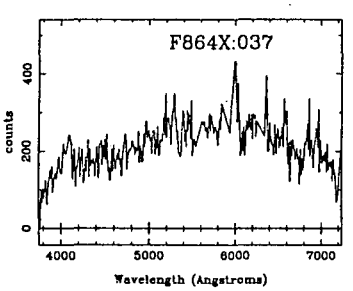
F864X:037
counts
Wavelength (Angstroms)

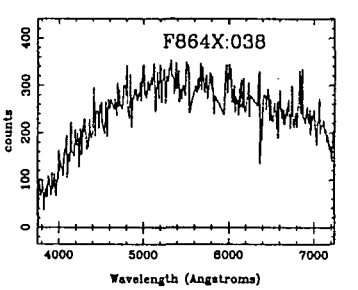
F864X:038
counts
Wavelength (Angstroms)

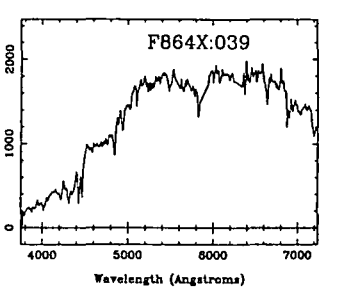
F864X:039
counts
Wavelength (Angstroms)

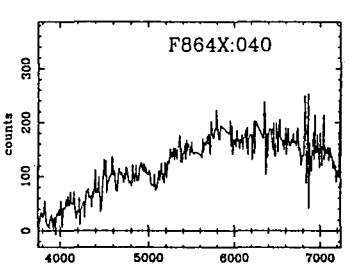
F864X:040
counts
Wavelength (Angstroms)

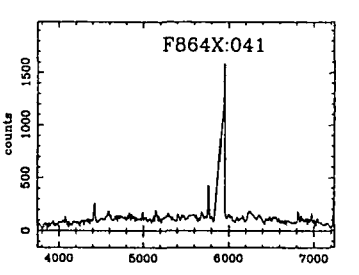
F864X:041
counts
Wavelength (Angstroms)

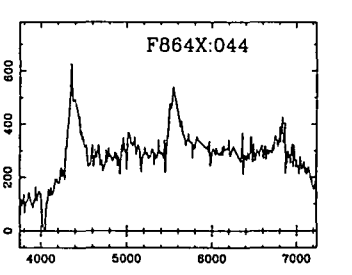
F864X:044
counts
Wavelength (Angstroms)

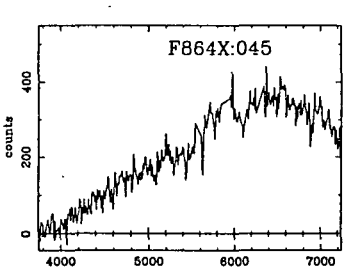
F864X:045
counts
Wavelength (Angstroms)

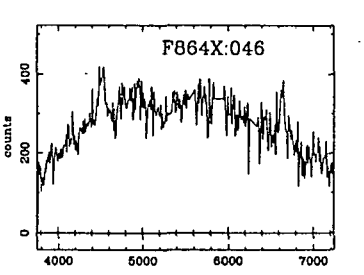
F864X:046
counts
Wavelength (Angstroms)

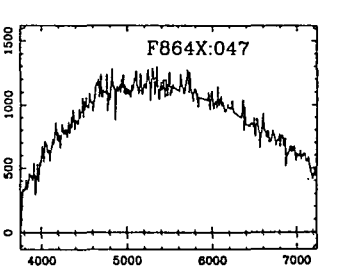
F864X:047
counts
Wavelength (Angstroms)

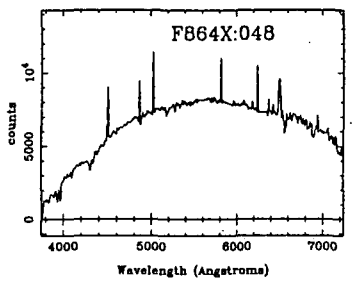
F864X:048
counts
Wavelength (Angstroms)

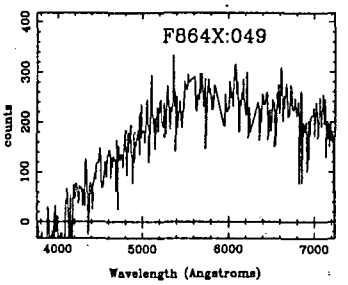
F864X:049
counts
Wavelength (Angstroms)

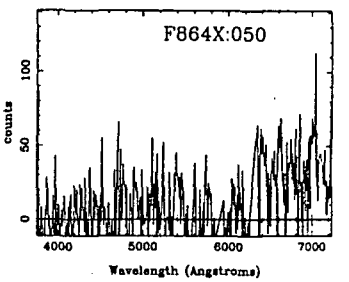
F864X:050
counts
Wavelength (Angstroms)

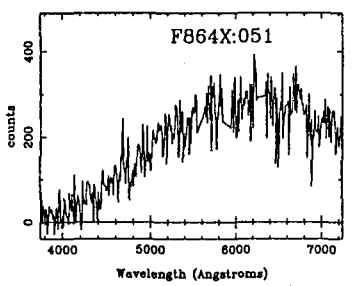
F864X:051
counts
Wavelength (Angstroms)

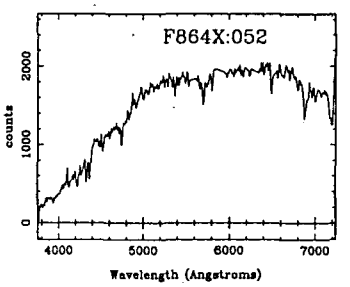
F864X:052
counts
Wavelength (Angstroms)

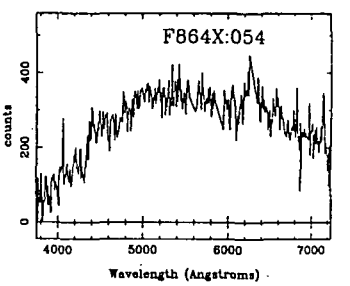
F864X:054
counts
Wavelength (Angstroms)

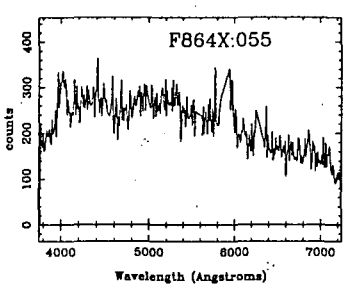
F864X:055
counts
Wavelength (Angstroms)

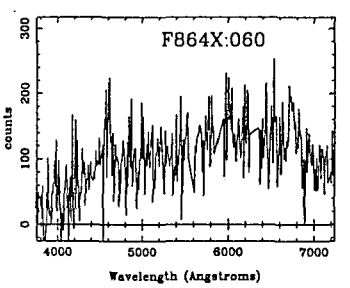
F864X:060
counts
Wavelength (Angstroms)

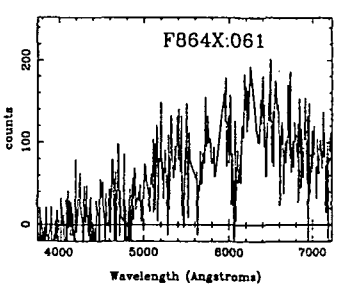
F864X:061
counts
Wavelength (Angstroms)

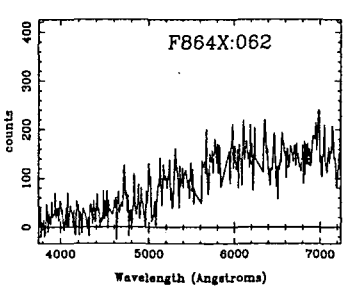
F864X:062
counts
Wavelength (Angstroms)

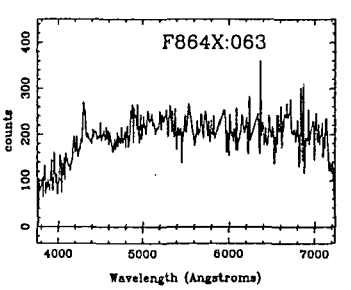
F864X:063
counts
Wavelength (Angstroms)

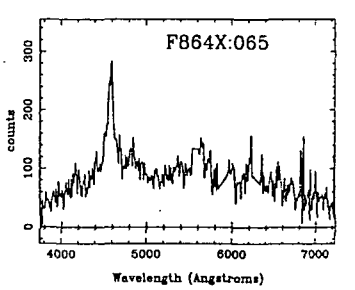
F864X:065
counts
Wavelength (Angstroms)

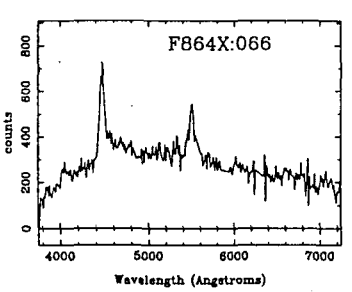
F864X:066
counts
Wavelength (Angstroms)

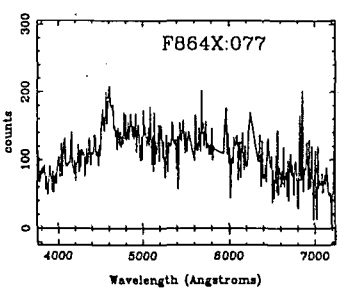
F864X:077
counts
Wavelength (Angstroms)

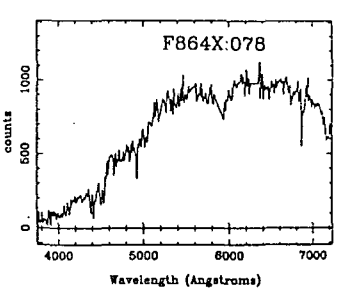
F864X:078
counts
Wavelength (Angstroms)

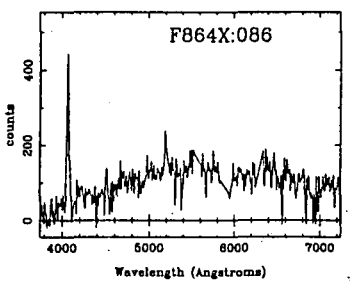
F864X:086
counts
Wavelength (Angstroms)

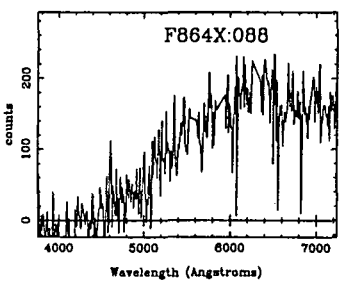
F864X:088
counts
Wavelength (Angstroms)

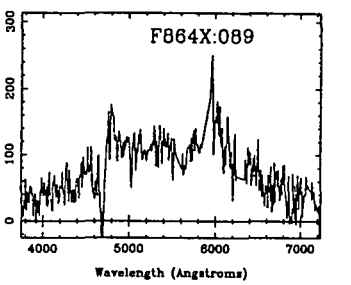
F864X:089
counts
Wavelength (Angstroms)

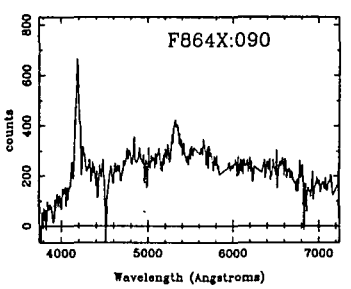
F864X:090
counts
Wavelength (Angstroms)

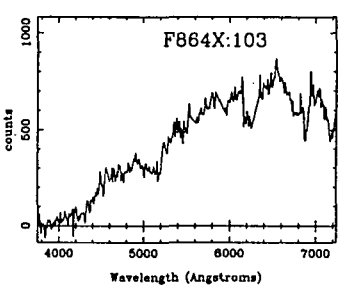
F864X:103
counts
Wavelength (Angstroms)

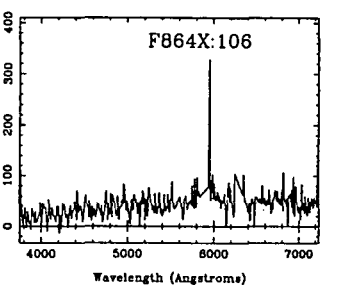
F864X:106
counts
Wavelength (Angstroms)

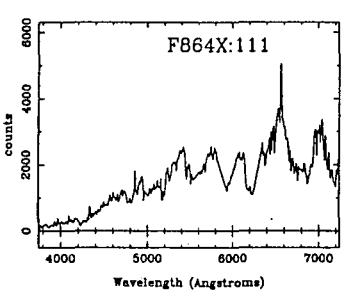
F864X:111
counts
Wavelength (Angstroms)

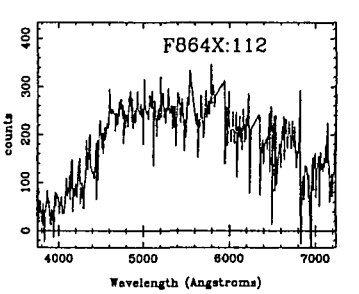
F864X:112
counts
Wavelength (Angstroms)

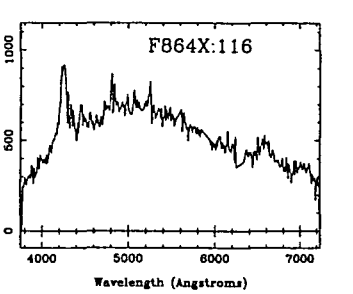
F864X:116
counts
Wavelength (Angstroms)

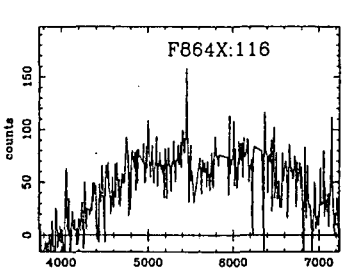
F864X:116
counts
Wavelength (Angstroms)

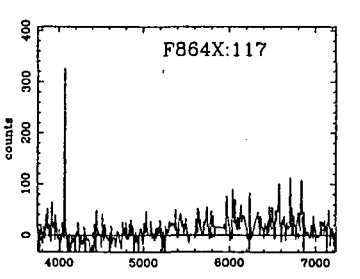
F864X:117
counts
Wavelength (Angstroms)

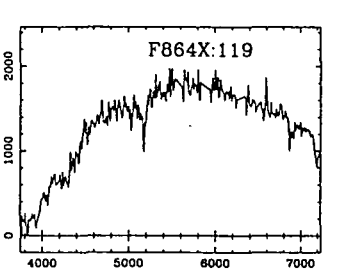
F864X:119
counts
Wavelength (Angstroms)

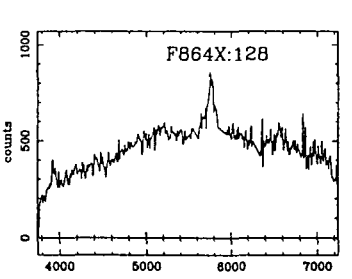
F864X:128
counts
Wavelength (Angstroms)

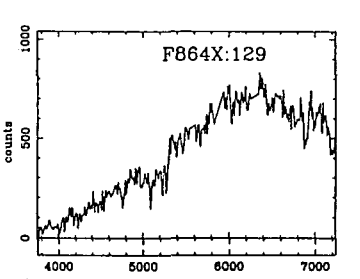
F864X:129
counts
Wavelength (Angstroms)

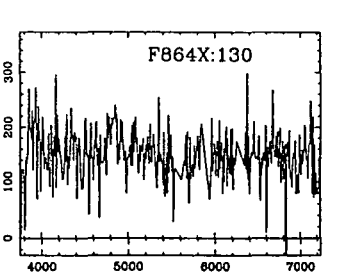
F864X:130
counts
Wavelength (Angstroms)

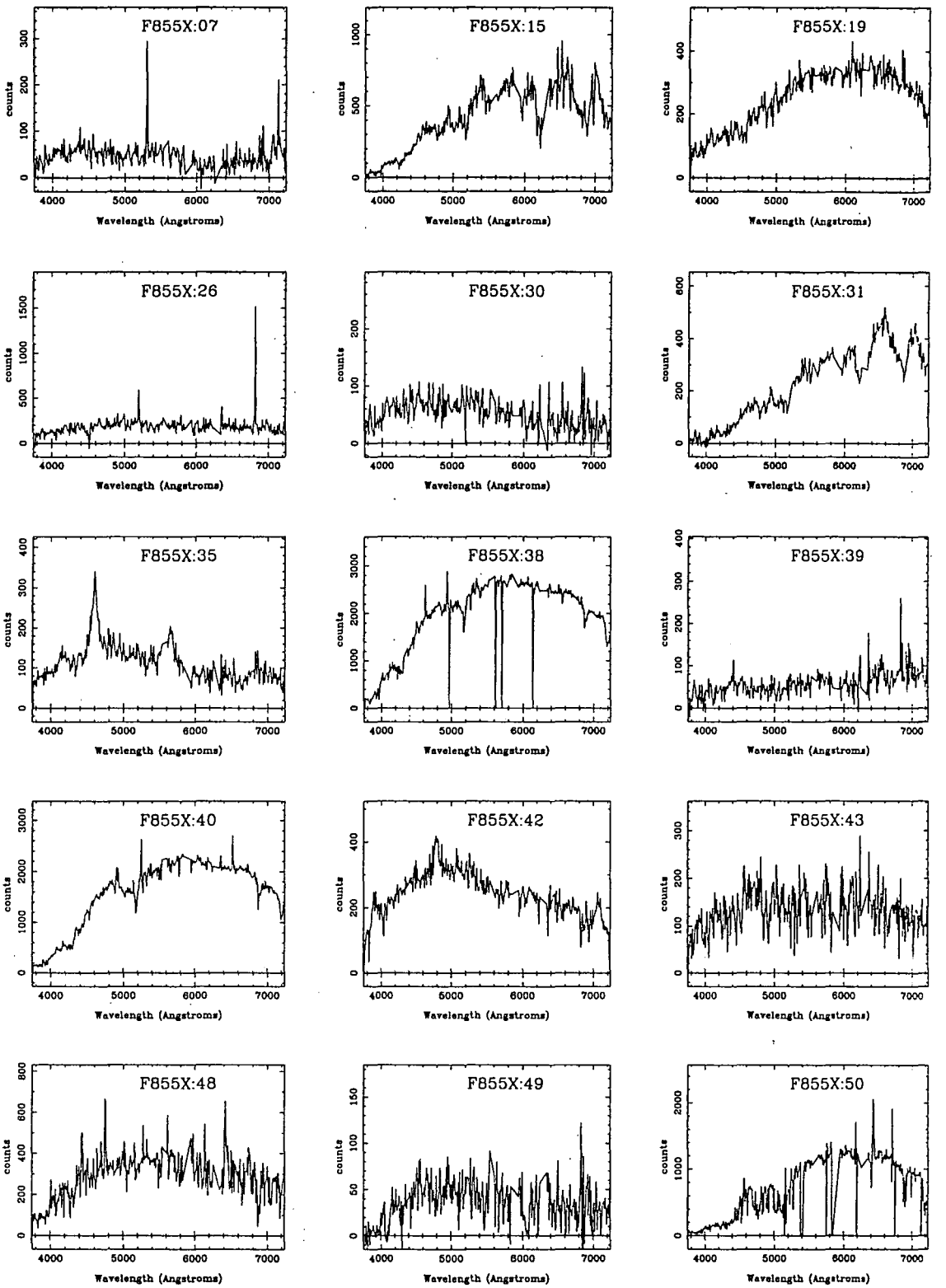

Figure A.2: Low resolution ($\sim$ 12Å) spectra of optical counterparts to X-ray sources on the BJS855 field. Counts give the mean number of photons per 2000 second exposure per 10Å bin.

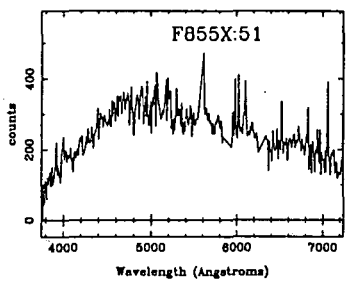
F855X:51
counts
Wavelength (Angstroms)

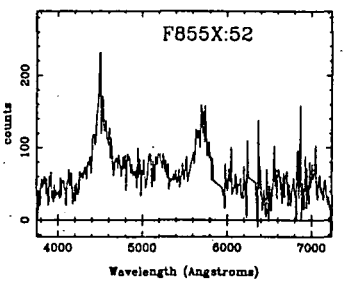
F855X:52
counts
Wavelength (Angstroms)

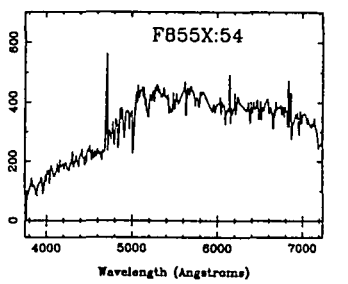
F855X:54
counts
Wavelength (Angstroms)

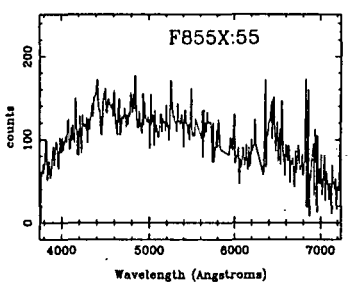
F855X:55
counts
Wavelength (Angstroms)

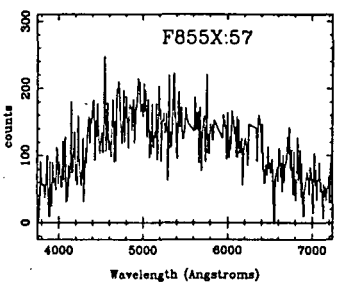
F855X:57
counts
Wavelength (Angstroms)

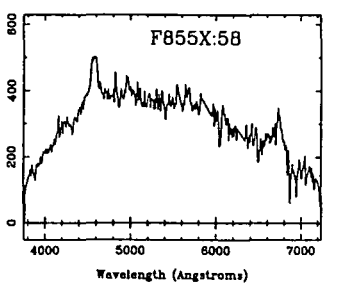
F855X:58
counts
Wavelength (Angstroms)

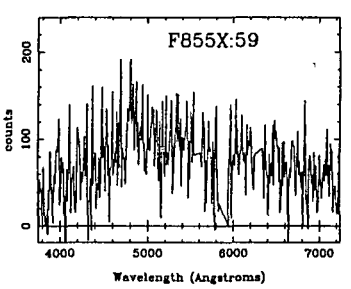
F855X:59
counts
Wavelength (Angstroms)

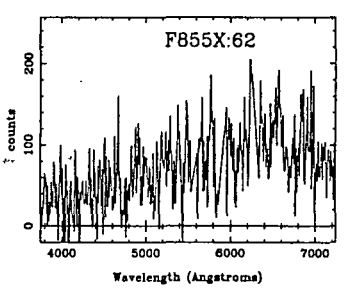
F855X:62
counts
Wavelength (Angstroms)

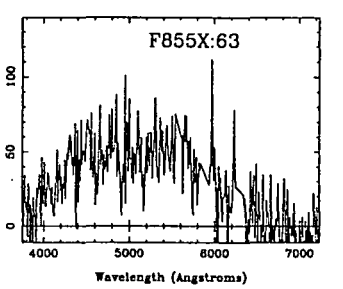
F855X:63
counts
Wavelength (Angstroms)

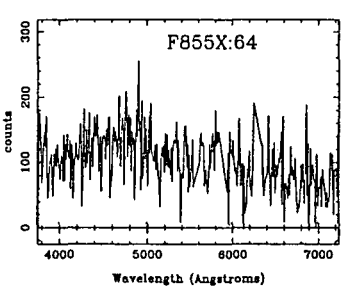
F855X:64
counts
Wavelength (Angstroms)

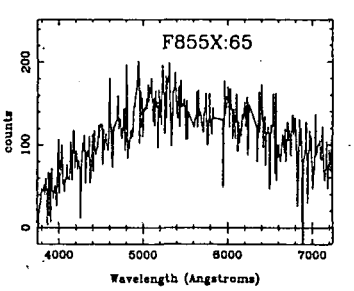
F855X:65
counts
Wavelength (Angstroms)

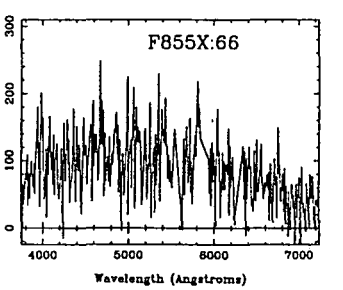
F855X:66
counts
Wavelength (Angstroms)

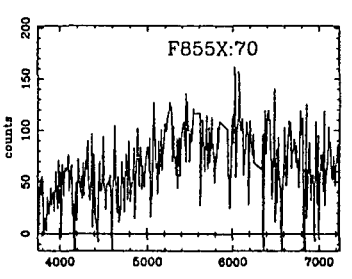
F855X:70
counts
Wavelength (Angstroms)

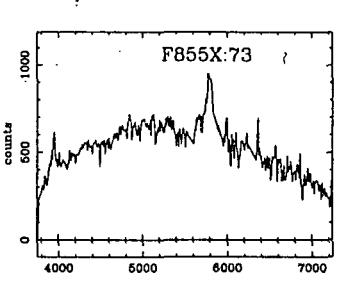
F855X:73
counts
Wavelength (Angstroms)

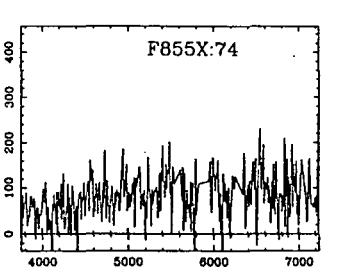
F855X:74
counts
Wavelength (Angstroms)

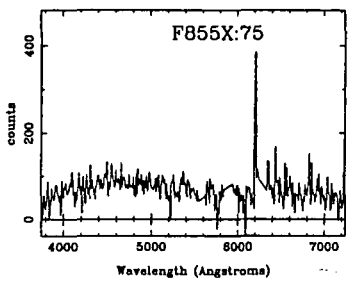
F855X:75
counts
Wavelength (Angstroms)

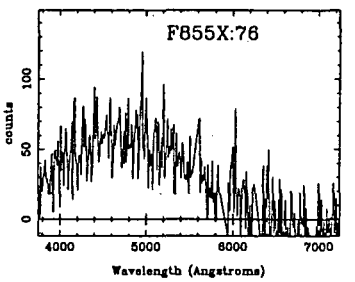
F855X:76
counts
Wavelength (Angstroms)

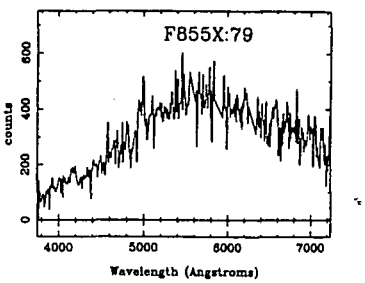
F855X:79
counts
Wavelength (Angstroms)

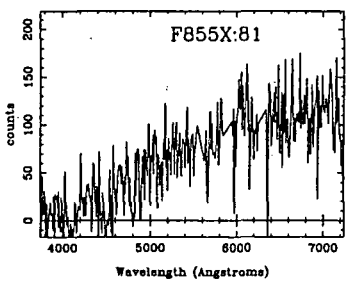
F855X:81
counts
Wavelength (Angstroms)

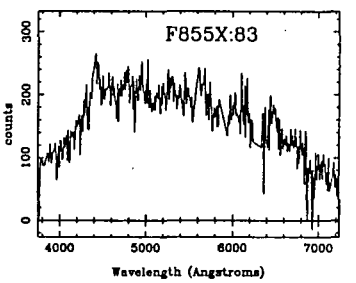
F855X:83
counts
Wavelength (Angstroms)

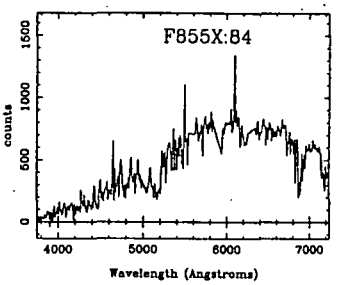
F855X:84
counts
Wavelength (Angstroms)

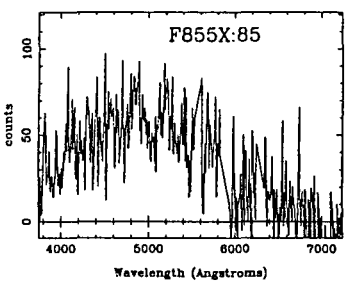
F855X:85
counts
Wavelength (Angstroms)

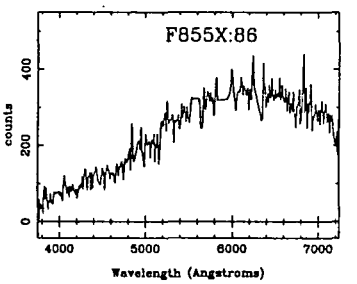
F855X:86
counts
Wavelength (Angstroms)

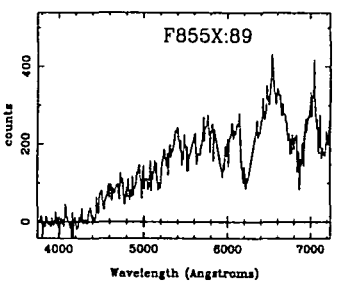
F855X:89
counts
Wavelength (Angstroms)

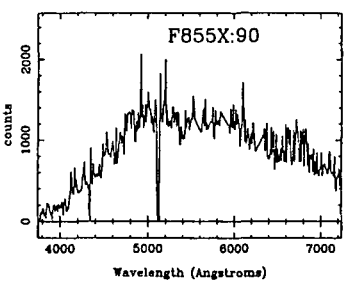
F855X:90
counts
Wavelength (Angstroms)

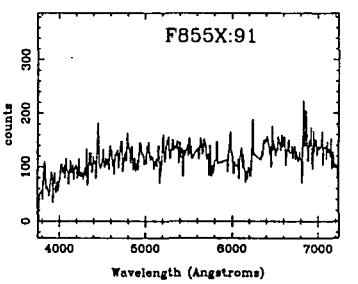
F855X:91
counts
Wavelength (Angstroms)

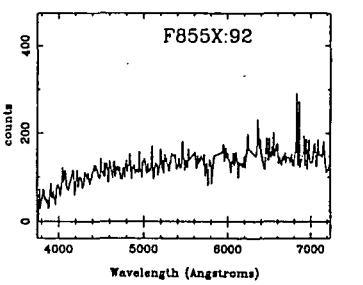
F855X:92
counts
Wavelength (Angstroms)

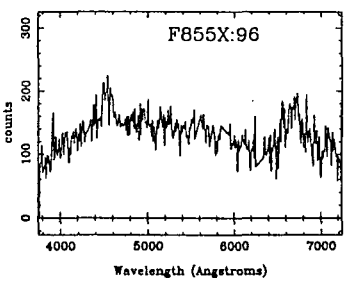
F855X:96
counts
Wavelength (Angstroms)

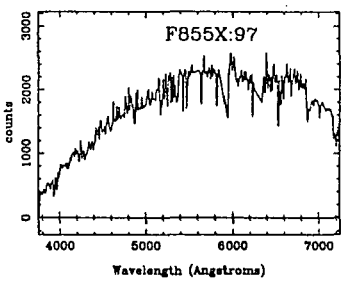
F855X:97
counts
Wavelength (Angstroms)

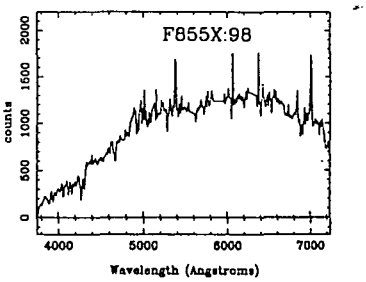
F855X:98
counts
Wavelength (Angstroms)

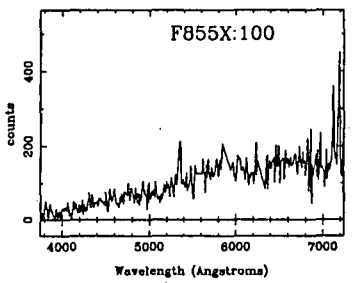
F855X:100
counts
Wavelength (Angstroms)

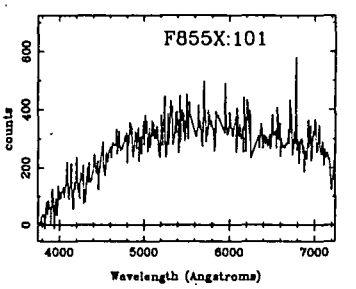
F855X:101
counts
Wavelength (Angstroms)

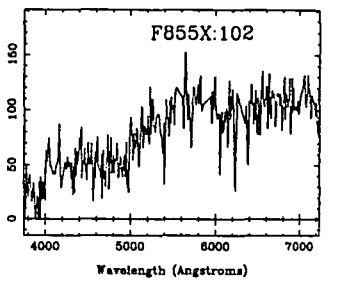
F855X:102
counts
Wavelength (Angstroms)

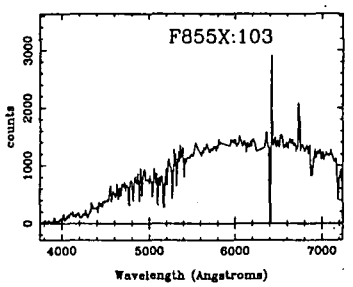
F855X:103
counts
Wavelength (Angstroms)

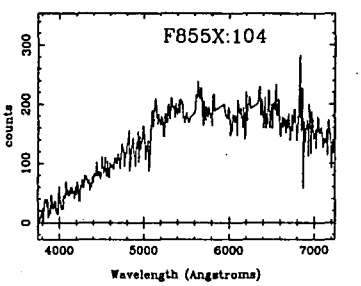
F855X:104
counts
Wavelength (Angstroms)

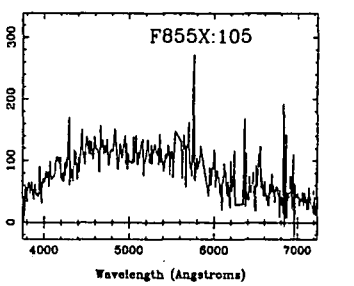
F855X:105
counts
Wavelength (Angstroms)

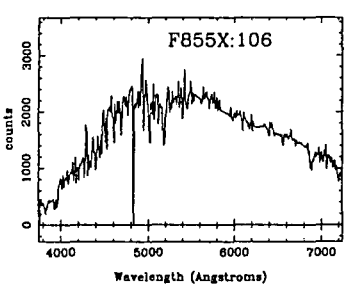
F855X:106
counts
Wavelength (Angstroms)

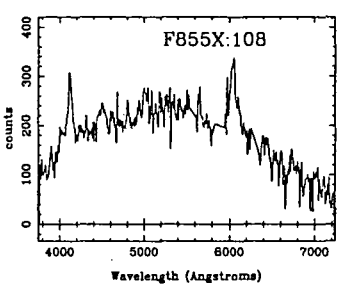
F855X:108
counts
Wavelength (Angstroms)

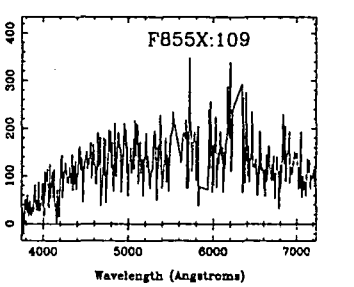
F855X:109
counts
Wavelength (Angstroms)

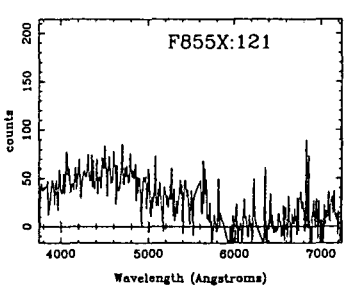
F855X:121
counts
Wavelength (Angstroms)

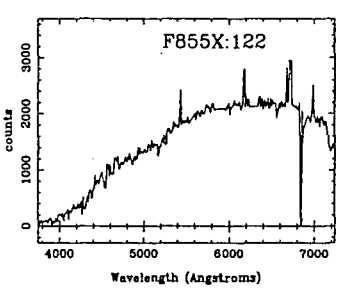
F855X:122
counts
Wavelength (Angstroms)

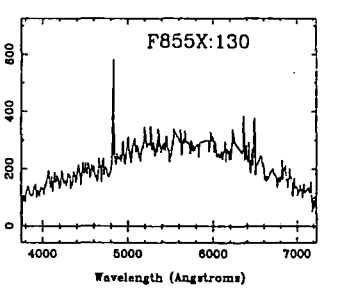
F855X:130
counts
Wavelength (Angstroms)

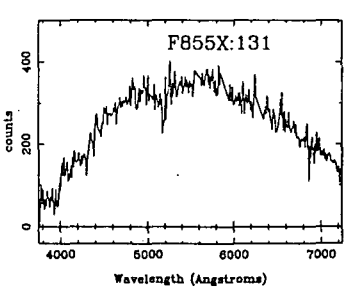
F855X:131
counts
Wavelength (Angstroms)

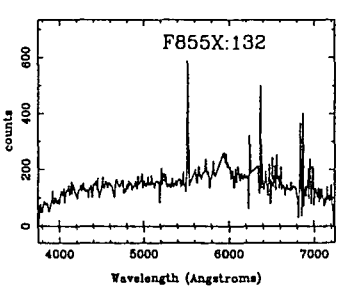
F855X:132
counts
Wavelength (Angstroms)

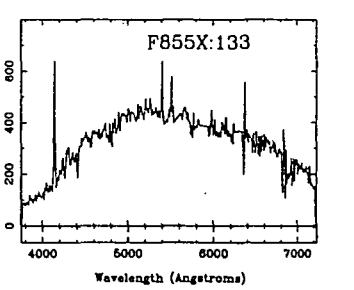
F855X:133
counts
Wavelength (Angstroms)

Appendix B

X-ray source catalogue

Here the catalogue of X-ray sources identified on the BJS855 and BJS864 fields is presented. Full details of the *ROSAT* fields, source detection and optical spectroscopic observations are given in Chapter 2. The columns give the X-ray source name, distance from the centre of the *ROSAT* field in arcminutes, $0.5-2\,\mathrm{keV}$ X-ray flux, the offset from X-ray source to optical counterpart in arcseconds, b_j magnitude, $u-b_j$ colour, optical identification, redshift and finally various comments. For QSOs previously identified in the UVX survey of Boyle et al (1990) the optical name is given in the final column. For emission line galaxies the parameter W gives the equivalent width of the OII emission line in Å. For galaxies with absorption features the D parameter gives a measure of the H & K break (the ratio of the continuum immediately above and below the CaII H & K features near 4000Å).

Table B.1: Catalogue of X-ray sources identified within the central 20 arcminute region of the BJS855 and BJS864 fields to an approximate flux limit of 4×10^{-15}erg s^{-1}cm^{-2}.

Object	r	Sig.	flux	d_{xo}	b_j	$u - b_j$	ID	redshift	comments
F855X:012	18.7	5.33	3.107×10^{-15}						
F855X:016	17.9	9.68	1.252×10^{-14}						
F855X:017	16.8	8.71	1.965×10^{-14}	21.8	22.66	0.55	?		
F855X:018	14.3	4.06	6.249×10^{-15}	8.04	21.82	1.80	?		
F855X:019	2.04	7.13	3.203×10^{-15}	21.6	18.50	1.08	NL	0.130	W=8A, D=1.29
F855X:030	10.8	11.1	3.175×10^{-14}	14.8	21.49	0.38	?		
F855X:035	14.2	4.45	2.328×10^{-15}	8.04	22.50	-0.22	QSO	1.97	
F855X:036	13.4	15.5	3.002×10^{-14}						
F855X:039	14.4	5.28	6.604×10^{-15}	8.04	21.34	-0.94	QSO	1.358	F855:141
F855X:040	14.1	5.86	5.846×10^{-15}	28.1	17.07	0.47	G		
F855X:041	17.0	4.09	1.782×10^{-15}	16.0	22.52	2.02	?		
F855X:042	19.0	5.11	3.720×10^{-15}	18.0	20.86	0.47	QSO	1.51	
F855X:043	3.30	7.00	5.621×10^{-15}	12.9	20.80	-0.70	QSO	1.952	F855:125
F855X:048	14.3	18.5	1.029×10^{-13}	26.2	18.20	-0.29	Gal	0.08	D=1.3
F855X:049	12.6	6.63	1.842×10^{-14}	18.0	22.13	0.84	?		
F855X:050	11.8	9.26	9.469×10^{-15}	7.20	18.78	1.43	?		
F855X:051	11.1	6.99	7.830×10^{-15}	18.3	19.69	0.17	QSO	1.00	
F855X:052	16.6	7.49	1.124×10^{-14}	11.3	21.35	1.43	QSO	2.68	
F855X:053	17.7	35.6	4.377×10^{-14}	26.2	22.81	0.00	?		
F855X:054	9.40	4.57	3.648×10^{-15}	11.3	20.37	1.05	NL	0.26	W=20A, D=1.25
F855X:055	10.5	5.32	3.689×10^{-15}	14.4	21.29	0.85	QSO	1.31	
F855X:058	8.40	4.77	4.327×10^{-15}	12.9	21.23	0.59	QSO	1.40	
F855X:059	13.8	9.00	2.372×10^{-14}	11.3	20.41	-0.31	QSO	0.729	F855:111
F855X:060	11.8	8.98	1.999×10^{-14}	0.24	21.21	-1.19	QSO	1.073	F855:133
F855X:062	8.10	5.15	5.691×10^{-15}	6.80	21.21	-0.83	QSO	1.107	F855:134
F855X:063	12.8	6.20	6.970×10^{-15}	7.20	20.83	1.87	?		
F855X:064	5.40	5.50	4.976×10^{-15}	0.25	20.75	-0.84	QSO	2.057	F855:123
F855X:065	4.00	4.75	2.678×10^{-15}	11.3	21.76	0.06	?		
F855X:066	10.8	6.35	5.725×10^{-15}	8.04	20.12	-0.87	QSO	1.087	F855:107
F855X:067	17.1	8.47	1.254×10^{-14}	18.3	22.81	-0.23	?		
F855X:068	8.60	4.48	4.238×10^{-15}	15.2	21.04	1.82	?		
F855X:069	18.7	5.15	6.769×10^{-15}						
F855X:070	16.8	5.27	1.133×10^{-14}	5.09	22.17	1.60	?		
F855X:071	16.3	5.58	1.447×10^{-14}						
F855X:072	15.6	4.50	9.819×10^{-15}						
F855X:073	4.50	11.5	2.706×10^{-14}	8.04	20.65	0.01	QSO	1.07	
F855X:074	6.00	4.04	2.108×10^{-15}	0.43	21.10	-0.27	?		
F855X:075	7.70	7.29	2.350×10^{-15}	18.3	22.36	-0.16	?		

Object	r	Sig.	flux	d_{xo}	b_j	$u-b_j$	ID	redshift	comments
F855X:076	17.1	4.77	8.109×10^{-15}	16.0	22.14	0.83	?		
F855X:077	15.6	13.1	4.819×10^{-14}	3.60	18.16	1.21	?		
F855X:078	13.5	5.15	4.313×10^{-15}						
F855X:079	8.30	6.50	7.510×10^{-15}	10.1	19.37	1.11	Gal	0.299	W=8A, D=1.42
F855X:080	9.20	10.8	2.220×10^{-14}	8.04	21.59	-1.23	QSO	1.789	F855:155
F855X:081	4.10	4.08	2.727×10^{-15}	23.0	20.79	4.47	?		
F855X:082	5.90	10.1	1.213×10^{-14}	25.4	20.98	1.06	?		
F855X:083	9.90	4.36	1.875×10^{-15}	0.56	21.78	-0.28	QSO	1.31	
F855X:084	10.6	4.83	2.712×10^{-15}	21.8	19.59	1.30	K		
F855X:085	7.40	4.46	4.196×10^{-15}	11.3	22.79	2.47	?		
F855X:086	7.90	4.27	2.346×10^{-15}	3.60	21.27	1.96	NL	0.30	W=10A, D=1.23
F855X:088	18.6	5.84	8.830×10^{-15}	18.0	22.22	-0.92	?		
F855X:089	13.4	7.17	8.399×10^{-15}	3.60	22.03	0.00	M		
F855X:090	14.5	4.16	8.282×10^{-15}	11.3	16.89	1.38	?		
F855X:091	17.6	5.43	6.638×10^{-15}	8.04	20.65	1.37	NL	0.19	W=14A
F855X:092	14.4	6.61	8.366×10^{-15}	16.0	22.23	0.51	?		
F855X:093	16.0	6.39	6.313×10^{-15}						
F855X:096	8.10	6.18	4.438×10^{-15}	14.8	21.13	-0.21	QSO	1.37	
F855X:097	9.10	10.9	1.313×10^{-14}	7.19	16.90	-0.13	F		
F855X:098	14.9	5.30	5.281×10^{-15}	20.9	17.66	1.68	Gal	0.086	D=1.47
F855X:100	8.50	4.09	1.145×10^{-15}	3.59	21.26	0.96	NL	0.435	W=30A
F855X:104	12.6	9.29	8.390×10^{-15}		21.32		Gal	0.28	
F855X:105	11.5	7.96	7.778×10^{-15}	11.3	20.61	4.65	NL	0.149	W=10A
F855X:106	1.20	4.82	1.071×10^{-15}	10.8	17.50	0.27	G		
F855X:108	12.7	9.13	1.310×10^{-14}	3.60	21.24	0.32	QSO	1.16	
F855X:112	11.2	8.79	1.064×10^{-14}	5.09	21.28	-1.26	QSO	1.18	F855:137
F855X:118	18.4	8.36	1.925×10^{-14}						
F855X:121	16.0	4.66	4.859×10^{-15}	8.04	22.50	-0.70	?		
F855X:122	16.4	4.18	6.428×10^{-15}	8.04	17.16	0.37	?		
F855X:126	17.5	9.13	1.879×10^{-14}						
F855X:130	5.10	6.03	9.024×10^{-15}	15.2	21.20	1.09	NL	0.295	W=30A
F855X:131	5.80	7.16	5.925×10^{-15}						
F855X:133	15.9	4.30	6.412×10^{-15}	24.1	19.64	1.00	NL	0.111	W=40A,D=1.2

Object	r	Sig.	flux	d_{xo}	b_j	$u-b_j$	ID	redshift	comments
F864X:004	13.6	5.77	5.995×10^{-15}	8.98	21.43	-0.35	QSO	1.767	F864:148
F864X:007	13.2	18.4	3.069×10^{-14}	5.09	19.42	1.77			
F864X:008	13.1	4.83	3.687×10^{-15}	8.04	22.78	-22.78	QSO	2.92	
F864X:009	12.4	12.6	2.195×10^{-14}	8.04	20.87	-0.66	QSO	0.667	F864:119
F864X:010	13.3	7.14	6.108×10^{-15}						
F864X:011	3.70	7.59	5.582×10^{-15}	10.4	22.48	2.69	?		
F864X:012	17.8	13.0	2.527×10^{-14}	16.2	20.22	1.28	NL	0.10	W=47A
F864X:013	11.4	10.5	1.667×10^{-14}	11.6	21.86	-0.41	QSO	2.21	
F864X:014	10.3	4.32	3.436×10^{-15}	16.3	22.46	2.12	?		
F864X:015	19.6	5.27	9.106×10^{-15}						
F864X:016	16.3	4.56	3.896×10^{-15}	7.20	22.99	0.26	?		
F864X:017	19.1	36.5	1.311×10^{-13}						
F864X:019	18.4	7.50	1.096×10^{-14}	3.60	20.69	-0.69	QSO	0.852	F864:111
F864X:021	17.4	6.33	9.130×10^{-15}	3.59	22.65	0.84	?		
F864X:022	13.2	5.34	1.145×10^{-14}	19.3	<15	0.00	G		
F864X:023	10.3	32.5	7.779×10^{-14}	8.04	<15	0.00	M(e)		
F864X:024	7.00	4.17	3.916×10^{-15}	25.4	20.24	-0.30	?		
F864X:025	14.2	7.08	7.249×10^{-15}	19.3	21.05	0.68	?		
F864X:029	5.10	12.5	1.436×10^{-15}						
F864X:031	19.8	12.8	2.525×10^{-14}						
F864X:032	17.0	14.2	4.300×10^{-14}	3.60	21.54	0.47	?		
F864X:034	8.80	14.4	1.612×10^{-14}	5.09	22.64	-0.23	QSO	1.91	
F864X:035	6.70	5.20	4.123×10^{-15}	14.8	22.52	1.68	?		
F864X:037	10.0	8.82	9.378×10^{-15}	3.60	20.31	-1.29	QSO	1.140	F864:97
F864X:039	0.30	7.72	6.580×10^{-15}	16.0	17.91	2.19	Gal	0.126	D=1.96
F864X:040	2.60	11.3	1.148×10^{-14}	15.2	22.47	-22.47	K		
F864X:044	7.50	7.94	1.035×10^{-14}	3.60	21.33	-0.14	QSO	2.59	
F864X:045	6.00	4.37	2.742×10^{-15}	25.9	22.23	3.11	Gal	0.40	
F864X:046	4.30	5.81	6.150×10^{-15}	3.59	20.15	-0.26	QSO	1.36	
F864X:047	5.90	4.92	2.605×10^{-15}	24.1	19.28	-0.22	F		
F864X:048	17.0	4.39	1.001×10^{-14}	20.9	<15	0.00	G		
F864X:049	17.1	4.19	9.468×10^{-15}	12.9	20.75	-0.07	?		
F864X:051	9.40	5.35	5.044×10^{-15}	10.8	20.13	1.85	NL	0.25	W=20A
F864X:052	14.6	4.80	8.233×10^{-15}	20.3	17.64	1.42	NLw	0.103	W=6A, D=1.36
F864X:053	19.5	22.2	7.728×10^{-14}	14.8	19.83	-0.05	QSO	0.804	F864:72
F864X:054	10.1	5.86	5.643×10^{-15}	21.8	19.53	1.36	NL	0.089	W=16A,D=1.5
F864X:055	10.6	17.2	1.739×10^{-14}	5.09	20.88	-0.99	QSO	1.11	
F864X:056	16.6	4.01	1.032×10^{-15}	8.04	22.54	1.38	?		
F864X:060	16.3	11.4	1.852×10^{-14}	0.23	20.70	-0.94	QSO	1.410	F864:113
F864X:061	17.5	6.14	7.751×10^{-15}	3.60	22.08	-0.32	?		
F864X:062	9.90	6.05	5.222×10^{-15}	18.0	19.81	5.53	?		
F864X:063	16.8	7.82	1.159×10^{-15}						

Object	r	Sig.	flux	d_{xo}	b_j	$u-b_j$	ID	redshift	comments
F864X:064	18.2	8.56	2.027×10^{-14}						
F864X:065	7.80	4.22	4.153×10^{-15}	11.3	22.69	-1.32	QSO	1.96	
F864X:066	7.20	9.50	1.159×10^{-14}	5.09	20.39	-1.23	QSO	1.89	F864:102
F864X:068	14.2	6.40	1.193×10^{-15}						
F864X:069	14.2	4.66	1.524×10^{-15}						
F864X:070	20.0	4.71	2.327×10^{-15}						
F864X:077	11.0	9.55	8.948×10^{-15}	7.20	21.95	0.07	QSO	1.97	
F864X:078	11.6	6.14	6.535×10^{-15}	7.20	19.41	2.03	Gal	0.15	D=1.6
F864X:085	18.2	8.43	2.158×10^{-14}	15.2	22.70	0.85	?		
F864X:086	16.9	14.9	3.338×10^{-14}	2.35	21.98	0.27	NLQSO	2.35	
F864X:087	13.7	4.72	4.218×10^{-15}	5.09	20.77	1.12	?		
F864X:088	12.1	4.28	4.580×10^{-15}	8.04	21.55	3.79	Gal	0.27	
F864X:089	18.8	4.90	6.085×10^{-15}	19.3	22.67	-0.52	QSO	2.10	
F864X:090	18.9	5.20	1.028×10^{-14}	14.8	20.21	-0.03	QSO	2.44	
F864X:105	11.6	4.23	2.989×10^{-15}	18.3	20.89	1.62	K/M		
F864X:106	12.1	8.91	8.322×10^{-15}	5.09	22.58	-0.35	?		
F864X:111	15.8	7.96	7.886×10^{-15}	5.09	19.55	1.36	M(e)		
F864X:112	14.7	8.19	2.032×10^{-15}	7.20	20.98	0.10			
F864X:116	17.4	8.25	1.055×10^{-14}	21.8	19.46	-0.87	QSO	1.22	F864:76
F864X:117	18.6	4.74	1.035×10^{-14}	18.3	18.90	1.16	?		
F864X:119	8.90	4.04	2.993×10^{-15}	18.3	18.96	0.42	K		
F864X:120	8.00	5.14	4.579×10^{-15}	3.60	< 15	12.45	?		
F864X:128	8.60	20.2	3.421×10^{-14}	5.09	19.69	-0.26	QSO	1.055	F864:81